Towards fabrication of optomechanical actuators by two-photon polymerisation

Alan Forrester

October 17, 2017

Abstract

This thesis describes theoretical and experimental progress toward making optical actuators: structures with nanoscale features that change shape when illuminated by light. Experiments on making nanoscale structures were conducted using the Nanoscribe: a commercial two-photon polymerisation machine. The Nanoscribe produces solid structures in a liquid resist called IP-L 780 in regions of the order of 100 nm around the focus of a laser beam, which is moved relative to the resist to make extended structures. These experiments tested the feature size of structures made using the Nanoscribe, and the optical and mechanical properties of the polymer it produces. Structures were created to test the effects on feature size of changing the power of the laser beam and the speed of its motion through the resist. Models were created to explain the width and depth of parts of features. These models did not match the experimental data, but the information on feature size is useful for designing structures. Making optical actuators requires information about mechanical properties of the polymer. Beams supported by a block at each end were created to test the mechanical properties of the solidified IP-L 780. These structures were designed to bend when exposed to forces to yield information about their Youngs modulus. Those forces were applied using a profiler. The results could not be explained by the models used to design the structures but directions for further research into the mechanical properties are considered. A series of Bragg stacks were made using the Nanoscribe to test the optical properties of the polymer and find out whether it could be used reliably to make structures with complex internal structure required to produce optical effects such as interference. The results were compatible with some of the stacks having the complex internal structure required.

Contents

Acknowledgements

I would like to thank Tim Freegarde for funding and discussions on the subject of the project described in this thesis and comments on this thesis.

Thanks to Mohammad Belal for discussions of optical and mechanical characterisation of the structures described herein.

Thanks to James Bateman for discussions and suggestions on the topic of this thesis.

I would like to thank Elena Mavrona for conducting measurements of the refractive index and absorption of a sample of solidified IP-L 780.

Thanks to Zondy Webber and Kian Shen Kiang for training in the cleanroom.

Thanks to Ben Mills for granting me access to the critical point dryer in the fast lab and advice on how to use it.

Thanks to Jonathan Woods for discussions and criticism.

Declaration

I, Alan Forrester, declare that this thesis "Towards fabrication of optomechanical actuators by two-photon polymerisation" and the work presented in it are my own and has been generated by me as the result of my own original research. I confirm that:

This work was done wholly or mainly while in candidature for a research degree at this University;

Where any part of this thesis has previously been submitted for a degree or any other qualification at this University or any other institution, this has been clearly stated;

Where I have consulted the published work of others, this is always clearly attributed;

Where I have quoted from the work of others, the source is always given. With the exception of such quotations, this thesis is entirely my own work;

I have acknowledged all main sources of help;

Where the thesis is based on work done by myself jointly with others, I have made clear exactly what was done by others and what I have contributed myself;

None of this work has been published before submission that I have the authority to make this agreement, and to hereby give the University of Southampton the right to make the thesis and research data (if any) available in the way described above;

that any errors or omissions in the content of the thesis and research data (if any) will be my responsibility as the author;

that I have exercised reasonable care to ensure that the thesis is original, and to the best of my knowledge, neither it nor the research data (where deposited) infringe upon anyone's rights, including copyright and related rights;

that my research was not sponsored/part-sponsored by or carried out in collaboration with an industrial or other organisation or if it was then their written permission to publish the thesis and research data (if any) is attached to this permission;

that the thesis and research data (if any) do not include confidential information belonging to another individual or organisation or if it does then their written permission for its publication is attached to this permission.

Chapter 1

Introduction

This thesis discusses progress made in the direction of producing mechanical actuators controlled and powered by light. The objective was to make optical devices that would expand or contract in a quasi-static manner when illuminated by light of a particular wavelength.

Light carries momentum and can impart some or all of that momentum when it interacts with an object by reflection, or absorption or refraction. As a result, the object interacting with the light may experience a force.

Optical forces have been used to manipulate microscopic objects in optical tweezers by focusing a laser beam tightly and using the resulting gradient force to manipulate microscopic objects [1]. There have also been theoretical studies of using arrays of reflectors to manipulate dielectric objects [2–4]. However, light can also be concentrated by interference effects within specially designed systems with feature sizes related to the wavelength of the light undergoing the interference. This concentration of intensity might produce optical forces within such systems so that they change shape when they are illuminated. The objective of the project was to make a device that would change shape by harnessing this effect.

An optical actuator might be useful for lab-on-a-chip systems. Lab-on-a-chip systems are systems with micron scale features that can be used to perform experiments. A lab on a chip can enable more controlled experimentation with drugs on single microbes and also enable high throughput testing of drugs [5]. Controlling devices on a chip optically might enable contactless experiments and allow the chip to be adapted to perform more than one type of experiment. For example, by changing the wavelength and intensity of the light being used interactions with the material on the chip can be tuned [6]. Optical valves have been made on chips and controlled by laser light by moving components using optical forces, such as those described in [7, 8]. An optical actuator would change shape instead of being moved by light and its motion might depend on the wavelength of the laser used to illuminate it.

1.1 Background

We will start by considering some technologies that might be used to produce large internal intensity gradients.

Metamaterials consist of subwavelength two-dimensional structures composed of both dielectrics and metals that are typically arranged on a plane or in a small number of

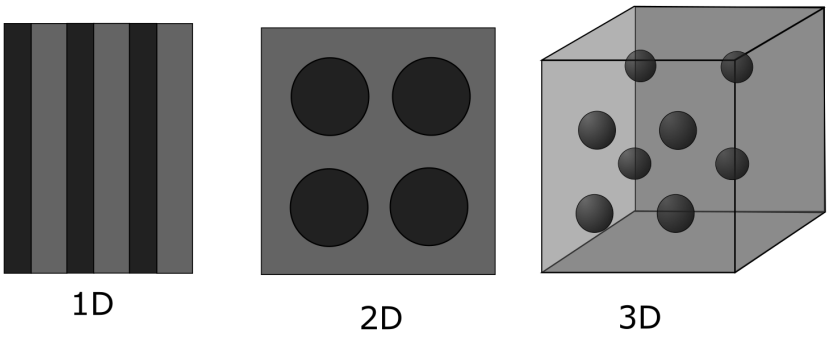

Figure 1.1: Photonic crystals with materials of different refractive indices arranged in 1D,2D and 3D.

layers to produce novel optical effects, such as reflection without phase change [9]. Since these effects tend to depend on having flat structures arranged in two dimensions, it is not clear how they could be used to make actuators.

Photonic crystals consist of combinations of dielectrics of different refractive indices in controlled patterns with subwavelength feature sizes that produce interference effects [10]. These patterns can be arranged in 1D, 2D or 3D as illustrated in 1.1. Such structures can move in directions other than those in the plane of the substrate which they rest. This does not make them promising candidates for optical actuators.

If a photonic crystal is periodic, then its reflectivity will, in general, depend on the wavelength of light incident on it and the angle of incidence. A mode at which the crystal has high reflectivity decays exponentially in the crystal: an evanescent mode.

A photonic crystal can be designed to be periodic with a defect: a region in which the periodicity is broken. A mode that is evanescent in the periodic region may be able to exist in the defect. The periodic regions act like mirrors confining the mode to the defect. Such effects can lead to light being concentrated in a defect when the light has a suitable wavelength. These modes have a complex frequency $\omega_0 - i\gamma/2$ that decay over time as $e^{-\gamma t/2}$ [10, Chapter 7]. The quality factor of such a crystal, given by ω_0/γ is a measure of how long the mode is confined and of the mode's width at half maximum.

There is a large literature on how to predict the intensity distribution in photonic crystals [11–13, 13–24], and how to design photonic crystals to have a high quality factor at a specific wavelength [25, 26]. Photonic crystals with high quality factors have also been manufactured and states of localised intensity have been observed as predicted [17, 27]. There have also been theoretical and experimental studies of localisation of intensity in aperiodic photonic crystals, see the review in [28].

Gradients of intensity can give rise to optical forces, so a photonic crystal could experience internal forces as a result of being illuminated with light of a suitable wavelength [29–32]. Optical forces in photonic crystals have been used to make optical mechanical resonators that have been used for optical cooling [33] and quantum information [34].

The direction we pursued to make optical actuators was to make photonic crystals that would undergo large quasi-static mechanical changes when illuminated rather than function as resonators. These crystals were made using the Nanoscribe: a device capable of making structures with feature sizes of the order of 100nm using two-photon polymerisation [35].

The Nanoscribe uses two-photon polymerisation to write structures with sub-micron resolution. In the research described in this thesis, the Nanoscribe uses a resist that can change state from liquid to solid as a result of chemical reactions when illuminated with light of a suitable wavelength. This transition happens as a result of the formation of radicals at a rate that depends on the square of the intensity of the illumination. This dependence on the square of the intensity occurs because the radicals are produced by an electronic transition that only takes place when the molecule absorbs two photons. This dependence of the reaction rate on the square of the intensity causes the state change to take place only in a region concentrated around the focus of the laser beam. As a result, the Nanoscribe can be used to make structures with sub-micron feature size. The Nanoscribe has been used to make photonic crystals such as woodpiles [36–44] or Bragg stacks [45] so manufacturing such structures with the Nanoscribe is possible.

1.2 The structure of this thesis

Making optical actuators requires making structures with particular sub-micron feature sizes. So the first chapter of this thesis describes the polymerisation process, the processing of samples and the feature size that can be achieved. The feature size is characterised as a function of the power of the laser beam and the speed with which the focus is moved for a particular resist IP-L 780. This information is necessary for designing the structures made using that resist .

The change in shape that can be expected from a structure depends on the mechanical properties of the material of which it is composed. The next chapter describes experiments conducted to measure the Young's modulus of the polymer produced by illuminating a particular resist. The results of this measurement are of the same order of magnitude as those produced by Nanoscribe. This chapter also considers issues arising from measuring the dimensions of the structures made to measure the Young's modulus, and discusses non-linear effects.

Chapter 4 describes experiments conducted to manufacture Bragg stacks with the Nanoscribe and test their optical properties. This chapter explains some principles that should be followed when designing structures made using two-photon polymerisation. The optical tests are consistent with some of the structures tested functioning as Bragg stacks.

Chapter 5 explains the conclusions of the research described in the thesis and suggests further lines of research. The appendices give some details of the work that were not included in the main thesis.

Chapter 2

Characterisation of the size of voxels

2.1 Introduction

To produce the microscopic structures for our experiments, we used a device produced by Nanoscribe GmbH: the Photonic Professional GT [39], henceforth referred to as 'the Nanoscribe'. The Nanoscribe is a very high-resolution 3-D printer that 'writes' arbitrary 3-D structures by multi-photon photopolymerization of a transparent resist.

The Nanoscribe operates by scanning the tight focus of a 120fs, 780nm, 100MHz repetition rate pulsed fibre laser into a sample of an unpolymerized resist through the thin glass coverslip that supports it. The position of the focus of the laser within the resist in the horizontal plane is controlled by piezo-electric actuators which move the microscope stage in the horizontal plane (parallel to the coverslip) with a resolution of 1 nm and a maximum travel distance of 300 microns. The position of the focus of the laser in the vertical plane (perpendicular to the coverslip) is controlled by changing the position of the optics that focus the laser beam relative to the sample using piezo-electric actuators to change the position of the focus in that plane with a resolution of 1 nm. The piezo electric actuators, the laser and the optics are controlled by a computer running an application designed by Nanoscribe. For a schematic illustrating how the writing process is controlled by moving the objective and the stage, see Figure 2.1.

The Nanoscribe finds the position of the sample by reflecting a laser off a transmission grating and then detecting the resulting reflection using a CCD [46]. A schematic of the optics used to do this is shown in Figure 2.2. The illumination optics focus the reflected light from the grating onto a plane where the lower surface of the substrate would be if the objective was in the right position. The imaging optics focus any light reflected from that plane onto the CCD. The position of the objective is adjusted until the reflected image of the grating is detected at its maximum intensity.

To make the structures described in this thesis IP-L 780 was used: a proprietary resist developed by Nanoscribe. The resist starts as a liquid and solidifies where the laser is bright enough by the process of radical chain polymerisation. Other resists that have been used for direct laser writing include SU-8 from Microchem Corporation, IP-S, IP-Dip and IP-G from Nanoscribe, Ormocore b59 from Micro Resist Technology GmbH, SZ 2080 from Forth, AKRE19, SCR500 and PEG-DA-258 [39, 47–50]. The minimum feature size the Nanoscribe fabricated with IP-L 780 in these experiments was around 150 nm in the horizontal plane and approximately 400nm in the vertical plane. These dimensions match what Nanoscribe has reported for this resist [35].

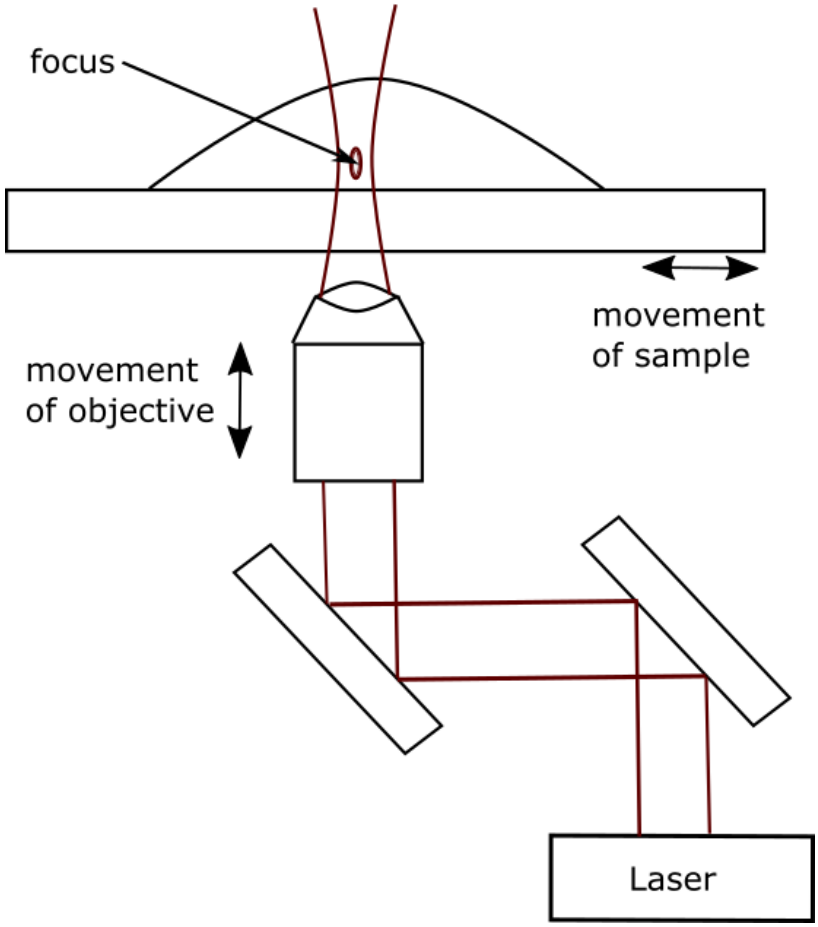

Figure 2.1: A schematic of the optics used to control the position of the focal point of the beam in the IP-L 780.

Although Nanoscribe provides a general specification for its device performance, little has been published about how it is determined by the physical and chemical mechanisms of exposure and photopolymerization [39, 46, 51–55], and details of the proprietary photoresist IP-L780 are scant. Since the performance and characteristics of the Nanoscribe and resist affect the structures that we can produce, this chapter describes our studies to characterize the performance of the Nanoscribe device. The 3-D resolution was measured under different conditions. The results are compared to simple models of the exposure and polymerization processes.

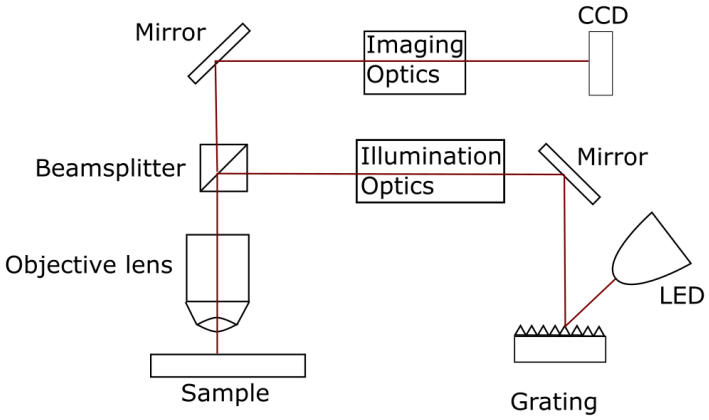

Figure 2.2: A schematic of the optics used to detect the position of the sample.

2.2 The polymerisation process

The following description of radical chain polymerisation follows [56, Chapter 3]. Chain polymerisation starts with a compound I called an initiator, which undergoes a process called initiation to produce a reactive species $R*$. The reactive species then bonds to a monomer by opening a double bond in the monomer. The monomer then becomes reactive and bonds itself to another monomer in the same manner and makes that monomer reactive. The new reactive monomer then bonds to another monomer and so on:

$$\begin{aligned} &I \xrightarrow{x} nR*, \\ &R* + M \rightarrow M_1*, \\ &M_1* + M \rightarrow M_2, * \\ &M_2* + M \rightarrow M_3* . \\ &\dots \end{aligned} \tag{2.1}$$

In these equations I stands for the initiator, M stands for a monomer, x stands for the initiation process and M_j* stands for a reactive species with j monomer subunits.

This process continues until it is terminated by a reaction. The details of the termination reaction depend on details of what type of reactions the reactive version of the monomer can undergo and the reaction conditions in the particular case in question. Chain polymerisation often terminates by two reactive monomer chains reacting with one another. Chain polymerisation can also terminate by a radical from one molecule being transferred to another molecule resulting in two separate non-radical molecules [56, Section 3-3a].

In two-photon polymerisation, the polymerisation process is initiated by two-photon absorption. In single-photon absorption, a molecule absorbs a single photon and one of its electrons goes from a stable ground state to some final state, both of which are energy eigenstates of the molecule. In two-photon absorption, a transition from the ground state to the final state can arise by the molecule absorbing two photons whose energies add up to the energy required for the transition. The first photon produces a virtual state whose lifetime is of the order $\hbar/\Delta E$ where ΔE is the difference between the energy of the photon interacting with the molecule and the nearest energy eigenstate of the molecule [57]. If the molecule absorbs a second photon of the right energy during that lifetime, then the electron may make the transition to the higher energy level. In the process used by the Nanoscribe, the energy of the photon is half of the energy

required for the transition, so $\hbar/\Delta E = \hbar/\Delta E_p = 2\pi\lambda/c \approx 10^{-14}$s, where E_p, λ are the photon energy and wavelength respectively. In two-photon polymerisation, the final energy eigenstate after two-photon absorption is one in which the electron has left the molecule: this produces the initial reactive species, which then leads to the process described above.

The polymerisation takes place only in regions near the focus of the laser beam in which radicals are produced, or in regions to which those radicals diffuse. In other regions of IP-L 780, the radicals are not present and so the reaction does not take place. A solidified piece of polymer in such a region is the minimal structure that is composed to make a structure using the Nanoscribe, so it is called a voxel (volume pixel) in analogy to the way pixels are used to build up images on a computer or television screen.

The formation of voxels exhibits a threshold behaviour: if the production of radicals is below a certain threshold, no voxel is produced. It is suspected that although radicals may be produced they do not lead to significant polymerisation because they react with oxygen dissolved in the resist and do not polymerise [54, 58, 59]. Some resists also have quenchers that are introduced to suppress the reaction unless the concentration of radicals exceeds some threshold, as explained in [60].

The laser beam in the resist is a Gaussian beam to a good approximation. When a structure is written with the Nanoscribe the focus of the laser beam moves. The faster the focus moves at a given power, the fewer radicals are produced in a voxel volume. If the focus moves quickly enough at a given power, no structure will form because the rate of radical production will be below the threshold required to remove the oxygen from the resist faster than it diffuses into the voxel region. Since the speed at which the beam moves will change the number of radicals in a given volume it should also change the dimensions of structures being written. The speed and pattern in which a given structure is written is determined by a program written in a specialised language created by Nanoscribe GmbH, which is described in Appendix A.

The time needed for the polymerisation reaction is typically of the order of 0.1-1ms [54], which is far longer than the lifetime of the virtual state or the duration of an individual pulse. As a result, the time taken for the pulse or the formation of the radical can be neglected in any discussion of how the reaction affects the size and shape of the structures. Other effects, such as diffusion or the number of pulses that propagate through a voxel sized region, may change the size and shape of structures.

2.3 Models of variation of width and height with velocity

This section describes structures that were made to measure the feature size produced by the Nanoscribe under a range of writing conditions. The experiment involves making blocks and drawing lines between them, as illustrated in figure 2.3. Each pair of blocks was made with the same settings: the laser power was 12 mW and the focus was moved at a speed of 25 μms^{-1}. The power and speed of the laser focus were changed for each line drawn between a pair of blocks. So while the blocks were identical the lines were not.

This section describes previous experiments for measuring feature size in two-photon polymerisation systems. Accounts are given of previous models developed attempt to explain and predict the results of two-photon polymerisation of voxels and lines. Then a model for predicting the width of lines in structures of the kind shown in figure 2.3 is given.

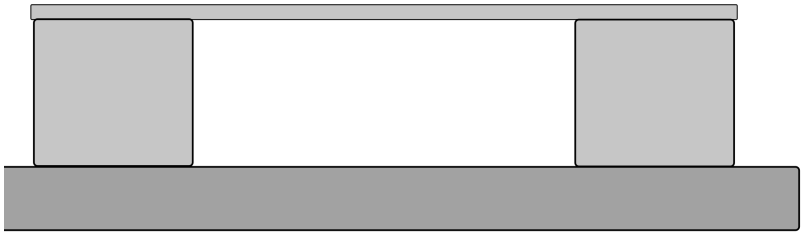

Figure 2.3: Two blocks with a single line drawn across the top of them viewed from the side.

2.3.1 Previous models and experiments

Previous experiments have been conducted to measure the resolution that can be achieved by two-photon polymerisation. Some experiments have measured the size of individual voxels [60–67]. These experiments involved moving the waist of the laser beam perpendicular to the substrate until the voxel stopped sticking to it. The distance at which the voxel stopped sticking to the substrate gave an estimate of the voxel's vertical size. Each voxel was exposed for some period controlled by the experimenter. The voxel size increased with exposure time and Tanaka found that the voxel size shows a straight line trend when plotted versus the logarithm of the exposure time for a given laser power [63] .

In the experiments described above, each voxel sized region is exposed for a time that is inversely proportional to the speed at which the focus moved. So the result corresponding to that of [63] would be for the voxel size to vary exponentially with velocity with a negative exponent, as in equation (2.3). The same kind of experiment and its results were described in [48]. In [48] a physical model of voxel formation was also proposed and the predicted width and depth of the voxel was given as

$$\begin{aligned} y_S &= \frac{w_0}{2}\sqrt{\log\left(\frac{\sigma_2 N_0^2 \nu \tau_i \tau_L}{c_r}\right)}, \\ z_S &= 2z_r\sqrt{\left(\frac{\sigma_2 N_0^2 \nu \tau_i \tau_L}{c_r}\right)^{1/2} - 1}, \\ c_r &= \log\left(\frac{C_0}{C_0 - C_T}\right), \end{aligned} \tag{2.2}$$

where C_0 is the initial concentration of the initiators, C_T is a threshold concentration of initiators below which no structures form, z_r is the Rayleigh range, N_0 is the photon flux, ν is the repetition rate of the laser, τ_i is the total time for which the voxel is irradiated, and τ_L is the laser pulse duration. This equation was derived from a rate equation (2.4) that will be discussed in Section 2.3.2 where it is used to derive a model of the structures made to test the variation of feature size under different writing conditions.

Other experiments involved measuring the width of lines drawn using two-photon polymerisation [68–71]. As in the experiments described above for voxels, the width of the lines increased with increasing power and decreased with increasing speed. The experimental data were fitted to the following function:

$$y_K = \xi(1 - \exp(-\phi v)), \tag{2.3}$$

where ξ, ϕ are functions of the laser power. No explanation was given for why the width of a voxel or line should vary with velocity according to this equation.

2.3.2 Physical model of voxel formation

In this subsection, the polymerisation process is modeled by supposing that the concentration of initiators is proportional to the square of the intensity of the laser beam, and that where the concentration is above a threshold value, the IP-L 780 solidifies. This threshold behaviour may be a result of oxygen dissolved in the resist [54, 58, 59]. This model effectively assumes that there are no loss mechanisms other than polymer formation. For example, neither the radicals nor bonded chains of monomers diffuse out of a voxel sized exposed region during voxel formation.

In the experiments to test the feature size of the Nanoscribe we were drawing a single line in the horizontal plane. As a result, the cross section of the line should have the same shape as the region of a beam in which the square of the intensity is above some threshold. That threshold would depend on both the power and the velocity at which the focus moves, as described below. However, we can calculate the shape of that region by considering where the square of the intensity of a laser beam hits particular thresholds for a Gaussian beam with wavelength 780nm focused by a lens of numerical aperture 1.4 propagating in the positive z direction, as shown in Figure 2.4. The shape is approximately elliptical, so we can treat the cross section of the line as elliptical. Note that Figure 2.4 shows the beam very close to the focus and so it does not have the same shape as a beam being shown propagating a very long distance compared to the Rayleigh range as in Figure 2.1.

Suppose that the laser beam produces the radicals and that the radicals then react to form the polymer with no other processes taking place. The concentration of the radicals may be described by a function of position and time $C(x, y, z, t)$ governed by a rate equation [48]:

$$\frac{\partial C}{\partial t} = (C_0 - C)\sigma_2 N^2, \tag{2.4}$$

where $\sigma_2 = \sigma_2^a \nu$ is the effective two-photon cross section, which is the product of the σ_2^a the two-photon cross section of the initiator and ν the efficiency of initiation. The photon flux is $N(x, y, z, t) = I(x, y, z, t)/E_p$, where E_p is the energy of a single photon and C_0 is the initial density of the initiator. The rate of radical production depends on $C_0 - C$ because that is the remaining concentration of the polymer after a reaction has produced a concentration of radicals C.

The region in which polymerisation will take place is bounded by a surface on which the concentration of radicals is at some threshold value C_T. To obtain an expression for that surface, we must find a solution for the concentration C near that surface using (2.4). Unless that threshold value is very close to the concentration of radicals in IP-L 780, the second term in equation (2.4) will be negligible at the boundary compared to the first term because at the threshold most of the radicals have undergone a reaction. So the integral will be approximated by

$$C \approx C_0 \sigma_2 \int_0^\tau N^2 dt, \tag{2.5}$$

on the understanding that this expression is only being used to find the boundary.

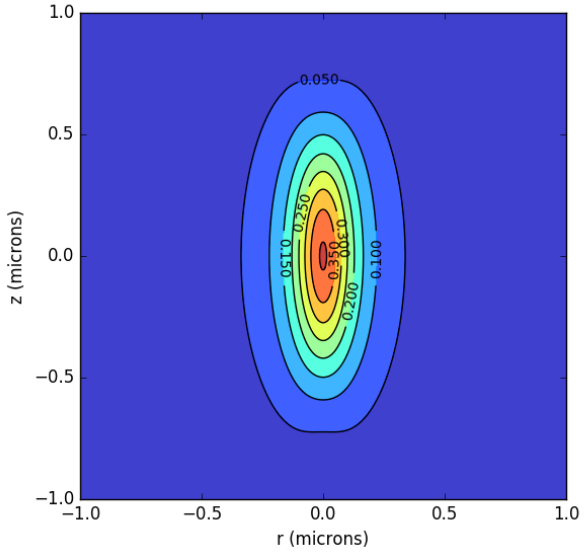

Figure 2.4: The square of the intensity of a Gaussian beam with wavelength 780nm focused by a lens of numerical aperture 1.4 normalised so that the intensity at the origin is 1. The numbers say how large the squared intensity is at the relevant contour. The direction of propagation is the positive z direction.

The intensity of a Gaussian beam whose focus is at the origin is given by

$$\begin{aligned} I(r,z) &= \frac{2P}{\pi w^2(z)} \exp\left(-\frac{2r^2}{w^2(z)}\right), \\ w_0 &\approx \frac{\lambda}{\pi \mathrm{NA}}, \\ w(z) &= w_0\sqrt{1+\frac{z^2}{z_r^2}}, \\ z_r &= \frac{\pi w_0^2}{\lambda}, \end{aligned} \tag{2.6}$$

where NA is the numerical aperture of the objective lens focusing the laser beam, w_0 is the beam waist, $r = \sqrt{x^2+y^2}$ is the distance from the focus of the beam, which is propagating parallel to the z axis, and λ is the wavelength of the laser.

Consider two distinct points $Q = (x, y, z)$ and $Q' = (x', y', z')$. A laser beam whose focus is at Q' will generate some radicals at Q: the magnitude of the contribution would be proportional to the intensity square of the beam focused on Q' at Q:

$$I^2(Q,Q',z) = \frac{4P^2}{\pi^2 w^4(z-z')} \exp\left(-\frac{4((x-x')^2+(y-y')^2)}{w^2(z-z')}\right). \tag{2.7}$$

Suppose that the Nanoscribe writes a line of length L and that the time the beam takes to move along the line is small compared to the time over which the reaction takes place. As a result, the laser beam at every point on the line contributes to the concentration of initiators at every other point on the line. To find the width and depth of the line, we must then integrate over the entire line to get the concentration at each point. Using (2.5), if the beam moves at a constant velocity with speed v in the x direction we have

$$\begin{aligned} C_{vx}(x,y,z,t) &= \int_0^{L/v} \frac{4C_0\sigma_2 P^2}{\pi^2 w^4(z)\nu^2 E_p^2} \exp\left(-\frac{4((x-vt)^2+y^2)}{w^2(z)}\right) dt, \\ &= \frac{C_0\sigma_2 P^2}{\pi^{3/2} v w^3(z)\nu^2 E_p^2} \exp\left(-\frac{4y^2}{w(z)^2}\right)\left(\mathrm{erf}\left(\frac{2x}{w(z)}\right) - \mathrm{erf}\left(\frac{2(x-L)}{w(z)}\right)\right). \end{aligned} \tag{2.8}$$

A similar expression would hold if the focus were moving in any direction in the x, y plane.

Polymerisation takes place if the concentration is above the relevant threshold: $C_{vx1}(x, y, z, t) > C_T$. In the x, y plane $w(z) = w_0$, so for $2w_0 < x < L$, the term featuring error functions in x is approximately equal to 2 since $\text{erf}(m) \approx \pm 1$ for $m > 2, m < -2$ respectively. The blocks might in principle change the concentration near them because the beam may be unable to generate radicals inside the blocks. This is realistic for any portion of the line that is not on the blocks since they are cubes with sides larger than two microns and beam waist is approximately 0.2 microns. Away from the x, y plane $w(z)$ increases with z and so the x dependent term decreases in magnitude. The line size in the y direction in the x, y plane will be the maximum width of the line parallel to the x, y plane. The value of y for which $C_{vx}(x, y, z, t) = C_T$ in the x, y plane and in the interval $w_0 < x < L$ will be

$$y_T = \frac{w_0}{2}\sqrt{\log\left(\frac{P^2}{v}\frac{C_0\sigma_2}{\pi^{3/2}w_0^3 C_T \nu^2 E_p^2}\right)}. \tag{2.9}$$

The error function term will be constant with value two if $2x/w(z_T) > 2$ so that $x > w(z_T)$. The Rayleigh range is 279 nm, so if $z_T = 1\mu$m, then $w(z_T) = 934nm$. So at any point more than one micron away from the blocks, the error term has value two. The maximum concentration will be along the line $y = 0$ in the z direction so the equation to be solved is

$$C_T = \frac{C_0\sigma_2 P^2}{\pi^{3/2} v w^3(z_T)\nu^2 E_p^2}, \tag{2.10}$$

which gives

$$z_T = z_r\sqrt{\frac{C_0^{2/3}\sigma_2^{2/3}}{\pi w_0^2 C_T^{2/3}\nu^2 E_p^2}\left(\frac{P^2}{v}\right)^{2/3} - 1}. \tag{2.11}$$

Since the model used in this section is adapted from [48] the expressions given by the two models will be compared. The time for which a voxel sized region would be exposed in the model described in this section would be voxel size/v. The equations for y_S and y_T have different constants but are both functions of the form $f\sqrt{\log\left(\frac{P^2}{v}g\right)}$ where f, g are constants. The equation z_S is of the form $\alpha\sqrt{\left(\beta\frac{P^2}{v}\right)^{1/3} - 1}$ while z_T is of the form $\alpha\sqrt{\left(\beta\frac{P^2}{v}\right)^{2/3} - 1}$ and the constants are not the same either.

The width of a voxel is of the order 0.1 microns. The speed at which the laser beam moves is between 25 and 400 micron/s in the experiments reported here. So the time it takes the laser beam to move across a region of the size of a voxel is approximately 0.25-4 ms. Measured values for reaction times for various resists for two-photon polymerisation range from 0.16-1.9ms [54]. So the time taken to pass through the region of a voxel on higher speeds is similar to the reaction time for quickly reacting resists. At lower speeds, the time taken to pass through a voxel region is greater than the reaction time taken for even the slowest reacting resists. So the range of speeds chosen seems well adapted to test the extreme ends of the range of reasonable writing parameters.

2.4 Experimental test

To test the theory the expressions for y_T, z_T, y_K, z_S were compared to experimental measurements of these quantities.

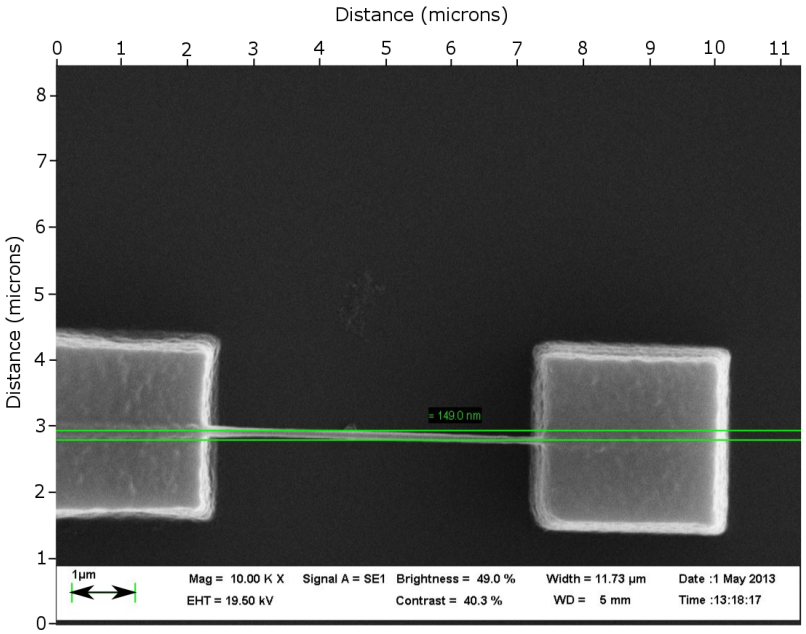

Figure 2.5: SEM image of line drawn between two blocks. The blocks were designed, made and imaged by the author.

Structures were made that consisted of two cubes designed to have side three microns facing one another with a line drawn between their upper surfaces, see Figure 2.5. The cubes were made by drawing lines 150 nm apart in layers with the laser at a standard speed and power so that all of the blocks were as similar as possible. The blocks were designed to be three microns in size and were placed five microns apart. So a given line would be 11 microns long in total, with five microns of its length between the blocks. The region of the line 2 microns away from both blocks should be well described by equations (2.9) and (2.11). Lines were drawn at a range of different settings of speed and laser power. The Nanoscribe measures the laser power before the beam goes into the sample.

After the polymerisation ceased, the unpolymerised polymer was removed by immersing the sample in isopropanol and then removing the isopropanol. Removing liquid from a microscopic structure can damage the sample as a result of forces exerted by surface tension.

Surface tension is a fairly well-known problem that can be solved by supercritical drying with carbon dioxide, which has been applied to electronics, MEMS and producing polymerised structures [72–74]. The critical point is a point on the phase diagram of a chemical where the liquid and gas phases become indistinguishable. For temperatures and pressures greater than those at the critical point the chemical is said to be supercritical. The chemical can then pass from a liquid to a gas state without going through a phase transition that would create surface tension. Carbon dioxide can be put into a liquid state by keeping it at about 50 bar at 10°C. The critical point for carbon dioxide is at 74 bar and 31°C. So if the isopropanol is replaced by carbon dioxide at 50 bar at 10°C then the pressure can be increased to 74 bar and the temperature raised to 31°C to achieve the critical point drying effect.

This critical point drying process was carried out using a Quorum critical point dryer. The dryer has a vessel that can be pressurised to 74 bar. The sample was placed in this vessel with some isopropanol which is then cooled to 10°C or less. Carbon dioxide was then pumped into the chamber until the pressure reached 50 bar from a high-pressure cylinder of carbon dioxide. The temperature of the vessel was reduced by adiabatic expansion of liquid carbon dioxide from the high-pressure cylinder in a region in thermal contact with the high-pressure chamber so that the temperature would remain

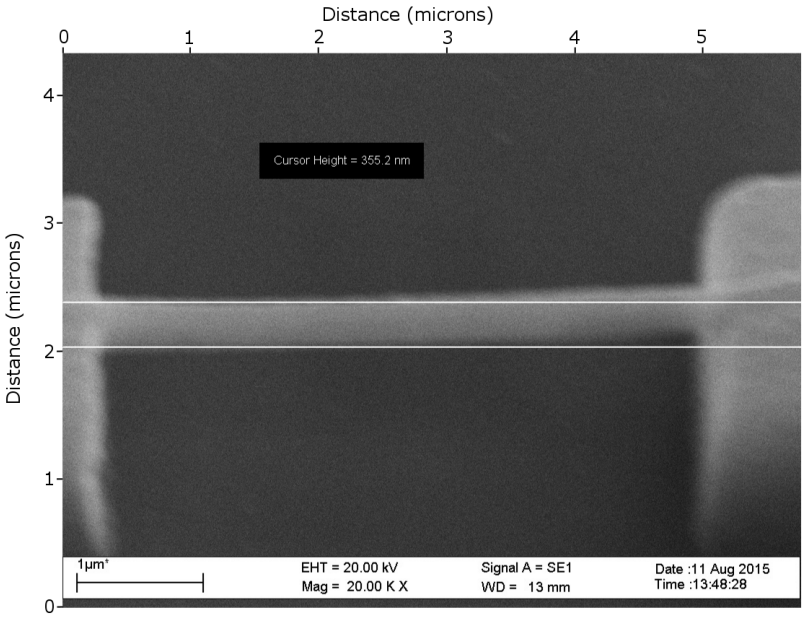

Figure 2.6: SEM image of blocks tilted at an angle of 45 degrees. The blocks were designed, made and imaged by the author.

low and the carbon dioxide in the vessel would be in a liquid state. The isopropanol was gradually bled out of the chamber and replaced by liquid carbon dioxide. When all the isopropanol had been replaced, the pressure was increased by pumping more carbon dioxide into the chamber. A heating element was then used to increase the temperature so that the carbon dioxide became supercritical and could be bled off without damaging the sample.

The width of the lines was then measured. The sample was coated with 5-10 nm of gold. It was placed in a scanning electron microscope (SEM), which was focused on the line at a magnification of 20,000. The width of the line was then measured with the SEM software.

The depth was found by measuring the apparent depth d_θ of the line with the sample tilted at an angle of θ with the SEM, as illustrated in Figure 2.6, and then calculating the depth in z from that measurement.

We assume that the voxel has an elliptical cross-section, as illustrated in figure 2.7. The width of the voxel as seen by the observer at angle θ is given by D_θ. The tilted ellipse is described by the equation:

$$\left(\frac{\cos\theta x - \sin\theta y}{w/2}\right)^2 + \left(\frac{\sin\theta x + \cos\theta y}{h/2}\right)^2 = 1, \tag{2.12}$$

where w, h are the width and height of the voxel respectively. The lines at constant x that intersect the ellipse at only one point are at $x = \pm D_\theta/2$. Substituting $x = D_\theta/2$ into the equation for the ellipse gives a quadratic in y which has a unique solution if

$$D_\theta = \pm\sqrt{\tfrac{1}{2}(w^2(1+\cos 2\theta) + h^2(1-\cos 2\theta))}. \tag{2.13}$$

If $\cos 2\theta \neq 1$, i.e. $\theta \neq 0, \pi$, then h is given by

$$h = \sqrt{\frac{2D_\theta^2 - w^2(1+\cos 2\theta)}{1-\cos 2\theta}}. \tag{2.14}$$

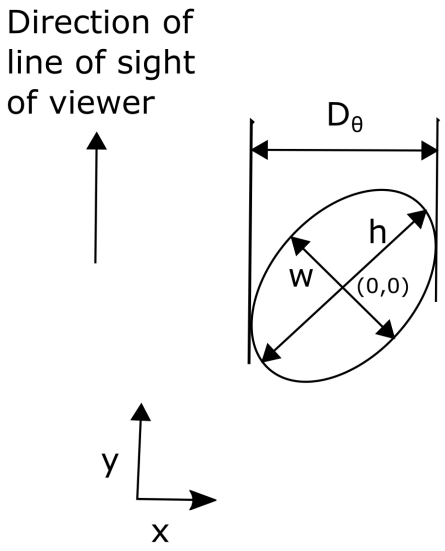

Figure 2.7: Elliptical voxel viewed from an angle: d represents the depth of the voxel as viewed by the observer. The x and y axes are chosen to be oriented along the axes of the ellipse.

The measurements of y_T, z_T, y_K, z_S were fitted to the equations:

$$\begin{aligned} y_T &= f\sqrt{\log\left(\frac{P^2}{v}g\right)}, \\ z_T &= \alpha\sqrt{\left(\beta\frac{P^2}{v}\right)^{2/3} - 1}, \\ y_K &= \xi(1-\exp(-\phi v)), \\ z_S &= \zeta\sqrt{\left(\psi\frac{P^2}{v}\right)^{1/2} - 1}. \end{aligned} \tag{2.15}$$

If the model is correct, then there should be values of f, g that are the same for all of the data. The fits were done in two ways. First, the data were divided into five different sets, one set for each power. The data were then least squares fitted as a function of the speed at which the focus moved for each data set separately. Second, the data were fitted in a single data set as a function of $\frac{P^2}{v}$. If the model is accurate these two methods should give similar results.

The width and depth of the lines as measured by the SEM were not perfectly uniform along the line, they varied by approximately 10nm. These non-uniformities were larger than the minimum change in width that could be measured by the SEM, so it is the source of errors in measurement of the width. The other errors in the power and speed of the laser are negligible by comparison and so they were omitted from the analysis. The fitted parameters f, g and their errors $\delta f, \delta g$ are given in Table 2.1. The fits and the data are graphed on the same axes in Graph 2.8.

The fit for the line at 12mW did not give an accurate figure for g. For the other lines, the error bounds for g all overlap, so that test does not rule out the above account of how the lines form. The fits for f appear to be more accurate and do not overlap at all, but rather increase as the power increases. This apparently rules out the model explained in the previous section.

Power(mW)	$f(\mu m^2)$	$\delta f(\mu m^2)$	$g(\mu m s^{-1}(mW)^{-1})$	$\delta g(\mu m s^{-1}(mW)^{-1})$
12	0.106	0.007	16	6
14	0.186	0.005	5.4	0.5
16	0.225	0.005	5.2	0.5
18	0.265	0.005	4.7	0.4
20	0.3000	0.005	4.1	0.3

Table 2.1: Measured fitting parameters.

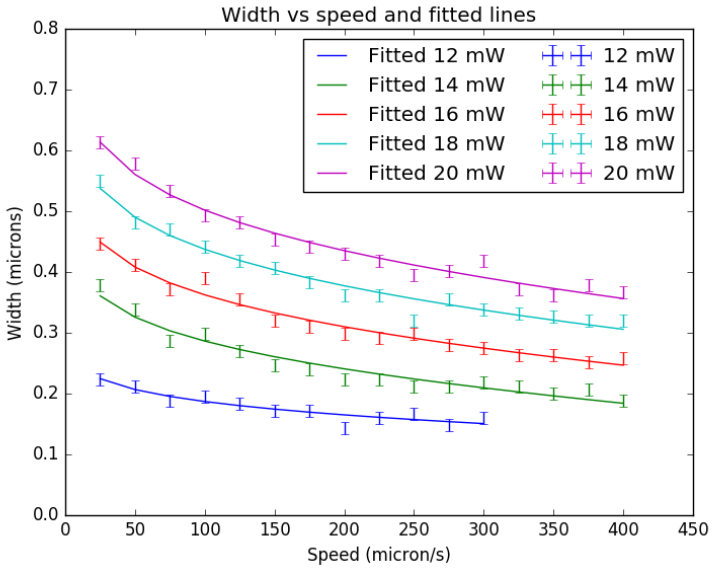

Figure 2.8: The width of a line as a function of velocity, with lines fitted for each individual power.

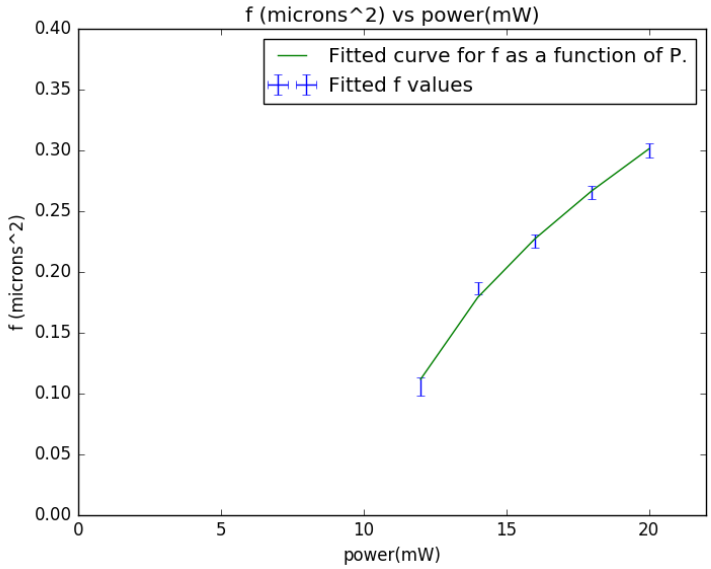

Figure 2.9: The fitted parameter f vs the power in the laser beam (mW).

We fitted the f parameters as the following function of P:

$$f(P) = \sqrt{f_s(P - f_i)}, \tag{2.16}$$

and got the result $f_s = 0.00962 \pm 0.00006 \mu m^4 (mW)^{-1}$, $f_i = 10.61 \pm 0.3 mW$. A plot of f and the fitted curve are shown in as shown in Figure 2.9. The fit to the equation (2.16) for f as a function of P appears accurate. Substituting (2.16) back into the expression for y_T in (2.16), gives:

$$y_T = \sqrt{f_s(P - f_i) \log\left(\frac{P^2}{v} g\right)}. \tag{2.17}$$

There is currently no theoretical motivation for this expression, but experimental data do not rule it out.

Fitting the data as a function of $\frac{P^2}{v}$ gives values of $f = 0.27 \pm 0.04 \mu m^2, g = 3.0 \pm 0.2$, but when the fit is displayed in Graph 2.10 with the data, the fit appears very poor.

The data for the depth, given in Figure 2.11, does not fit either of the expressions given in equation (2.16) for the depth. Scipy [75] was used to try to fit the data to that expression without success. The velocity for a given power varies by a factor of 18. One expression for the depth gives a v dependence of $1/v^{1/3}$, so the difference in depth ought to be a factor of 2.6. The other equation gives a v dependence of $1/v^{1/4}$, so the difference in depth ought to be a factor of 2.1. In reality, the depth is almost flat across that range of velocities. The model with no diffusion explained above is not consistent with the experimental data in Figure 2.11.

Fits of the data above to (2.3) give the fit shown in plot 2.12 and fit parameters are shown in Table 2.2. The data sets for different powers individually fit to an exponential function, but they do not have the same gradient, so the results do not match those measured in [63].

There is no discernible trend in the fitted parameter ϕ for (2.3) , as illustrated in figure 2.13. As such, equation (2.3) cannot be used to make predictions about what would happen at other powers.

The maximum and minimum dimensions of measured lines provide useful information for understanding the scale of structures that can be written. The minimum measured

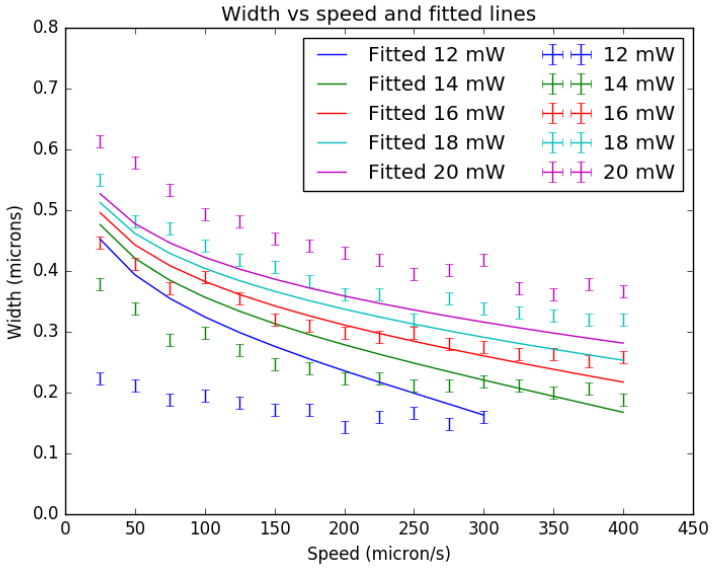

Figure 2.10: The width of a line as a function of velocity with fitted lines for all the data fitted together.

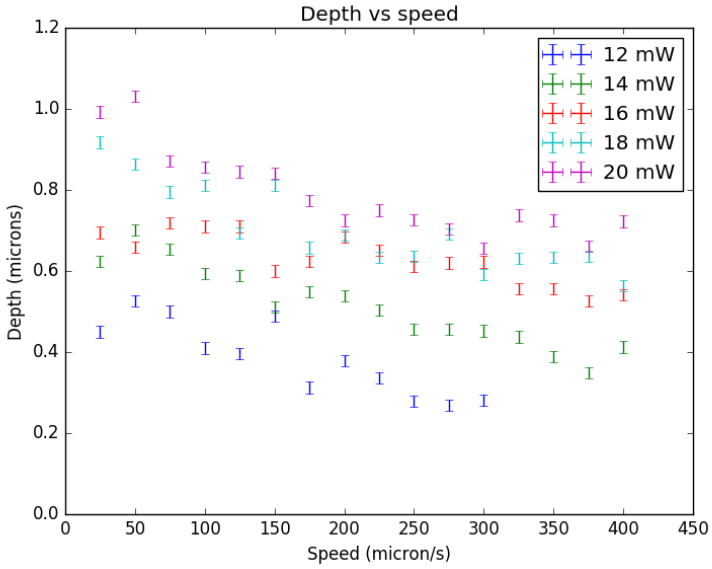

Figure 2.11: The depth of a line as a function of velocity at different powers.

Power(mW)	$\xi(\mu m s^{-1})$	$\delta\xi(\mu m^2)$	$\phi(\mu m s^{-1}(mW)^{-1})$	$\delta\phi(\mu m s^{-1}(mW)^{-1})$
12	0.126	0.004	4.4×10^{-3}	9×10^{-4}
14	0.202	0.006	9×10^{-3}	1×10^{-3}
16	0.241	0.006	6.6×10^{-3}	8×10^{-4}
18	0.295	0.006	7.0×10^{-3}	7×10^{-4}
20	0.329	0.006	6.0×10^{-3}	5×10^{-4}

Table 2.2: Measured fitting parameters.

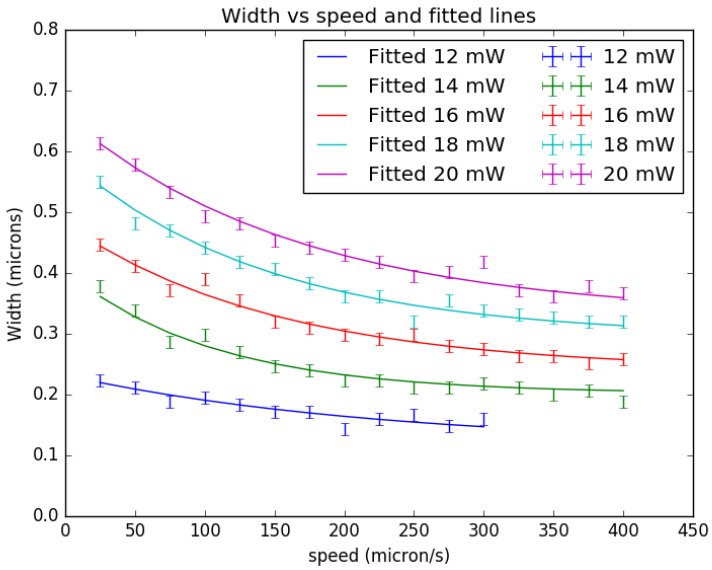

Figure 2.12: The width of a line as a function of velocity with fitted lines for equation (2.3).

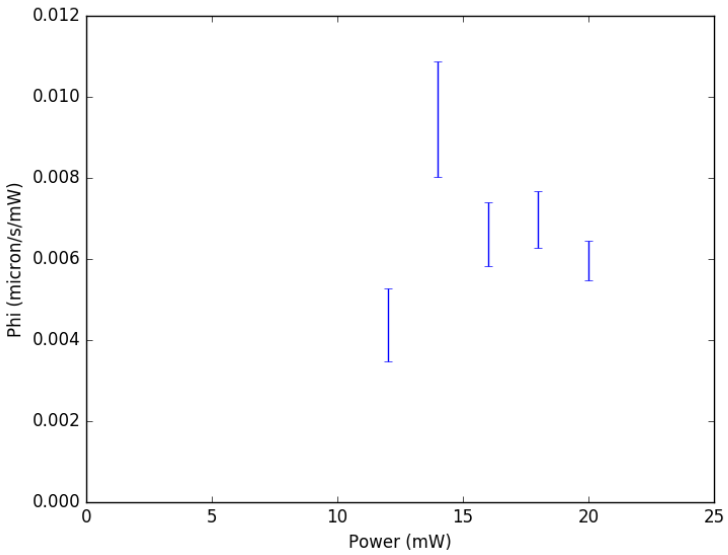

Figure 2.13: The parameters for (2.3) as a function of power in mW.

width of a line is 0.14 microns. The minimum measured depth of a line is 0.23 microns. The maximum measured width of a line is 0.61 microns. The maximum measured depth of a line is 1 micron.

2.5 Discussion

The models given above do not explain the results of the experiments. In this section, we consider what alternative models might explain the results.

The authors of [76] found that samples written near threshold with a zirconium-based sol-gel composite underwent as much as 35% shrinkage. This does not explain the results above for two reasons. First, many of the samples written above were not close to the threshold. Second, the deviation from the model was in the direction of the line being thicker, not thinner.

Processes involving more than two photons might contribute to the voxel size. If the only difference was the number of photons involved then the derivation of (2.9) and (2.11) could be repeated with P^n for $n > 2$ instead of P^2 in (2.9). The equations for an n-photon process are given by:

$$\begin{aligned} y_T &= f\sqrt{\log\left(\frac{P^n}{v}g\right)}, \\ z_T &= \alpha\sqrt{\left(\beta\frac{P^n}{v}\right)^{2/3} - 1}. \end{aligned} \tag{2.18}$$

The expression for z_T for the two-photon process could not be fitted because $1/v$ varied over the range of speeds considered, and these expressions have the same problem.The velocity for a given power varies by a factor of 18 and equation 2.18 has a dependence of $1/v^{1/3}$, so the difference in depth ought to be a factor of 2.6, but experimental data are almost flat. So processes involving more than two photons do not explain the variations in voxel size.

Another possibility is that the radicals underwent reactions other than the polymerisation process at rate k and this somehow led to the results above. The rate equation for the formation of the polymer would then be

$$\frac{\partial C}{\partial t} = C\sigma_2 N^2 - kC. \tag{2.19}$$

A solution to this equation, derived using Mathematica, is given by

$$\begin{aligned} C(x,y,z,t) =& c(x,y,z)e^{-kt} + \frac{\alpha^2 C_0 P^2 \sigma_2}{\sqrt{2\pi}vw(z)}\mathrm{erf}\left(\frac{kw(z)^2 + 4v(x-tv)}{2\sqrt{2}vw(z)}\right) \\ & \exp\left(\frac{k^2 w(z)^2}{8v^2} + \frac{k(x-tv)}{v} - \frac{2y^2}{w(z)^2}\right). \end{aligned} \tag{2.20}$$

There is a problem with this expression even before boundary conditions are imposed. Both $\mathrm{erf}(m)$ and $\exp(m^2)$ are monotonically increasing with m. As a result, both the erf term and the exp term in the equation above are monotonically decreasing with v. The term in front of those expressions is dependent on P^2/v, and so its P, v dependence if fitted would be similar to the fit for the model described in the previous section. Since one of the problems with that model is that the depth decreases too rapidly as a function of v, this model cannot fix that problem since it adds factors that decrease as a function of v.

There is another explanation that has not been eliminated. Pikulin and Bityurin [59,77] have argued that a lower limit on feature size for two-photon polymerisation may be imposed by diffusion. The radicals diffuse while they are reacting to produce the polymer so that the minimum feature size is set by how far the radicals diffuse in addition to the beam waist, the power and the speed at which the focus moves. To pursue this line of investigation further, it would be necessary to devise and perform experiments to discover the diffusion constants for the radicals. It would then be necessary to derive and solve an equation involving the effects of diffusion and chemical reactions. Some experiments have been performed and modelled for other polymers that can be used for direct laser writing [54]. The experiments involved measuring the light scattered by a voxel as a result of the difference in refractive index between the solid polymer and the resist. Similar experiments could be performed with IP-L 780 and other resists.

The absence of a model predicting the variations in voxel width and depth with power and speed is an unsolved problem. Expressions that fit the measured widths of voxels well and values for the parameters in those expressions have been found. We found a phenomenological model that is compatible with experimental data for the width described by the equation (2.17).

In addition, the observations described in this chapter provide information on the dimensions of voxels that is useful for designing structures. The minimum and maximum measured widths of a line are 0.12 microns and 0.61 microns respectively. The minimum and maximum measured depths are 0.61 and 1 microns respectively. Any attempt to draw voxels that are closer than the voxel sizes described above will not produce distinct structures. So to draw distinct structures, the voxels composing those structures have to be farther away than one voxel width. Conversely, a strong structure will presumably have voxels that overlap significantly so that they adhere to one another. The observations described above provide information on how close voxels have to be to overlap, and so provide information on how to produce strong structures.

Chapter 3

Characterisation of mechanical properties

Making actuators using the Nanoscribe requires making structures out of the Nanoscribe polymer that will remain intact when subjected to optical forces. The Young's modulus of the polymer is required to make predictions about how actuators will move under illumination. It is also possible that the mechanical properties of the polymerised IPL-780 change if it is written in different ways. So we designed, made and tested structures to determine the mechanical properties of polymerised IPL-780.

3.1 Stress and strain

All of the structures made using the Nanoscribe are of the order of 100nm in size or larger, and atoms are of the order 1 angstrom in size, so the structures can be understood using continuum mechanics. Continuum mechanics characterises structures in terms of the relationship between stress and strain. The strain is a description of how the material is changed by the imposition of applied forces from its state when it is not subject to any such forces. The stress is the distribution of forces induced in the object by the applied force.

Consider an element of the material in the object under consideration that is at a point $\mathbf{x}$ when no force is applied to the object and moves to a point $\mathbf{x}' = \mathbf{x} + \mathbf{u}$ when a force is applied. The strain can be described by a tensor γ_{ij}, which can be derived following [78, Chapter I, Section 1]:

$$\gamma_{ik} = \frac{1}{2}\left(\frac{\partial u_i}{\partial x_k} + \frac{\partial u_k}{\partial x_i} + \frac{\partial u_m}{\partial x_k}\frac{\partial u_m}{\partial x_i}\right). \tag{3.1}$$

When a force is applied to a material, it gives rise to forces inside the material. In what follows it is assumed that the material can be treated as a collection of volume elements. For an illustration of a volume element, see Figure 3.1.

We will assume that each element only affects its neighbours. This need not be true in general, but the forces between the molecules are short range compared to the size of the structures under consideration so in this situation the assumption is not problematic. The force density $\mathbf{f}$ on a small area δA of the element is given by

$$f_i = \sigma_{ij} n_j \delta A, \tag{3.2}$$

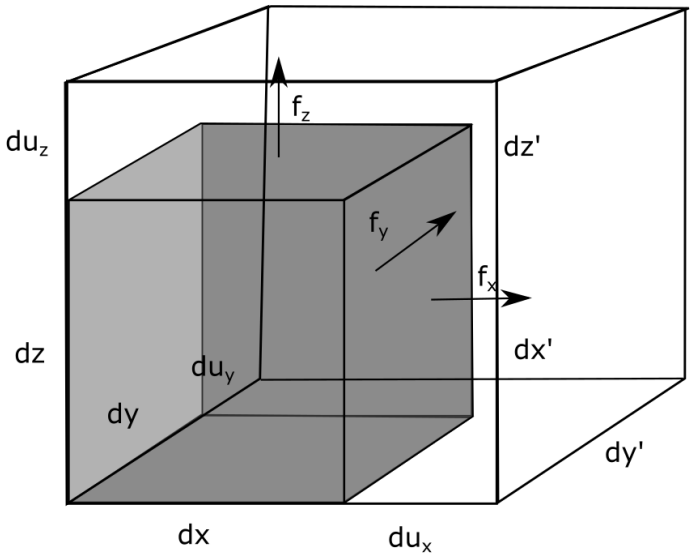

Figure 3.1: A volume element and the strain produced on that element by forces exerted by neighbours.

where $\mathbf{n}$ is a vector normal to the surface and σ is the stress tensor.

The equation of motion of the strain is given by the equation described in [79, Section 2.1]:

$$\rho \frac{\partial^2 u_j}{\partial t^2} = \frac{\partial \sigma_{ij}}{\partial x_i} + b_j, \tag{3.3}$$

where ρ is the density, $\mathbf{b}$ is the force acting on the material and

$$f_i = \frac{\partial \sigma_{ij}}{\partial x_j}. \tag{3.4}$$

The stress tensor describes the forces acting within the material and the strain tensor describe the deformation of the material from its equilibrium state without forces. If the forces and deformations are not too large, then the relationship between them is linear. Assuming that the relationship is linear, it can be represented by an elasticity tensor $\mathbf{E}$ such that $\sigma_{ij} = E_{ijkl}\gamma_{kl}$. The compliance tensor, $\mathbf{C}$ gives the stress as a function of the strain $\gamma_{ij} = C_{ijkl}\sigma_{kl}$.

The Nanoscribe polymers should have polymer chains running in multiple different directions since there is nothing to make all the chains line up. As such, any difference in stresses and strains that might occur if all the polymer molecules lined up should not occur in the material made by the Nanoscribe. To a good approximation, the properties of the Nanoscribe material should be isotropic and we will assume this is the case. For an isotropic material, we have

$$\begin{aligned} \gamma_{ik} &= \frac{1}{E}((1+\nu)\sigma_{ik} - \nu\sigma_{ll}\delta_{ik}), \\ \sigma_{ik} &= \frac{E}{1+\nu}\left(\gamma_{ik} + \frac{\nu}{1-2\nu}\gamma_{ll}\delta_{ik}\right), \end{aligned} \tag{3.5}$$

where E, ν are Young's modulus and Poisson's ratio, respectively.

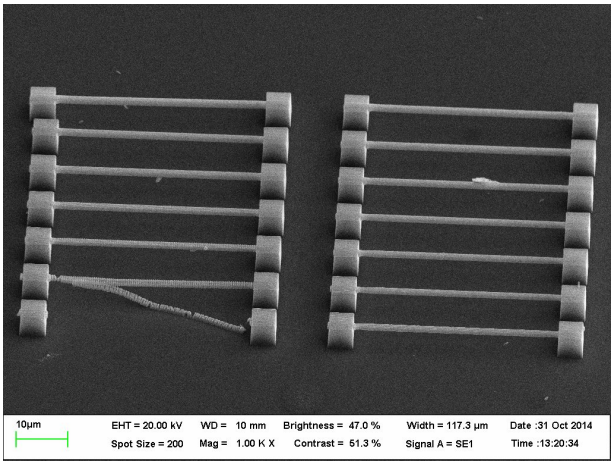

Figure 3.2: SEM image of beams designed and made by the author for mechanical testing.

3.2 Equation for static displacement of a beam

The technique used to measure the mechanical properties of the polymer was to make a beam mounted on two blocks, subject the beam to a known force at different points along the beam and then use this to find the Young's modulus. This technique has been used to investigate the mechanical properties of MEMS materials [80, 81]. The Nanoscribe can be used to manufacture a structure provided that it is attached to the substrate and would stand up under its weight, so manufacturing supported beams was possible. The controlled force could be applied using a profiler, as described below.

Test structures were fabricated to test the mechanical properties of the material made by the Nanoscribe. Each structure consisted of two identical cubes of side three microns, placed seven microns apart, with a beam running across one cube, across the gap between the cubes, and then across the other cube, as illustrated in Figure 3.2. Each beam was made by drawing lines perpendicular to the substrate equidistant from one another in the x and y directions.

A KLA Tencor profiler was used to subject these beams to a controlled force. This method of measuring the mechanical properties of microstructures has been used to measure the Young's modulus of materials used in MEMS [80, 81]. The profiler consists of a stylus two microns in diameter controlled by a piezo-electric actuator, which exerts a controlled force on the surface on which the stylus is pressing. The stylus is moved at a controlled speed along a line and its height relative to its starting point is recorded at a set of equally spaced sample points.

To find the mechanical properties of the Nanoscribe polymer it is necessary to work out the displacement of the beam if a specific force is exerted at a specific point on the beam. Consider a coordinate system in which the x-axis is parallel to the axis of the beam when it is not subject to a force. The beam is bent in the z, x-plane so that its transverse displacement as a function of x is $v(x)$. The forces within the beam are caused either by body forces in the beam or by forces applied externally by the probe, so the boundary conditions on the surfaces of the beam are $\sigma_{ik} n_k = 0$. The normal vector at the $+z, -z$ and $+y, -y$ faces point in the y and z directions respectively so $\sigma_{zz} = \sigma_{yy} = \sigma_{yz} = \sigma_{xz} = \sigma_{xy} = 0$. Since the beam is thin in the z and y directions, stress cannot build up in the beam in those directions and those expressions hold in the beam's bulk as well. So only σ_{xx} is non-zero, which means that the beam undergoes a simple extension or compression along the x axis. If the material of the beam is elastic and has Young's modulus E, it can be shown that the stress is given by [78, Chapter II,

Section 17]:

$$\sigma_{xx} = -\frac{Ez}{R}. \tag{3.6}$$

To make predictions an equation for the displacment $v(x)$ of the beam is needed. If we assume that $(dv/dx) << 1$ it can be shown that [82, Sections 5.2 and 5.3] and [83, Section 9.3]:

$$\frac{d^2v}{dx^2} = -\frac{M}{EI}, \tag{3.7}$$

where I is the second moment of the area about the z axis:

$$I = \int_A z^2 dA. \tag{3.8}$$

The moment of the area of a rectangular beam of width d and height h is given by

$$I = \int_{-h/2}^{h/2} \int_{-d/2}^{d/2} z^2 dy dz = \frac{dh^3}{12}. \tag{3.9}$$

Substituting this equation into (3.7) results in the equation:

$$\frac{d^2v}{dx^2} = \frac{12M}{Edh^3}. \tag{3.10}$$

3.3 Solution for static displacement of a cantilever

The test structure is a beam supported at both ends. But it is easier to explain the displacement of a beam supported at both ends by discussing the displacement of a cantilever first, and this provides an opportunity to explain why a cantilever was not used. The treatment of the displacement of the cantilever in this section is adapted from [84, Section 6.2.2].

When a force is exerted on the cantilever the support block may change shape too, and this could invalidate the model of the beam as a cantilever. The beams made using the Nanoscribe are embedded in the blocks below them. The extent to which a block would bend is inversely proportional to the moment of the block's area and so is inversely proportional to its horizontal thickness and the cube of its vertical thickness, as seen in equation (3.10). For some of the blocks and beams, the block is approximately five times larger than the beam in the y and z directions. For such blocks, we can expect the bending of the supporting block to be approximately 625 times smaller than the bending of the beam, so the bending will produce an error of less than 1%, which is an order of magnitude smaller than many of the other errors involved, and will be neglected. Some of the blocks are only about 2.5 times larger than the beams, and so we should not expect that the bending of the blocks will be negligible.

Suppose that a force F_0 is applied at a point x_0 away from the end of the cantilever that is not fixed, as illustrated in Figure 3.3.

If the beam is assumed to be fixed at the supported end with $v(0) = 0$ and $dv/dx(0) = 0$ and the derivative is continuous at x_0 $dv/dx(x_0^+) = dv/dx(x_0^-)$, then it can be shown that the complete solution for the cantilever is given by

$$v(x) = \frac{F_0}{6EI} \begin{cases} (3x_0x^2 - x^3) & \text{if } 0 < x \leq x_0, \\ (3x_0^2x - x_0^3) & \text{if } x > x_0. \end{cases}$$

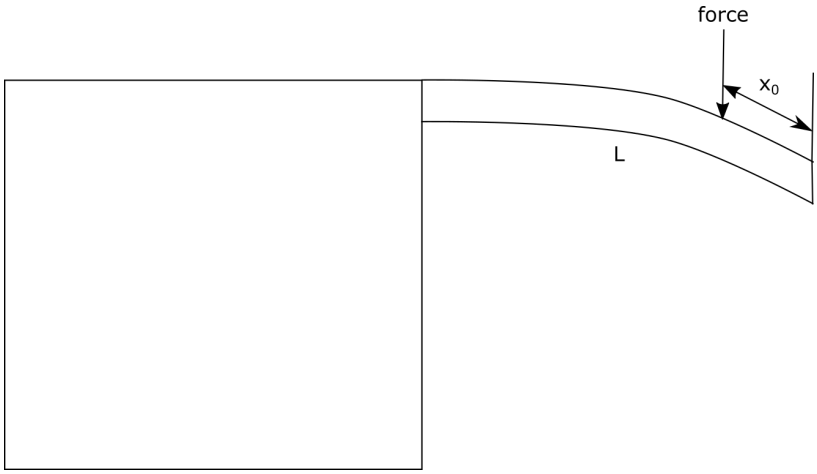

Figure 3.3: A cantilever subjected to a force.

The profiler will detect the displacement at the point where the force is exerted. So substituting the moment of the area of a block gives a measured displacement of

$$v_m(x_0) = -\frac{4F_0x_0^3}{Ewd^3}. \tag{3.11}$$

The force exerted by the profiler is 9.8μN. The Young's modulus for similar materials like PMMA is of the order $1.8 - 3.1$GPa and the the block has width and height five microns. It would be useful for the block to be significantly longer than its width so that there is a region long enough to give many measurements for the displacement to be fitted as a function of the distance from the support. So it should be possible to have a reasonable displacement of less than 7 microns if the force is exerted at a distance of ten microns along the block. The calculated displacement at ten microns along the block for a Young's modulus of 1GPa is 39 microns. The Young's modulus would have to be about 5.6 GPa, almost double the Young's modulus for PMMA, for the displacement to drop below 7 microns. So this geometry is not suitable for testing the Young's modulus of the polymer.

Making thicker beams might allow testing of cantilevers. However, a thicker beam would require a larger support. Making solid structures as large as 16 microns creates problems with the writing process as explained in the next chapter. So the beams could only be scaled in size by less than a factor of two. As such, the displacement of the cantilever beam would be more than five microns even for structures too large to be written properly. So cantilevers cannot be used as test structures.

3.4 Solution for static displacement of a beam with two supports

The treatment of the displacement of the beam supported at two ends in this section is adapted from [84, Section 6.8.1]. A beam of length L supported on two blocks can be modelled in terms of a beam with $v = 0, dv/dx = 0$ at both ends. A reaction force F_R and a reaction moment M_R are required to hold the beam and impose flatness at the $x = L$ end of the beam. The displacements as a result of F_0, F_R, M_R are written as $v_0(x), v_{FR}(x), v_{MR}(x)$ and the total solution is the sum of those displacements:

$$v(x) = v_0(x) + v_{FR}(x) + v_{MR}(x). \tag{3.12}$$

The equation for the displacement of a cantilever can be applied to obtain expressions for $v_0(x), v_{FR}(x), v_{MR}(x)$ because the beam is effectively two cantilevers stuck together at the point where the force is applied. Imposing boundary conditions $v = 0, dv/dx = 0$ on those equations at both ends of the beam and continuity of v and dv/dx at the point where the force is applied gives:

$$v(x) = \frac{F_0(3L - 2x_0)x_0^2}{6EIL^3}(3Lx^2 - x^3) + \frac{F_0(L - x_0)x_0^2}{2EIL^2}x^2 \qquad (3.13)$$
$$+\frac{F_0}{6EI}\begin{cases} (3x_0x^2 - x^3) & \text{if } 0 < x \leq x_0, \\ (3x_0^2x - x_0^3) & \text{if } x_0 < x \leq L. \end{cases}$$

3.5 Measurement of Young's Modulus

The quantity measured by the profiler is the displacement at x_0, which will be written as:

$$v_0(x_0) = \frac{F_0(L - x_0)^3x_0^3}{3L^3EI}. \qquad (3.14)$$

The displacement measured by the profiler at $L/2$ is given by:

$$v_0(L/2) = \frac{F_0L^3}{192EI}. \qquad (3.15)$$

Substituting the expression for the moment of the area of a rectangular block into the two equations above gives

$$v_0(x_0) = \frac{12F_0(L - x_0)^3x_0^3}{3L^3Ewh^3},$$
$$v_0(L/2) = \frac{F_0L^3}{16Ewh^3}. \qquad (3.16)$$

A typical scan, such as figure 3.4, starts on the coverslip that the sample is resting on. The equation for $v_f(x_0)$ is only expected to apply from the point where the beam meets the block call this $x_0 = x_1$, so the equation for $v_f(x_0)$ should be changed:

$$v_f(x_0) = a(L - (x_0 - x_1))^3(x_0 - x_1)^3 + h_0, \qquad (3.17)$$

where a, x_1, h_0 are constants for any particular data set. The displacement from the top of the structure at the centre of the beam is given in terms of the fitted parameters is

$$v_c = \frac{aL^6}{64}. \qquad (3.18)$$

In terms of fitted or measured quantities,the Young's modulus is given by:

$$E = \frac{F_0L^3}{16v_cwh^3} = \frac{4F_0}{aL^3wh^3}. \qquad (3.19)$$

Each beam was scanned several times. In a typical scan of the beam, the stylus would start on the coverslip, then the recorded height would increase until it reached the top of a block. The stylus would then scan along the beam and the second block, and finally drop in height until it ended up back on the coverslip, as illustrated in 3.4. Each beam was scanned from left to right and right to left to left to check whether the scans distorted the structure. A forward and backward scan of the same structure typically looked similar and gave similar figures for fitted quantities and quantities derived from the fits, so it does not appear that the scans damaged the structures.

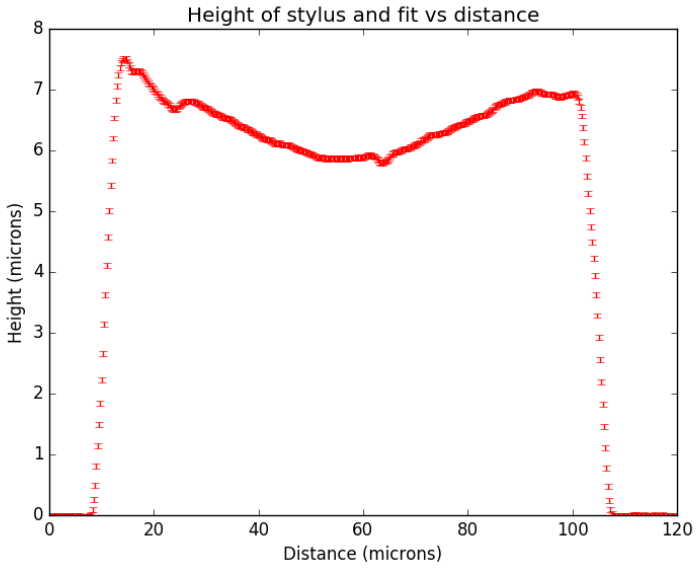

Figure 3.4: Data from a typical scan of a beam mounted on two blocks.

In order to get a measurement of Young's modulus, it is necessary to know d and h as well. Using a scanning electron microscope, the width of the beam was measured as viewed from above and with the sample tilted at an angle of 45°. The width of a whole rectangular beam as seen at an angle θ is given by

$$w(\theta) = h\sin\theta + d\cos\theta, \tag{3.20}$$

as can be seen from Figure 3.5. The measurement from above gives d and h can be obtained from $w(\theta)$ by the equation

$$h = \frac{w(\theta) - d\cos\theta}{\sin\theta}. \tag{3.21}$$

The errors in the measurement of w and h are $\pm 40nm$ owing to some non-uniformity in the thickness of the beam. The error in h as a result of propagating those errors is

$$\delta h = \sqrt{\frac{\delta w^2}{\sin^2\theta} + \frac{\delta d^2\cos^2\theta}{\sin^2\theta}}, \tag{3.22}$$

where δd is the measurement error in d, which gives $\delta h = 69nm$ when $\theta = 45°$.

SEM images of some of the beams show a clear transition between the top and the side of the beam, such as Figure 3.6. Other images do not show such a transition: an example is shown in Figure 3.7. Where the side of the beam can be distinguished from the top, the height h as a function of the height h_θ at angle θ is given by

$$h = \frac{h_\theta}{\sin\theta}, \tag{3.23}$$

The error in the height δh as a function of the error in the measurement of the side of the beam at an angle δh_θ is

$$\delta h = \frac{\delta h_\theta}{\sin\theta}, \tag{3.24}$$

which gives $\delta h = 57nm$ where $\delta h_\theta = 40nm$.

In the first tested batch of beams, which were designed to have a depth and height of two microns, all of the transitions were unclear and all of the depths were calculated using the formula above. A second batch of beams were designed to have a depth and

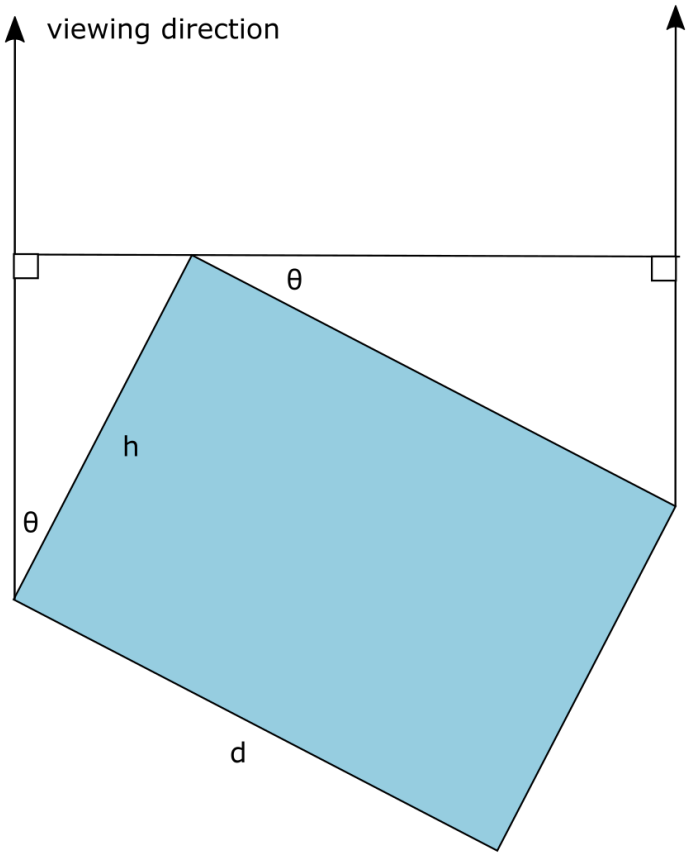

Figure 3.5: The beam tilted at an angle, with the arrow pointing in the direction from which the beam is viewed in the SEM.

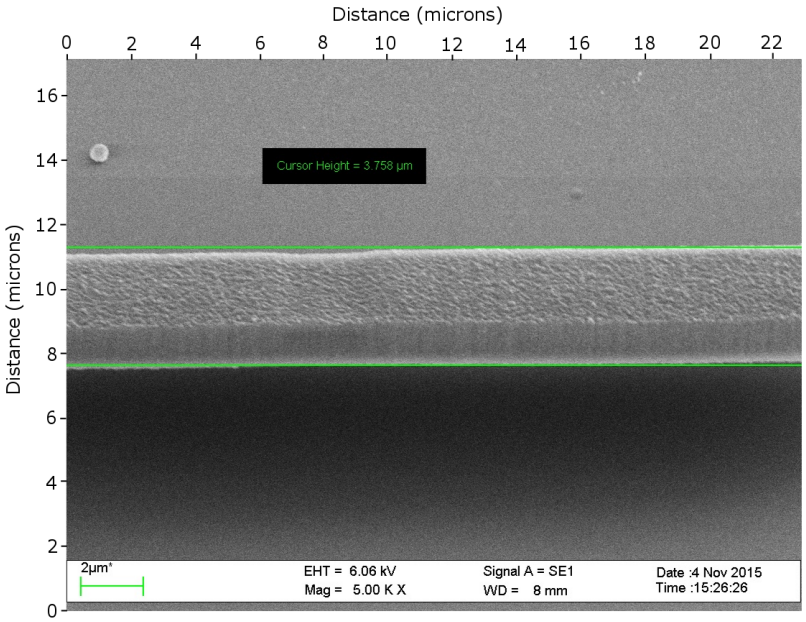

Figure 3.6: Image of a beam at an angle with a clear transition between the side of the beam and the top of the beam. The green lines mark the top and bottom of the beam. The line in the middle of the green lines is the transition between the top and the side. The figures in the black rectangle are the SEM's measurement of the distance between the features on the picture bounded by the green lines.

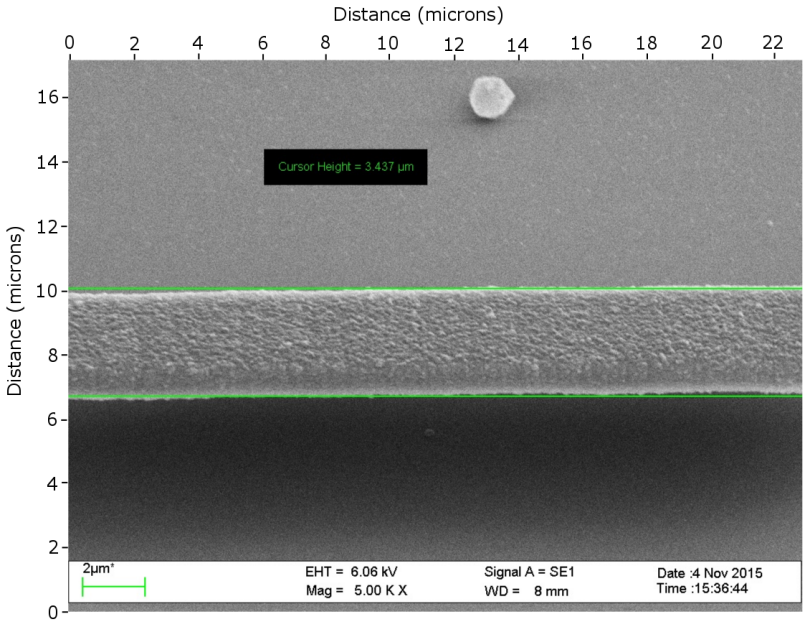

Figure 3.7: Image of a beam at an angle without a clear transition between the side of the beam and the top of the beam. The green lines mark the top and bottom of the beam. There is no line in the middle of the green lines to indicate the transition between the top and the side. The figures in the black rectangle are the SEM's measurement of the distance between the features on the picture bounded by the green lines.

height of four microns. Some of those beams showed clear transitions from the side to the top of the beam. The measured and calculated dimensions of these batches are given in separate tables 3.1 and 3.2 below.

The errors in E are given by

$$\delta E = \frac{1}{aL^3wh^3}\sqrt{16\delta F_0^2 + \frac{16F_0^2\delta a^2}{a^2} + \frac{16F_0^2\delta w^2}{w^2} + \frac{144F_0^2\delta h^2}{h^2} + \frac{144F_0^2\delta L^2}{L^2}}. \qquad (3.25)$$

The errors in the force exerted by the profiler are $\pm 10\%$ of the force according to a private communication with the manufacturer. The equation (3.17) was fitted using Scipy [75]. A couple of samples of fitted curves are given below in Figures 3.8 and 3.9. The fitted parameter a and the calculated Young's moduli are shown in an appendix in Tables B.1–B.3.

The estimated Young's moduli differ by as much as a factor of about 2.6 from one another from the lowest to the highest values: the minimum value is 4.7 GPa and the maximum is 12 GPa. In a private communication, Nanoscribe informed me that they have measured the Young's modulus of IP-L 780 using a nano indentation and found a value of 4GPa, which is smaller than the smallest value estimated above. Some variation in Young's modulus might be expected as a result of different degree of polymerisation in structures written with different speeds and powers. If the beams had internal structural differences from one another, that could in principle produce differences in the measured Young's moduli, but they are all solid. It is possible that they are not all rectangular in cross-section. Beams with a clear transition may be rectangular, but those with a clear transition may have rounded corners. If a beam has rounded corners, then the argument given above for how to do the calculation will underestimate the vertical thickness of the beam. Since the expression for the Young's modulus in terms of the experimental data is dependent on $1/h^3$ this could change the calculated Young's modulus.

Sample	Top (μm)	Whole Beam (μm)	Calculated side (μm)
1	2.1	2.4	1.3
2	2.1	2.3	1.2
3	2.1	2.2	1.1
4	2.1	1.9	0.6
5	2.1	1.8	0.5
10	2.1	2.4	1.2
11	2.2	2.5	1.3
12	2.1	2.4	1.3
13	2.1	2.1	0.8
14	2.1	2.0	0.7
16	2.1	1.9	0.6
17	2.1	1.9	0.6
18	2.1	1.8	0.5
19	2.2	2.6	1.5
20	2.3	2.7	1.5
21	2.2	2.5	1.4
22	2.1	2.1	0.9
23	2.1	2.1	0.8
24	2.1	2.0	0.8
25	2.1	2.0	0.8
26	2.1	2.0	0.7
27	2.1	1.9	0.6

Table 3.1: Measured and derived sizes of samples in the second batch of test structures. "Top" is the width of the top of the beam. "Angle whole" is the width of the whole beam measured at an angle. "Calculated side" is the size of the side as calculated using 3.22.

Sample	Top (μm)	Whole beam (μm)	Measured side (μm)	Calculated side (μm)	Side from measurement (μm)
1	3.5	3.8	1.4	1.8	2.0
2	3.5	3.6	1.3	1.6	1.9
3	3.5	3.4	0.9	1.4	1.3
4	3.4	3.2	0.8	1.2	1.1
5	3.7	4.5	2.2	2.7	3.1
6	3.6	4.3	1.9	2.5	2.7

Table 3.2: Measured and derived sizes of samples in the second batch of test structures. "Top" is the width of the top of the beam. "Whole beam" is the width of the whole beam measured at an angle."Measured side" is the side as measured on an SEM image. "Calculated side" is the size of the side as calculated using 3.22. "Side from measurement" is the size of the side as calculated using 3.23.

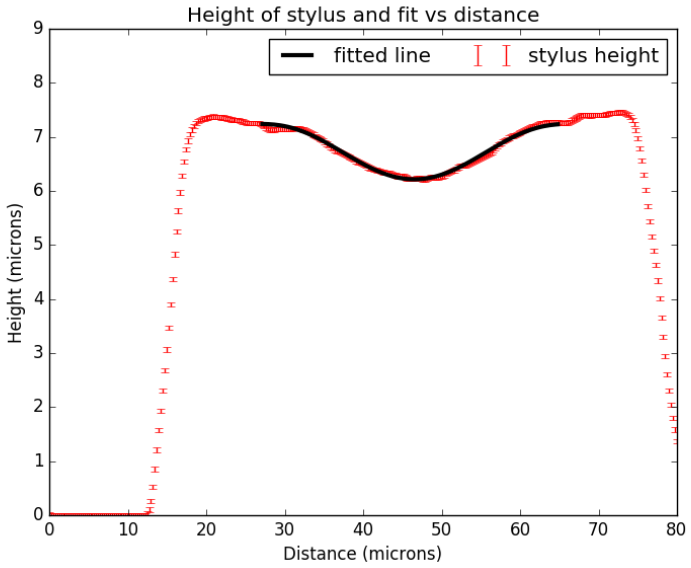

Figure 3.8: Experimental data from a scanned beam with error bars in red, with overlaid fitted line in black.

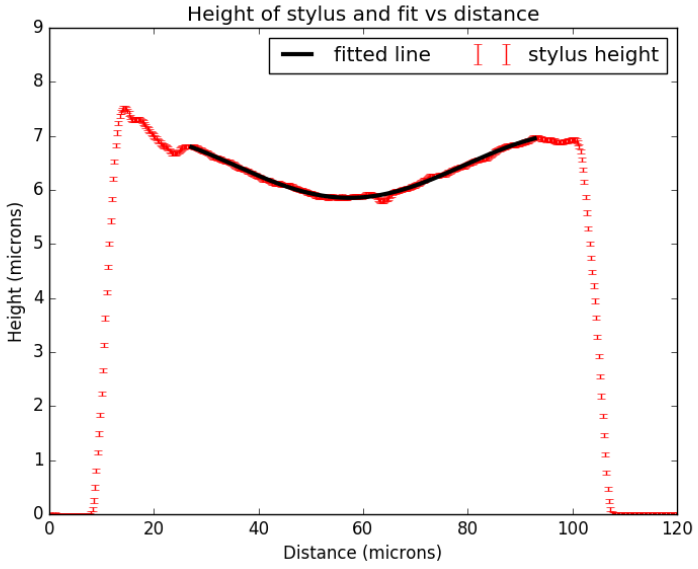

Figure 3.9: Experimental data from a scanned beam with error bars in red, with overlaid fitted line in black.

Another potential problem is that the stylus may not run down the centre of the beam. If this happens, then the stylus may exert a torque on the beam that causes it to twist. If the warping of the beam can be described by a rotation of its cross-section, and a small warping of the cross-section that is the same for all cross-sections, then an equation for the warping of a rectangular beam can be derived [85, Sections 90 and 95]. The assumption that the warping is the same for all cross-sections is probably not true for the edges of the beam that are on the blocks. Nor will it necessarily be true for the section of the beam that the stylus is on. There will be more warping at the points the stylus is in contact with, and so the warping on the stylus section of the beam will differ from the warping elsewhere. The section on which the stylus rests is relatively short compared to the length of the whole beam. So the predicted angle should be accurate near the centre of the beam. The maximum angle through which the beam will turn will be

$$\Theta = \frac{FL}{2Gw^2h\beta(w/h)}, \tag{3.26}$$
$$\beta(w/h) = \frac{1}{3}\left(1 - \frac{192h}{\pi^5 w}\sum_{n=1,3,5\ldots}^{\infty}\frac{1}{n^5}\tanh\frac{n\pi h}{2w}\right).$$

The function $\beta(w/h)$ varies between 0.1406 and 0.333: see the table on [85, p. 277]. For $w/h = 1$, which is approximately true for these beams, $\beta(w/h) = 0.1406$. The error produced in the result of the measurement by the twisting is

$$\delta v_\Theta = \frac{w\tan\Theta}{2}. \tag{3.27}$$

For the two micron beams, the length of the beam is designed to be 40 microns. For the four micron beams the length is designed to be 70 microns. In addition, the two micron beams were only subjected to a force of 9.8 μN while the four micron beams were subjected to a force of 49 μN. So the set of (F, L, w, h) for which the error is at a maximum is either $\delta v_\Theta(9.8\mu N, 40\mu m, 2\mu m, 2\mu m) = 0.064\mu m$ or $\delta v_\Theta(49\mu N, 70\mu m, 4\mu m, 4\mu m) = 0.088\mu m$. The displacements of the beam are often only of the order 0.1 microns, as illustrated in Figures 3.8 and 3.9.

Another problem arises from the boundary conditions. The equation given above for the variation of the depth with distance assumes that the ends of the beam are fixed. If the beam is small enough relative to the block, this may be true because the block will deform by a small amount compared to the beam. However, the beam is not small relative to the block in all cases. This complication, together with those listed above, make a different approach necessary.

3.6 Comsol simulations of a beam mounted on two blocks

One way to solve the problem is to simulate the deformation of beams mounted on a block in Comsol assuming that the Young's modulus is 4GPa. The simulation was performed using the "Structural Mechanics: Static Linear Analysis" module. The model consists of two blocks of side seven microns, whose bases are kept fixed, a distance d apart with beams of height h and width w attached, as depicted in Figure 3.10.

In any single run, the simulation works out the equilibrium displacement of one of the upper edges of the beam when some force F is applied by exerting uniform pressure on a region of the beam two microns in length. To find the displacement of the stylus as it moves along the beam, this calculation is repeated with the patch on which the force is exerted moving along the beam. This gives a series of curves similar to those plotted in Figure 3.11.

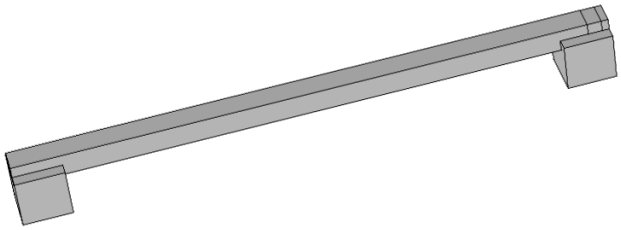

Figure 3.10: A diagram of the beam simulated in Comsol.

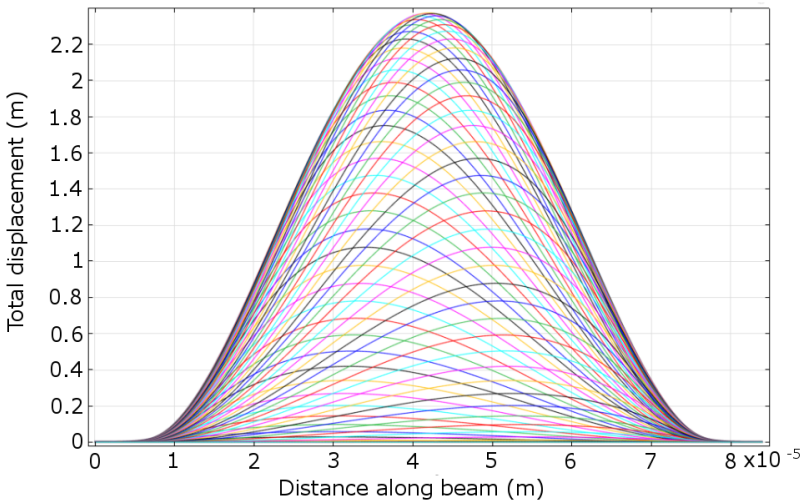

Figure 3.11: A series of curves produced by Comsol for the displacement of a beam with the stylus at various positions along the beam. Different colours indicate different positions for the stylus along the beam. The beam has width of 3.5 microns and depth 1.9 microns and the force applied is 9.8 μN.

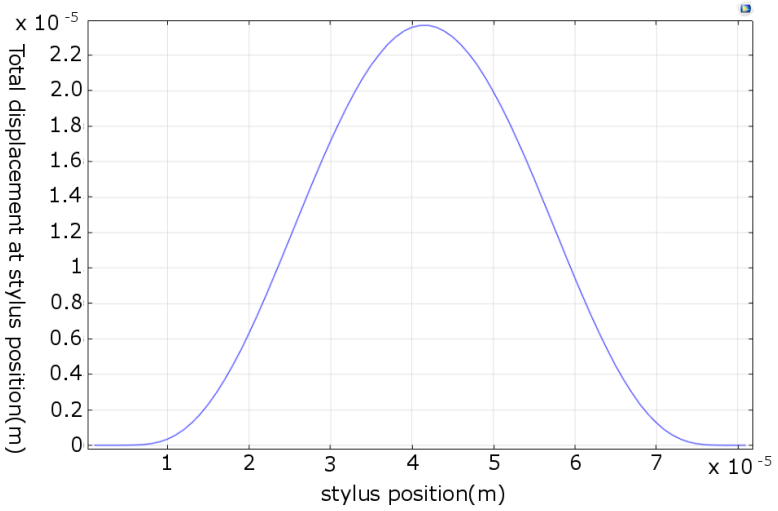

Figure 3.12: A curve produced by Comsol for the displacement of the beam at the stylus position for a range of geometries. The beam has width of 3.5 microns and depth 1.9 microns and the force applied is 9.8 μN.

Force (μN)	Top (μm)	Side (μm)	d_{meas} (μm)	d_{sim} (μm)
9.8	3.5	2.1	1.0–1.1	2.4
19.6	3.5	2.1	1.7–2.0	4.7–4.8
49	3.5	2.1	3.3–3.7	12
9.8	3.5	3.2	0.6	0.5
9.8	3.5	2.8	1.4–2.0	2.4

Table 3.3: Simulated and measured displacements for various beams.

To find the position of the stylus, the displacement of a point on the edge of the stylus patch is plotted: the results are plotted in Figure 3.12.

To account for the possibility of the stylus not running down the centre of the beam, two simulations were done for each beam. In one of the simulations, the region to which the force was applied crossed the entire beam, representing the case in which the stylus is in the centre of the beam. In the other, the region to which pressure is applied is one quarter of the width of the beam.

The experimental results then have to be compared to the results of the simulations. The difference between the maximum and minimum height of the stylus in the experimental data is calculated, and compared to the simulated displacement. The comparison was only carried out for cases in which the side of the beam could be clearly distinguished from the top of the beam and measured.

Table 3.3 gives the simulated and measured displacements d_{sim} and d_{meas} respectively. In some cases ranges are given where more than one result was available for a sample or simulation. This covers the case in which running the stylus on the edge of the beam changed the result when rounded to one tenth of a micron. The results for the sample with side 2.1 microns do not seem consistent with the results of the simulations, except for the last result which is consistent with the beam being pushed into the coverslip. For the other samples, the results seem compatible with the simulation. The simulation does not account for the results of the experiments.

3.7 Discussion

The data and calculations explained above are not consistent with a figure of 4GPa for the Young's modulus of IP-L 780. In this section, we try to assess if the figures given above could be accurate or if there is another explanation of the results.

3.7.1 Recalculating the height and non-uniformity

The calculations of the Young's modulus could be wrong because the beams are not in fact rectangular. The ends of the beam bulge out slightly because the voxels are of finite width. As a result, the width of the beam when seen at an angle θ is $d - 2w_v$ where w_v is the width of a voxel. As a result, (3.21) changes to

$$h_{new} = \frac{w(\theta) + (2w_v - d)\cos\theta}{\sin\theta}, \tag{3.28}$$

which adds $2w_v$ to the height. The voxel width data from the chapter on the resolution of the Nanoscribe can be used together with the data from this chapter to calculate h_{new} for each sample.

The Young's modulus E_{new} for this new estimate of the height of the beam can be calculated using

$$E_{new} = \left(\frac{h}{h_{new}}\right)^3 E. \tag{3.29}$$

Calculating E_{new} using these equations gives values that are of the order 10GPa and mostly around 40-80GPa. This estimate is not of the right order of magnitude for a polymer, so this estimate of the height is mistaken.

There is a problem with any explanation of the result in terms of height. The Young's modulus estimates for different scans of the same sample sometimes differ by a factor of two or more: the lowest figure for sample 2 is 4.7GPa and the highest is 12GPa. A mistaken estimate of the height of a beam could not produce such a discrepancy since it would multiply the Young's modulus for all scans of the same sample by the same factor.

Another problem is that any particular beam is not perfectly uniform in shape. A beam also may not be perfectly uniform in their Young's modulus or density. Different places in the beam may be exposed differently since parts of the beam written earlier may have some effect on the distribution of intensity. Slightly different intensity could result in slightly different material properties by affecting the degree to which the resist polymerises. One potential line of research would involve considering the effects of that non-uniformity using the theory for non-uniform beams [86–88].

3.7.2 Non-linear effects

For sufficiently small stresses a polymer will undergo a linear change in strain as the stress increases. For larger stresses, the stress required to produce a given strain increases more than linearly. This strain hardening is attributed to the stress forcing polymer molecules to align more closely with one another [89]. Some of the samples broke on their first scan. Some of the other samples might have been similar enough to the broken samples to undergo non-linear effects without breaking, so non-linear effects should be considered as an explanation. For most of the samples, measurements are only available for two values of the force. As such, the stress cannot be fitted as a function of force.

For a large enough tensile stress, a polymer may snap: the value of the tensile stress is called the tensile strength of the polymer. The distance from the bottom of the beam to the substrate was around 7 microns, the depth of the beam was only around 1-2 microns and the beams were measured as pressed down by two microns at the most so the beam was not being pressed into the substrate. As such the beam was not being compressed against the substrate and most of the stress on the beam would be tensile stress rather than compressive stress. So a comparison of the stress on the beam with the tensile strength of plastics such as PMMA would test whether the IP-L 780 samples were subjected to stresses close to its tensile strength.

The tensile strength of PMMA is 72.4 MPa and the tensile strength of other similar plastics are all of the order of 10 MPa [90, Table 1.10], [89]. The forces on the beams were in the range 9.8-49 μN. The area on which the force was exerted was 2 μm $\times$ 2 μm and the cross-sectional area of the beam was of the same order of magnitude. If the beam is only about 1 μm deep, then the area is smaller and the stress increases. So the stress exerted on the beams was in the range 2.5-24.6MPa. All of the stresses in that range are somewhat less than the stress required to produce non-linear effects in PMMA. The value of 12.5MPa is similar to the values of some the other plastics in the table [90, Table 1.10]: the lowest is 9.6MPa. The range of stresses on the beams overlaps the range of stresses of some of the plastics on the table, so non-linear effects may be relevant. Further investigation would require more experiments with a wider range of forces in addition to more modelling.

Chapter 4

Optical properties of the Nanoscribe polymer

The object of the research described in this thesis was to make an optical actuator: a device that changes its shape when light of a suitable wavelength is incident on it. This device must have internal structure of the order of one wavelength in size for the wavelength of interest. According to Nanoscribe GmbH, the Nanoscribe can write devices with a minimum feature size of the order 100nm [35]. The Nanoscribe has been used to make templates for optical structures made out of other dielectrics or metal [91–98]. Two-photon polymerisation has also been used directly to make photonic crystals such as woodpiles [36–44] or 1D photonic crystals [45], arrays of standalone optical elements [99–102], microscopic machines [103, 104], aperiodic diffractive elements [105] and waveguides [106]. This chapter describes the fabrication and testing of Bragg stacks using the Nanoscribe. Bragg stacks are simpler than three-dimensional photonic crystals and so might give better information about the optical properties of the Nanoscribe polymer as a result.

Critical point drying is supposed to keep structures with microscopic features intact [72–74]. However, without a test of actual structures written by the Nanoscribe and processed by critical point drying, it is impossible to know whether the process actually works.

This chapter describes experiments undertaken to determine how to make Bragg stacks consisting of hexagonal planes of solid IP-L 780 held up by pillars at their corners. These planes are designed to be a fixed distance apart. The actual distance between the plates in a stack and their thickness will affect the transmission spectrum of the stack.

The writing process might not always produce the structure it was designed to produce. The Nanoscribe has produced structures with features of the order of 0.2 microns in depth, e.g. - the single lines written between two blocks as described in 2. But in all of those cases, a structure 0.2 microns in depth was not close to other structures that are supposed to be of the same scale. Structures that are written close enough together are no longer separated. For example, two lines written 150nm apart in a block no longer appear as distinct lines. This chapter describes what sort of writing patterns, powers and velocities of the laser focus produced Bragg stacks.

Another potential problem is that the critical point drying procedure may not preserve the internal structure of a stack. The plates in the stack may sag under their own weight so that they are not separated by the designed distance.

The development of writing patterns for making the stacks is described in the first section. The predictions that can be made using different assumptions about the internal structure of the stack are explained in the next section. Then measurements of some test structures are described and the results are interpreted.

4.1 Nanoscribe writing patterns for making stacks

The design of a stack has to take account of physical effects that might prevent the stack from being written successfully, effects that might cause the stack to be damaged or destroyed after it is written and what sort of stacks can be measured.

To test a stack it is necessary to shine light through the layers of the stack. The stack is attached to a coverslip. Removing the stack without damaging or destroying it would be difficult, so the stack was illuminated in situ. Also, it would be difficult to illuminate a stack from the side because it could only be of the order of tens of microns tall. As a result, the stacks were all written with the layers of the stack parallel to the coverslip. The layers in the stack have to be held apart from one another. Struts were constructed at the corners of the stack before the layers were written, as shown in figure 4.1.

The layers were written by writing concentric hexagons from the edge of the stack toward the centre. The outer edges of the layers would be attached to the pillars and would hold up the material further inside. This writing pattern is shown in Figure 4.2.

An attempt was made to write stacks from bottom to top, but this attempt failed, see figure 4.3. This stack was written to be 15 microns tall and to have layers that were the same in size and shape from top to bottom: hexagons 12 microns in diameter. In the image, the upper layers are not hexagonal and are smaller than the required diameter. Experiments were conducted to test what causes this problem since its recurrence would prevent successful writing of stacks. To this end, some theories about the cause of the problem were proposed and tested.

The first theory is that large enough solid structures change the distribution of light near the stack as a result of a difference in refractive index between solid and liquid IP-L 780. This theory would predict that a sufficiently large structure made of solid IP-L 780 would distort structures written near it, regardless of its shape or internal structure.

The second theory is that the structure was initially written correctly then collapsed for mechanical reasons. This theory would imply that stacks of any size would collapse when blocks were written on top of them. The theory would not predict that large blocks would be distorted.

The final theory is the distortion is caused specifically by trying to write Bragg stacks: the stacks might reflect laser light. This theory would predict that structures written on top of a sufficiently tall Bragg stack would be distorted, but those written on a tall block would not be distorted.

To test these theories, blocks were written on top of various structures, see figure 4.4. In what follows, each of the structures described is followed by the number of the column in which the structure lies. In each case, tall structures are 16 microns tall, short structures are 8 microns tall.

The results of the experiment are described in table 4.1. The table gives a description of the system in each column and whether a given theory was compatible with the experimental results. Only one of the theories considered is consistent with the results

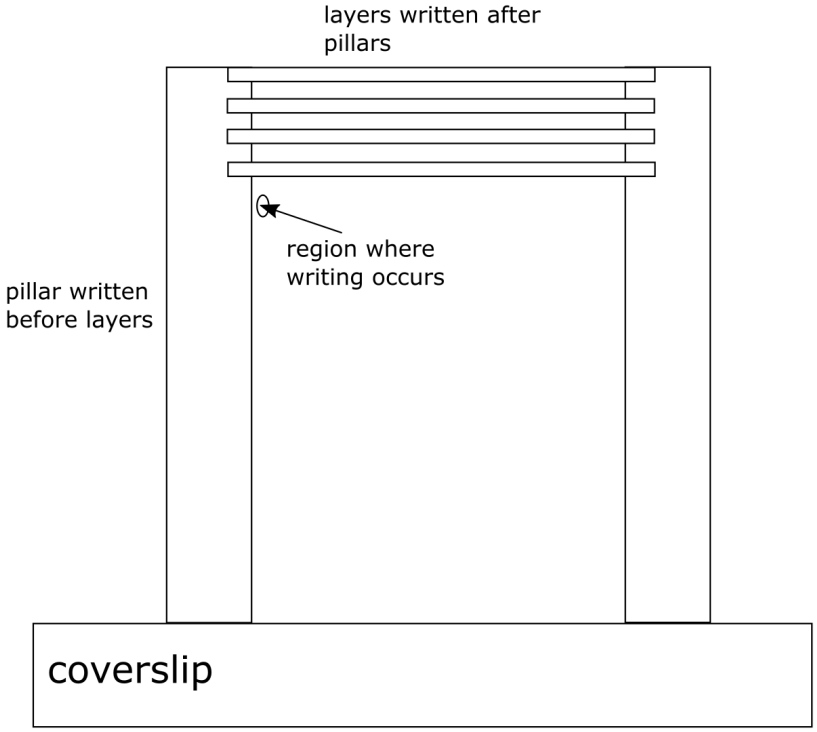

Figure 4.1: Illustration of the writing of layers in a stack.

Theory	Column 1	Column 2	Column 3	Column 4	Column 5
Description	block on tall stack	block on short stack	block on tall block	block on short block	tall block
Structural	compatible	incompatible	incompatible	incompatible	incompatible
Stack	compatible	compatible	incompatible	compatible	incompatible
Refractive index	compatible	compatible	compatible	compatible	compatible

Table 4.1: Table describing experimental results and their compatibility or lack thereof with different theories.

of all the experiments: the theory that sufficiently large pieces of solid IP-L 780 distort the laser beam during the writing process as a result of the refractive index difference between liquid and solid IP-L 780.

Another way of assessing whether a refractive index difference caused the distortion is to simulate a laser beam passing through a structure that has a small refractive index difference from a surrounding fluid. Such a simulation would require information about the refractive index of the Nanoscribe polymer. Another PhD. student Elena Markovna measured the refractive index for solid IP-L 780 was measured as 1.46 at 780nm using the M2000DI ellipsometer, which is a rotating compensator ellipsometer. See Appendix C for an explanation of ellipsometry. The refractive indices of the fluid and the structure are 1.42 and 1.46 respectively. The 1.42 value for the liquid IP-L 780 was chosen as being slightly different, although there is no particular reason to think that is the real value, other than the fact that it qualitatively explains the results above. The structure is a block 10 microns tall.

Comsol was used to model the distribution of the field relative to various structures such as a stack and a single beam made of polymer. Comsol was used because one of the systems involved was a Bragg stack. Simulating a Bragg stack involves being able to simulate interference effects in two dimensions. Before doing the simulation it was not

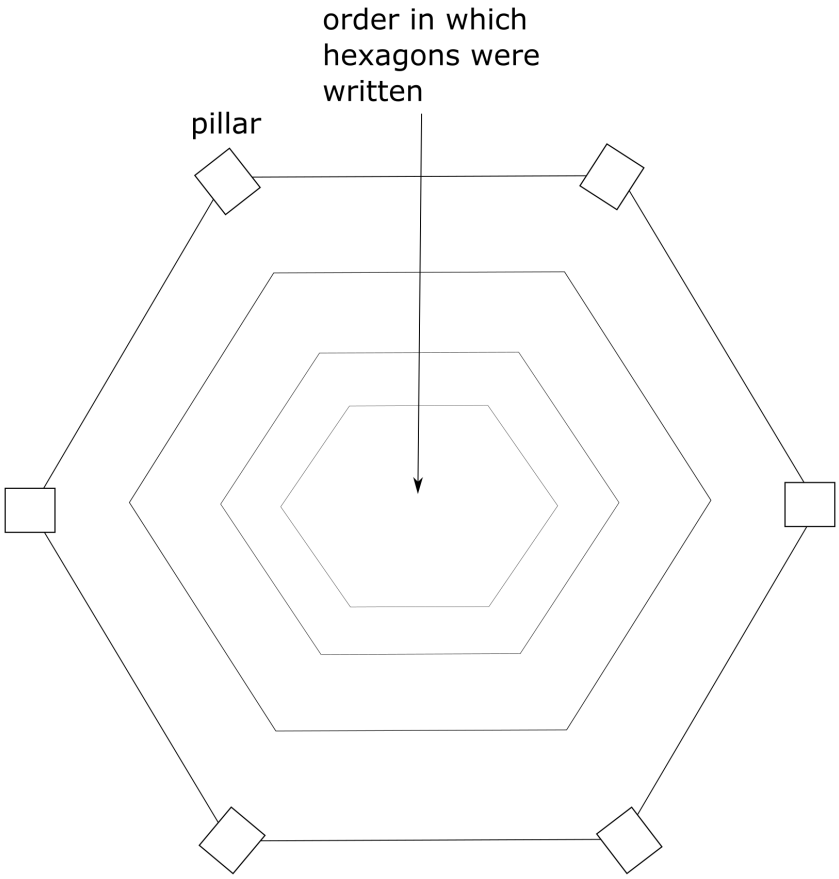

Figure 4.2: Illustration of writing of a single layer.

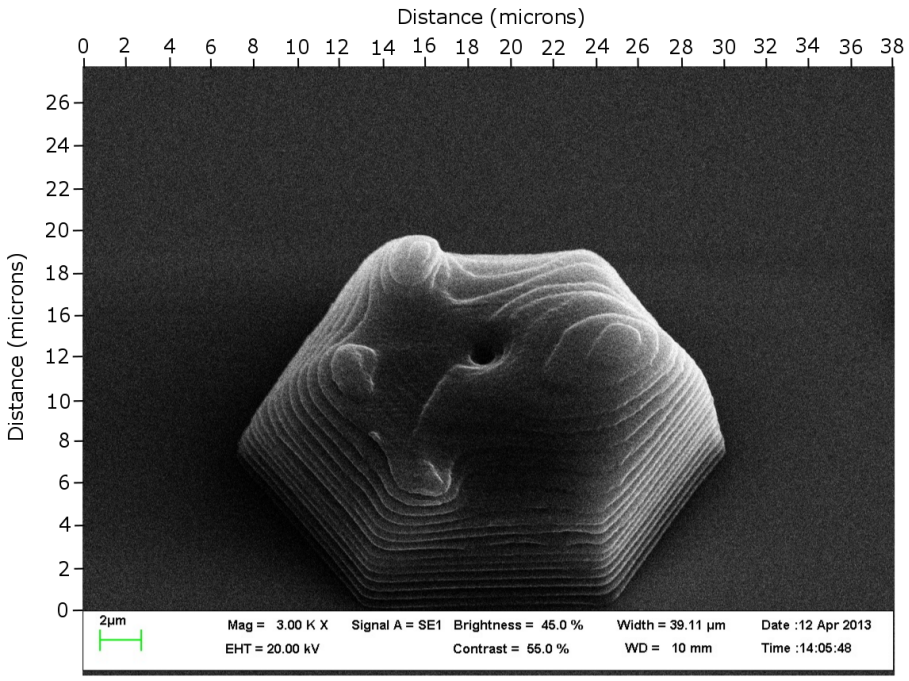

Figure 4.3: SEM image of stack written from bottom to top. The stack was designed, made and imaged by the author.

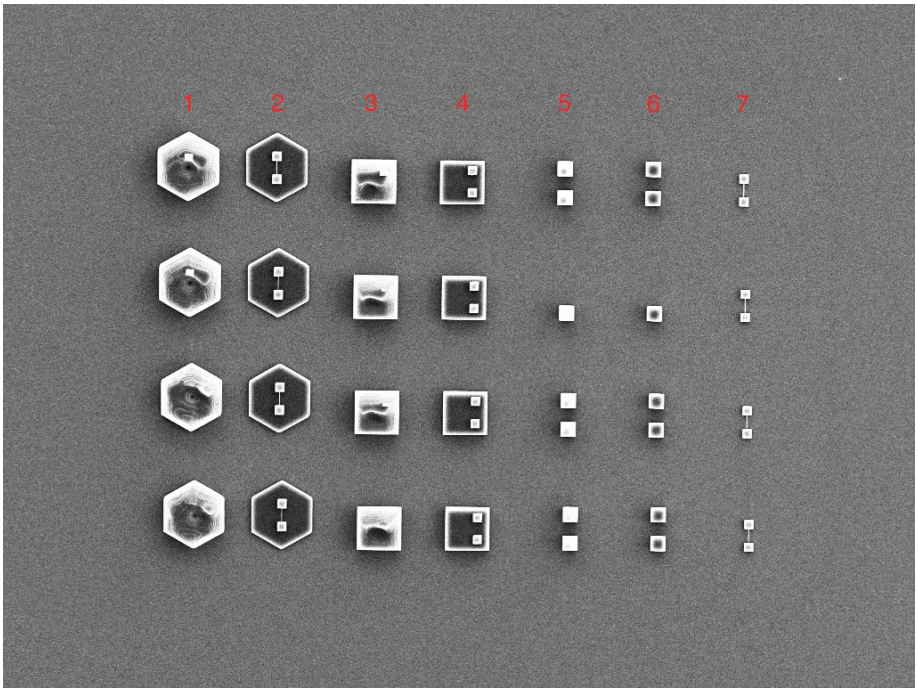

Figure 4.4: SEM image of blocks written on various structures. The structures were designed, made and imaged by the author.

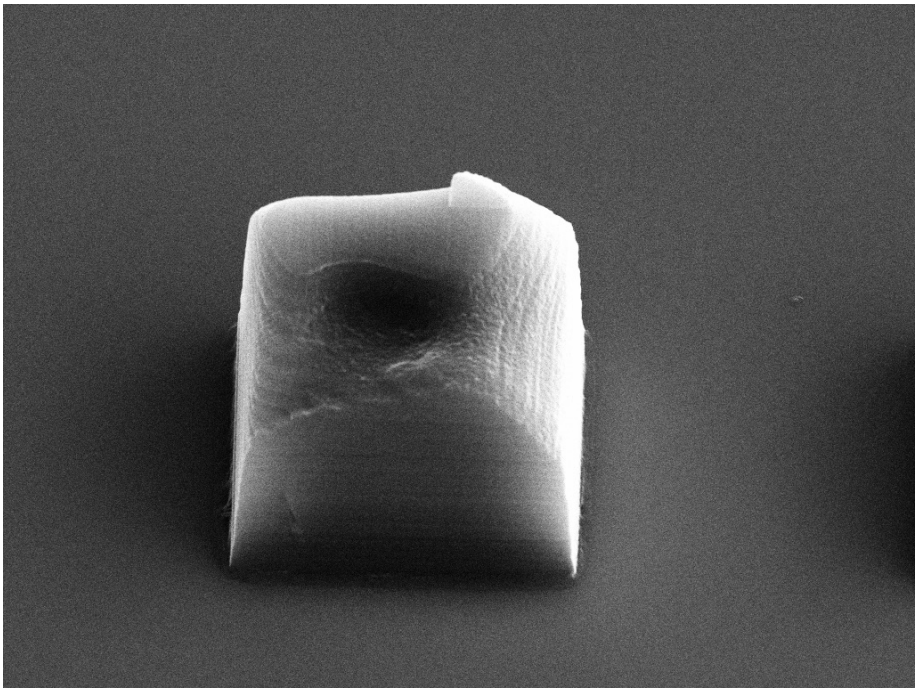

Figure 4.5: SEM image of a 16 micron tall block, showing that the top is distorted.

possible to know whether interference effects would be relevant. So it seemed reasonable to use software that was capable of simulating arbitrarily complex electromagnetic fields. This would require a method like finite difference time domain (FDTD) [107, Chapter 5] as used in MEEP [24] or the Finite Element Method [108] used by Comsol. An attempt was made to model the system as a block with refractive index 1.42 in a material of refractive index 1.46, but this produced pathological results. The laser beam was not consistent with a Gaussian beam, even when the location of the beam waist was chosen to be far from the block. This may have been a result of a problem with the boundary conditions. To solve this problem, the system was modelled as a block of refractive index 1.03 in air.

The field is a result of the beam being reflected at the boundaries between materials and suffering phase change as a result of propagation. The reflection is governed by the Fresnel coefficients, which are all of the form

$$\frac{(an_1/n_2 + b)}{(cn_1/n_2 + d)}, \tag{4.1}$$

where n_1, n_2 are the refractive indices and a, b, c, d do not depend on the refractive indices, although they do depend on the angle of incidence. So as a function of the refractive indices reflection at boundaries depends only on the ratio of the refractive indices.

The phase change will be different in media of different refractive indices. This effect can be accounted for by changing the wavelength of the field since the phase change is given by a product of the form nkd where $k = 2\pi/\lambda$ is the wavenumber, d is the distance the beam propagates, and n is the refractive index of the material. If the substitution $n \to n/n_1$ and $\lambda \to \lambda/n_1$ is applied, then the same phase change remains the same. So the wavelength of the beam was chosen to be $0.780/1.42 = 0.549$ microns rather than 0.78 microns.

Typical results of such simulations are shown in figures 4.6 and 4.7, which show a beam passing through and near a block of polymer 1 micron wide by 10 microns deep. When the beam does not pass through a block of polymer, the maximum of intensity is near the centre of the simulated area. When the beam passes through a solid block of polymer but is otherwise the same, the maximum of intensity is close to the bottom of the block. This happens because the electric field tends to concentrate its energy in high refractive index regions, as explained in [10, Chapter 2, pp. 14–16]. As a result, when a beam passes through a solid block of polymer of those dimensions the beam will not polymerise the resist near the top or centre of the block since the maximum of intensity is not located in that region.

Another simulation whose results are shown in figure 4.8 examined a beam with the same parameters incident on a stack. As noted previously, the beam would have a maximum of intensity near the centre of the simulated region if the stack was not present. But in the simulation with the stack, the maximum of intensity is confined near the bottom of the stack. So to write layers near the top of a large stack, it is necessary to write the top layers first and the lower layers later.

The effects of blocks of solid IP-L 780 can be tested further by writing specially designed stacks. The stack should have square pillars at its corners that have horizontal size larger than one micron, and it should be taller than ten microns. If the cross section of beam waist overlaps with the pillars by more than one micron when the layers are being written, then near the top of the stack the beam will be deflected near the pillars and the layers will be distorted. Specifically, regions of the layers near the pillar will not be written as designed even if they are written from the top down. The outer edge of a layer is designed to be half way through a pillar, so for larger pillars the outer edge would be poorly written farther into the middle of the stack. But if the problems with the stacks were a result of structural collapse, then thicker pillars would not cause any

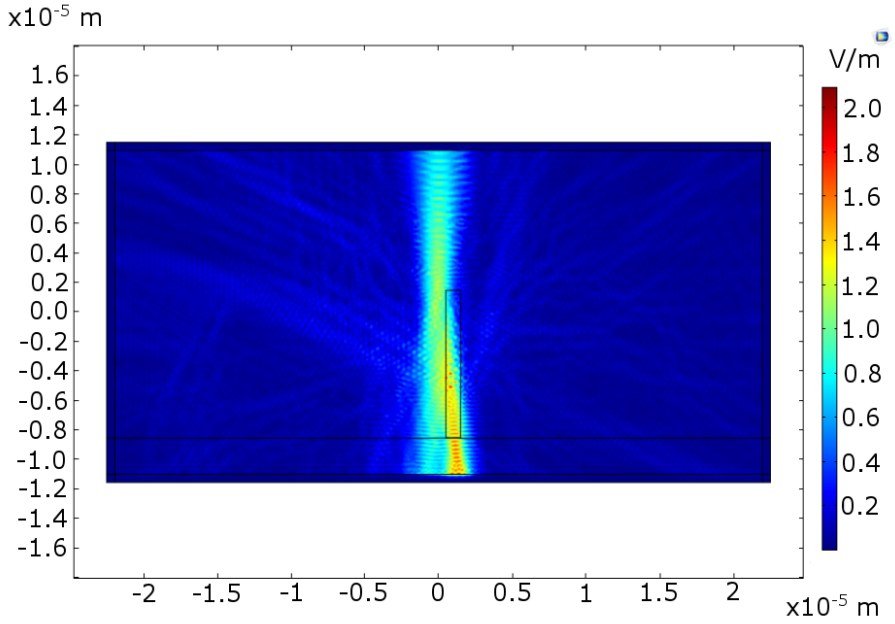

Figure 4.6: Simulation of a beam passing through a block of solid polymer.

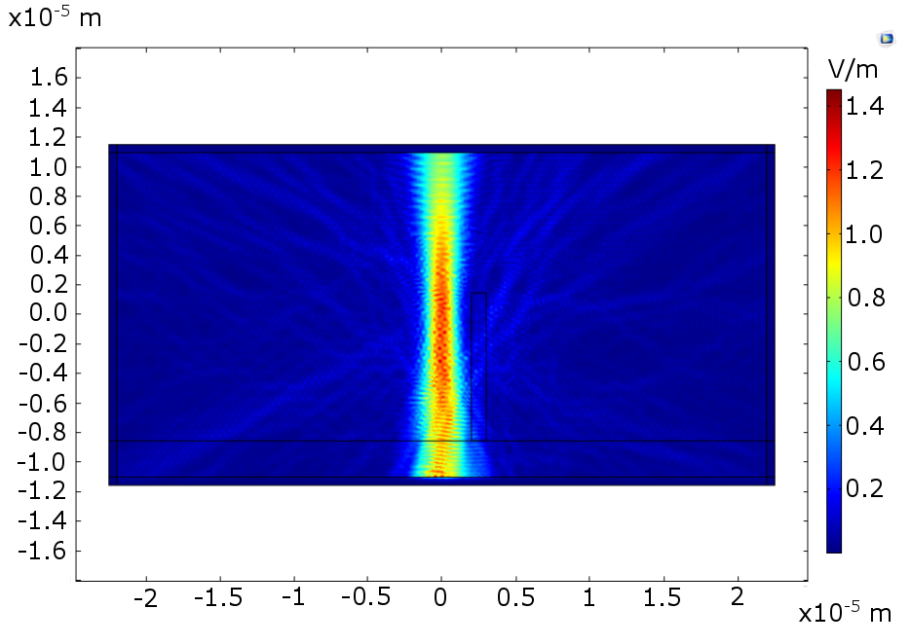

Figure 4.7: Simulation of a beam passing by a block of solid polymer without going through it.

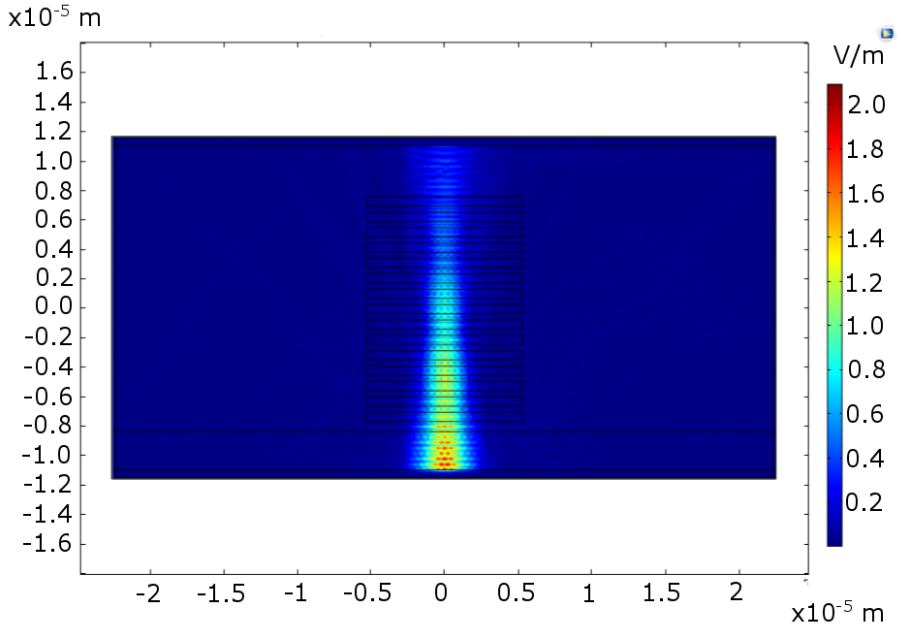

Figure 4.8: Simulation of a beam incident on a set of layers of solidified polymer.

problem because they would provide better support for layers. Figures 4.9,4.10 are two sample images of relevant stacks. As predicted by the theory that large enough pieces of solid IP-L 780 cause the distortion, the distortion increases with pillar width.

The distortion was quantified by measuring the width of the upper layer of the stack: the distance between the left edge and the right edge of the upper layer. Figure 4.11 is a graph of the width of the upper layers of the stacks above. The width of the upper layers decreases with increasing pillar size, which illustrates the way that pillars can distort writing.

Another potential structural problem that can be seen in the above images is a seam running from the centre of the stack to one of the pillars. Each layer in the stack is written as a set of concentric hexagons starting at the edge of the stack and getting smaller. In the stacks shown above, each hexagon started at the same pillar as the previous hexagon. One explanation of the seam is that the place where the writing starts is not written as well as the other corners because the beam turns off when it reaches that corner to move on to the next hexagon. This seam was eliminated by changing the writing process so that after a hexagon was finished, the next hexagon started writing at the next pillar clockwise around the stack when looking from the top of the stack. The writing patterns are shown in figure 4.12. Figure 4.13 shows the stack written with the pattern on the left. Figure 4.14 shows the stack written with the pattern on the right.

The stacks shown in Figure 4.14 have layers of uniform width from top to bottom. They also do not have any visible flaws in SEM images. So these structures are promising candidates to function as Bragg stacks.

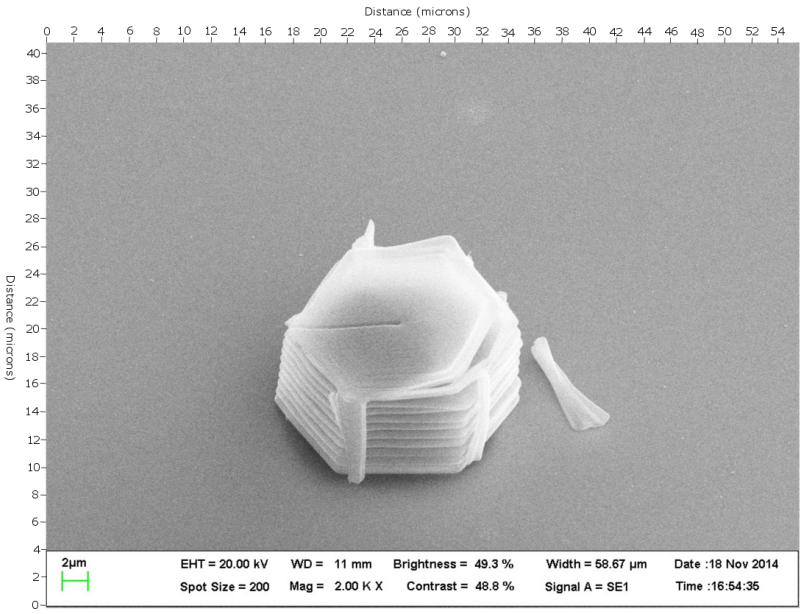

Figure 4.9: SEM image of stack with plates of width 8 microns and pillars of width 1.0 μm. The stack was designed, made and imaged by the author.

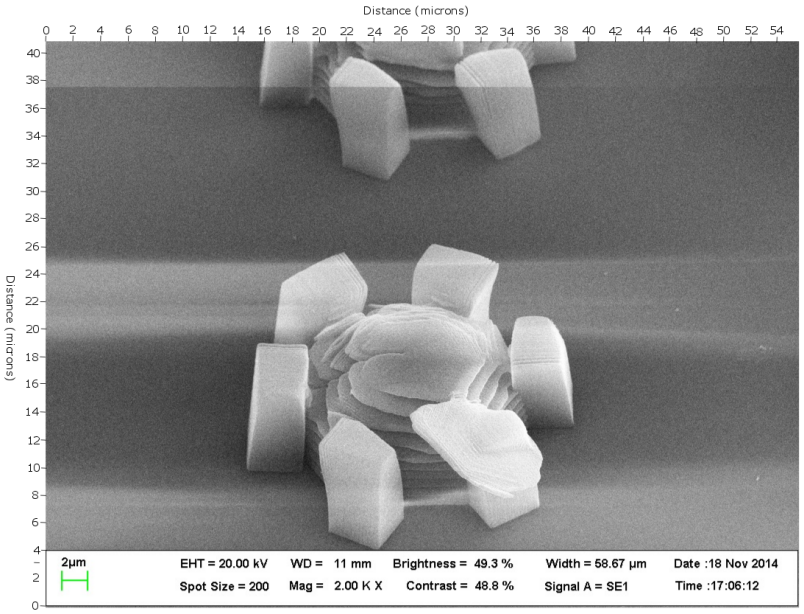

Figure 4.10: Stack with plates of width 8 microns and pillars of width 4.5 μm. The stack was designed, made and imaged by the author.

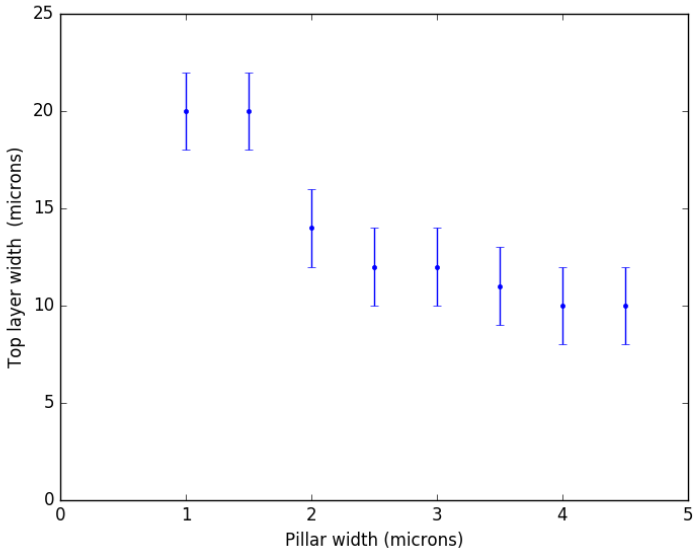

Figure 4.11: Graph of width of upper layers of stacks as a function of pillar size.

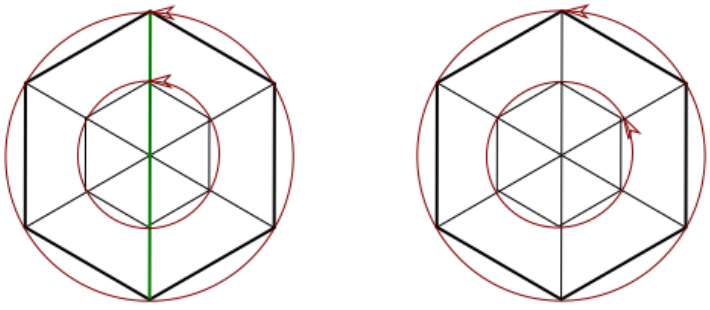

Figure 4.12: Diagrams showing the pattern in which layers were written. The red arrows show the direction and final point of the writing in the relevant hexagon. The green line in the first diagram will be underexposed.

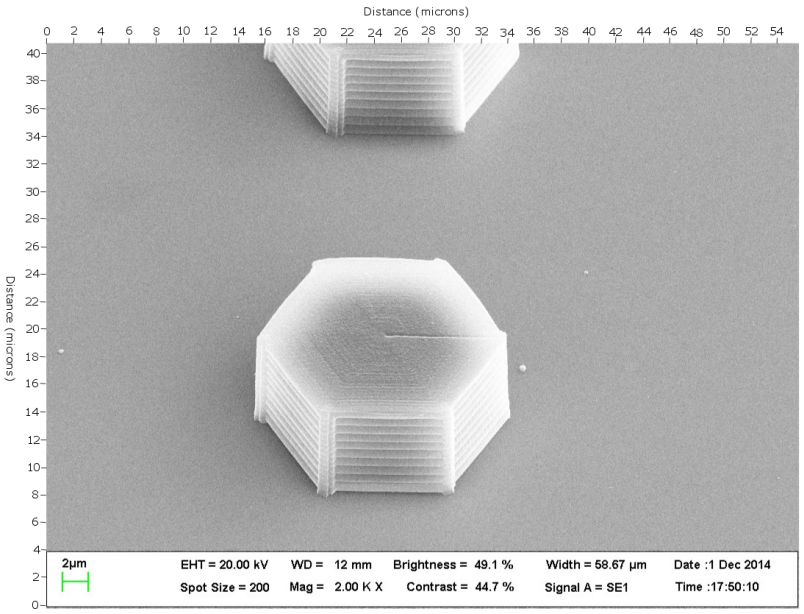

Figure 4.13: A stack written with the pattern on the left of Figure 4.12. The stack was designed, made and imaged by the author.

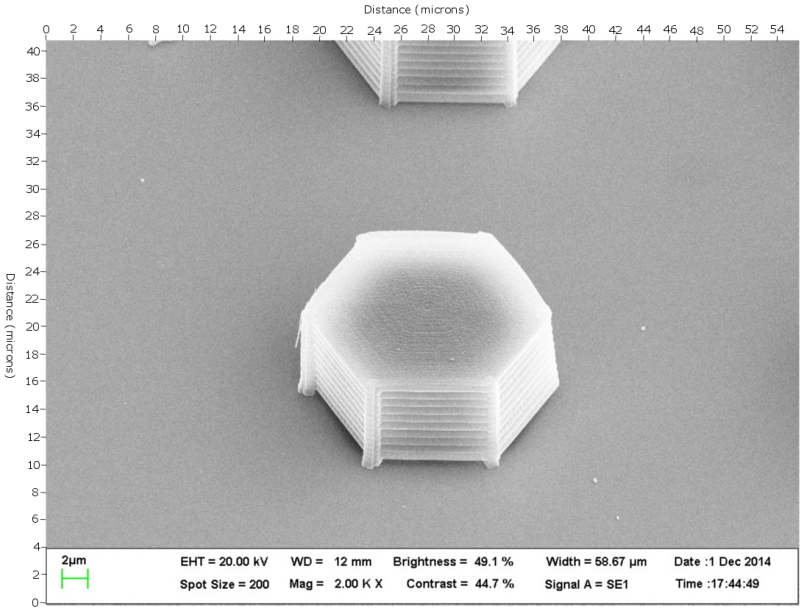

Figure 4.14: A stack written with the pattern on the right of Figure 4.12, with the same settings as in figure 4.13. The stack was designed, made and imaged by the author.

4.2 Theory of stacks

The stacks were assessed by measuring their transmission spectra and comparing them to theoretical predictions of transmission spectra. To make the relevant predictions, we consider a stack with N identical unit cells with two layers whose refractive indices are n_1 and n_2 and whose layers have length a and b, shown in figure 4.15. Let f_j, r_j be the forward and backward propagating electric fields in a single unit cell. The account of the theory of such stacks in this section follows [109, Section 6.2].The matrix equations relating the fields in the $(n-1)$th unit cell to those in the nth are given by:

$$\begin{bmatrix} f_{n-1} \\ r_{n-1} \end{bmatrix} = \begin{bmatrix} A & B \\ C & D \end{bmatrix} \begin{bmatrix} f_{n-1} \\ r_{n-1} \end{bmatrix}. \tag{4.2}$$

In a layer with refractive index n_a, the component of the wave vector perpendicular to the interfaces between layers is given by

$$k_{az} = \sqrt{\left(\frac{2\pi}{\lambda}\right)^2 - k_{ay}^2}, \tag{4.3}$$

where y, z are the axes parallel and perpendicular to the interfaces and λ is the wavelength of the field. If the field is propagating at angle θ, then $k_{az} = \cos\theta \frac{2\pi n_a}{\lambda}$.

In general, the fields depend on the polarization of the incident light. For transverse electric (TE) polarization we have:

$$\begin{aligned} A_{TE} &= \exp(ik_{1z}a)(\cos k_{2z}b + \tfrac{i}{2}(\tfrac{k_{1z}}{k_{2z}} + \tfrac{k_{2z}}{k_{1z}})\sin k_{2z}b), \\ B_{TE} &= \exp(-ik_{1z}a)\tfrac{i}{2}(\tfrac{k_{2z}}{k_{1z}} - \tfrac{k_{1z}}{k_{2z}})\sin k_{2z}b, \\ C_{TE} &= -\exp(ik_{1z}a)\tfrac{i}{2}(\tfrac{k_{2z}}{k_{1z}} - \tfrac{k_{1z}}{k_{2z}})\sin k_{2z}b, \\ D_{TE} &= \exp(-ik_{1z}a)(\cos k_{2z}b - \tfrac{i}{2}(\tfrac{k_{1z}}{k_{2z}} + \tfrac{k_{1z}}{k_{2z}})\sin k_{2z}b). \end{aligned} \tag{4.4}$$

For transverse magnetic polarization (TM) we have:

$$\begin{aligned} A_{TM} &= \exp(ik_{1z}a)(\cos k_{2z}b + \tfrac{i}{2}(\tfrac{n_2^2 k_{1z}}{n_1^2 k_{2z}} + \tfrac{n_1^2 k_{2z}}{n_2^2 k_{1z}})\sin k_{2z}b), \\ B_{TM} &= \exp(-ik_{1z}a)\tfrac{i}{2}(\tfrac{n_2^2 k_{1z}}{n_1^2 k_{2z}} + \tfrac{n_1^2 k_{2z}}{n_2^2 k_{1z}})\sin k_{2z}b)\sin k_{2z}b, \\ C_{TM} &= -\exp(ik_{1z}a)\tfrac{i}{2}(\tfrac{n_2^2 k_{1z}}{n_1^2 k_{2z}} + \tfrac{n_1^2 k_{2z}}{n_2^2 k_{1z}})\sin k_{2z}b)\sin k_{2z}b, \\ D_{TM} &= \exp(-ik_{1z}a)(\cos k_{2z}b - \tfrac{i}{2}(\tfrac{n_2^2 k_{1z}}{n_1^2 k_{2z}} + \tfrac{n_1^2 k_{2z}}{n_2^2 k_{1z}})\sin k_{2z}b)\sin k_{2z}b). \end{aligned} \tag{4.5}$$

At normal incidence, the matrix elements are the same for each polarization and these equations reduce to

$$\begin{aligned} A &= \exp(in_1 ka)(\cos n_2 kb + \tfrac{i}{2}(\tfrac{n_2}{n_1} + \tfrac{n_1}{n_2})\sin n_2 kb), \\ B &= \exp(-in_1 ka)\tfrac{i}{2}(\tfrac{n_2}{n_1} - \tfrac{n_1}{n_2})\sin n_2 kb, \\ C &= -\exp(in_1 ka)\tfrac{i}{2}(\tfrac{n_2}{n_1} - \tfrac{n_1}{n_2})\sin n_2 kb, \\ D &= \exp(-in_1 ka)(\cos n_2 kb - \tfrac{i}{2}(\tfrac{n_2}{n_1} + \tfrac{n_1}{n_2})\sin n_2 kb).. \end{aligned} \tag{4.6}$$

We will assume that the light is incident on the stack at normal incidence so that these equations can be used. The validity of this assumption will be discussed in the next section when the experimental apparatus is described.

The reflected intensity from such a stack is $|r_N|^2 I$, where I is the incident intensity and $|r_N|^2$ is given by:

$$|r_N|^2 = \frac{|C|^2}{|C|^2 + 1/U_{N-1}^2}, \tag{4.7}$$

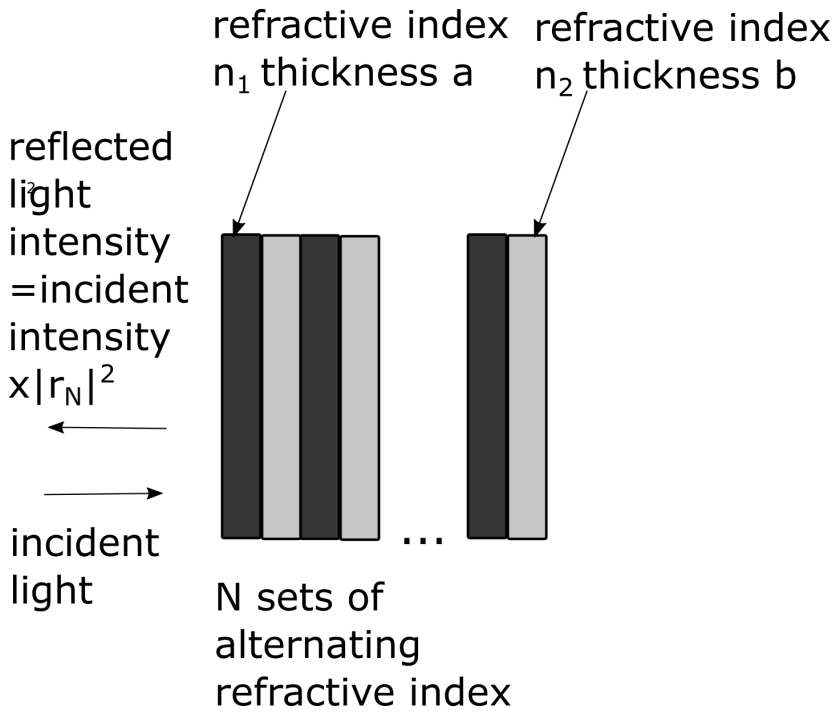

Figure 4.15: Transmission spectrum of the stack as designed.

and the U_N are Chebyshev polynomials of the second kind as a function of $\frac{1}{2}(A+D)$. Assuming that the absorption of the stack is negligible, the transmission should be $1-|r_N|^2$.

The most straightforward way to make a stack that reduces the transmission of light is to make the optical thicknesses of the alternating layers equal. Such a stack blocks transmission at wavelengths λ for which $(2n+1)\lambda/4 = t$, where t is the optical thickness of the layers and $n = 0, 1, 2 \ldots$.

In chapter 2, the depth of the voxels was calculated on the assumption that they are elliptical in cross section. If the depths calculated on that assumption are smaller than the real depth of a voxel, then layers could be stuck together as a result. So rather than rely on the model, it is useful to consider the maximum depth of voxel compatible with the experimental data. A structure made with that estimate gives the best possible chance of seeing an optical effect. It is possible to put an upper bound on how large the depth of a voxel can be given a measurement at angle θ. If the voxel is a straight line of zero thickness, then its thickness is $t_l = m/\sin\theta$. Any other shape would result in some distance being subtracted from that figure to account for the fact that the view of the voxel at angle θ includes the view of the top of the voxel at that angle. So the thickness of the voxel must be less than the t_l. The stacks to be tested were written with laser power 12mW at a speed of $25\mu m s^{-1}$, so if the layers are as thick as a single voxel then the thickness of the layers must be less than $0.36/\sin\frac{\pi}{4} = 0.51$ microns. A structure was designed to be a quarter wave stack assuming that the thickness of the polymer layer is 0.5 microns: the polymer layers are one voxel thick. The distance between polymer layers is $0.5 \times 1.5 = 0.75$ microns thick. If that calculation of the thickness of the layer is accurate, the transmission spectrum of the stack will be as depicted in figure 4.16. This spectrum and the others in this chapter were computed and plotted using Scipy [75].

However, this spectrum for the stack could be wrong if the stack does not turn out as designed. In particular, if the polymer layers are thicker or thinner than the above estimate, then the spectrum may be very different. If the sum of the thicknesses of

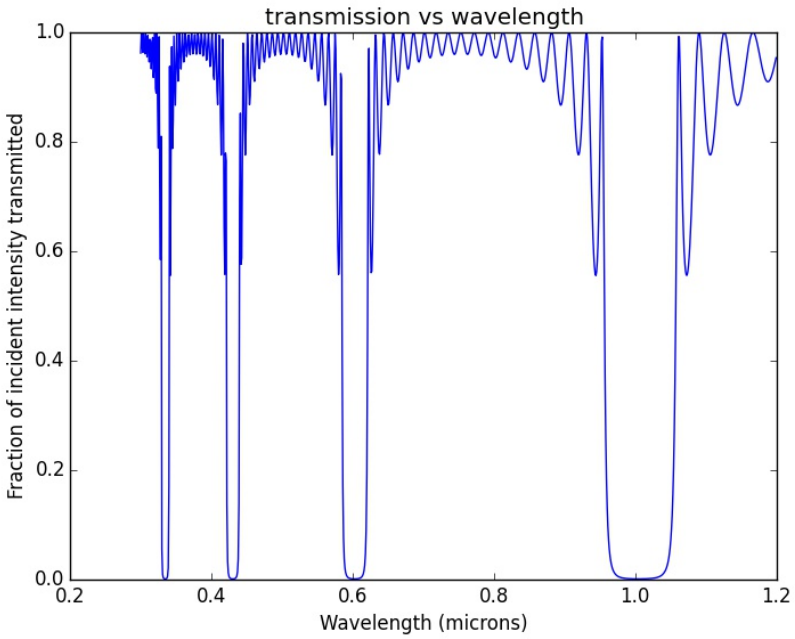

Figure 4.16: Transmission spectrum of the stack as designed.

the polymer and air layers remains the same $s = 0.75 + 0.5 = 1.25$ microns, the set of possible stacks could be described by a parameter f such that the thickness of the air layer is given by fs and the thickness of the polymer layer is given by $(1 - f)s$. A sample of such spectra are given below $f = 0.1$ in figure 4.17. The positions of dips in transmission vary with the air fraction, so if such dips are found in the spectra of light transmitted through stacks, their position may provide information about the air fraction in the stacks.

In addition, the transmission of stacks should vary with the number of layers. The minima of transmission will be shallower if there are fewer layers. For example, the spectrum for a stack with five layers and with air fraction 0.5 is shown in 4.18.

As a result, the transmission spectrum of a stack may give information about the number of intact layers as well as the air fraction.

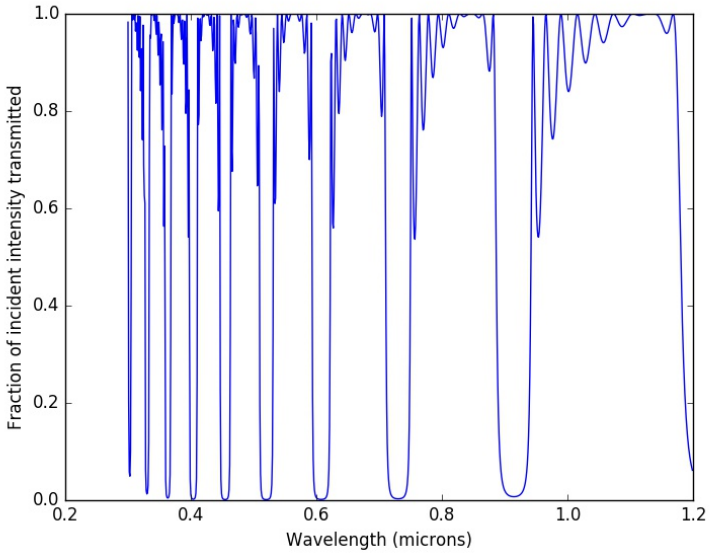

Figure 4.17: Transmission spectra of stack with air fraction 0.1.

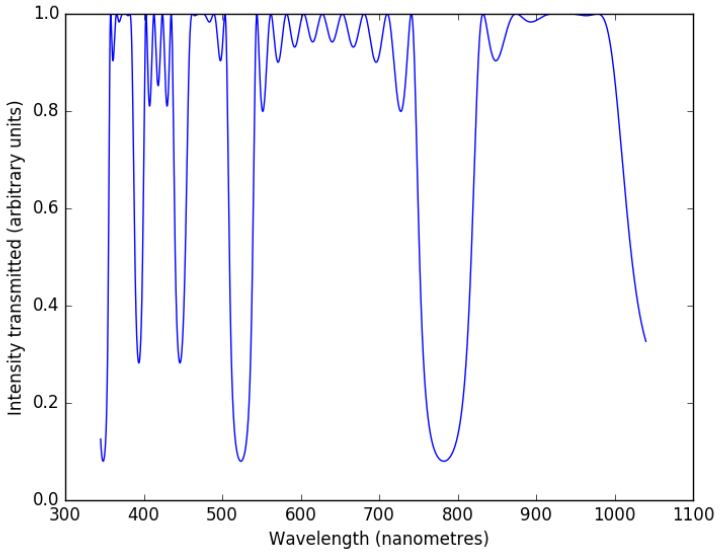

Figure 4.18: Transmission spectra of stack with five layers with air fractions 0.5.

4.3 Testing of stacks

The stacks were experimentally tested by illuminating one stack at a time with a white light source. The light was then gathered with a microscope objective and focused into an optical fibre connected to a spectrometer.

Each stack was illuminated by a fibre tungsten white light source coupled with a single fibre with a numerical aperture of 0.14, a 10 μm core and 125 μm cladding coupled to a tungsten white light source. The fibre was positioned under the coverslip, and the distance between the coverslip and the fibre was adjusted until only one stack was illuminated. The light from the fibre that had passed through the stack was then collected by a microscope objective. The light from the microscope objective goes through a lens and a prism that divides the light so that it passed down two optical paths. One of those paths directed the light to a USB camera, which was used to check the alignment of the fibre with the stack. On the other path light was directed to a multimode fibre mounted in an $x-y$ translation stage. The fibre was connected to an Ocean Optics USB 4000 VIS-NIR spectrometer. The fibre connected to the spectrometer was aligned with the stack by shining a laser through the detection fibre and adjusting the position of the illumination fibre and the sample until that laser was focused on the stack. A diagram of the optical layout is shown in figure 4.19. A photo of the apparatus is shown in figure 4.20.

The model given for the stack assumes that the field incident on the stack can be approximated by a plane wave. If the plane wave assumption is violated, then an accurate calculation of the spectrum would involve a weighted average over a range of angles. Since $k_{az} = \cos\theta 2\pi n_a/\lambda$ the spectrum would be shifted toward higher wavelengths as θ increases. To check this assumption, we calculate the angular spectrum of the light from the fibre and check the angle that contains 99% of the original intensity. The angular spectrum of light from a fibre can be approximated by [110, Section 20.5]:

$$\begin{aligned} |\psi(\theta)|^2 &= |\psi(0)|^2 \exp\left(-\frac{2\sin^2\theta}{\sin^2\theta_f}\right), \\ \sin^2\theta_f &= \frac{\lambda}{\pi w}, \\ V &= \frac{2\pi a NA}{\lambda}, \\ w_{core} &\approx a_{core}\left(0.65 + \frac{1.619}{V^{3/2}} + \frac{2.879}{V^6}\right), \end{aligned} \tag{4.8}$$

where w_{core} is the actual width of the core and a_{core} is an effective width used to approximate the angular spectrum by a Gaussian. This equation can be rearranged to find the angle at which $|\psi(\theta)|^2/|\psi(0)|^2 = \alpha$ for some $\alpha < 1$:

$$\cos\theta = \sqrt{1 + \frac{\sin^2\theta_f}{2}\ln(\alpha)}. \tag{4.9}$$

Where $\alpha = 0.01$, we find that $\cos\theta = 0.998$ at 900nm and $\cos\theta = 0.9996$ for 400nm. So light of wavelength 900nm would be mixed with light of wavelength up to about 901.8nm and light of wavelength 400nm would be mixed with light of wavelength up to 400.2nm. Since the experimental data were sampled at intervals of 0.2nm, the angular spread would be equivalent to averaging over 10 points at most. The experimental data were Gaussian smoothed over more than 10 points, so the angular spread of the light would not affect the results described in this chapter.

The transmission of a sample at wavelength λ can be measured by measuring the sample intensity S_λ, a reference intensity R_λ (the intensity of the light before it is incident on the structure being measured) and the dark intensity D_λ (the intensity when the light

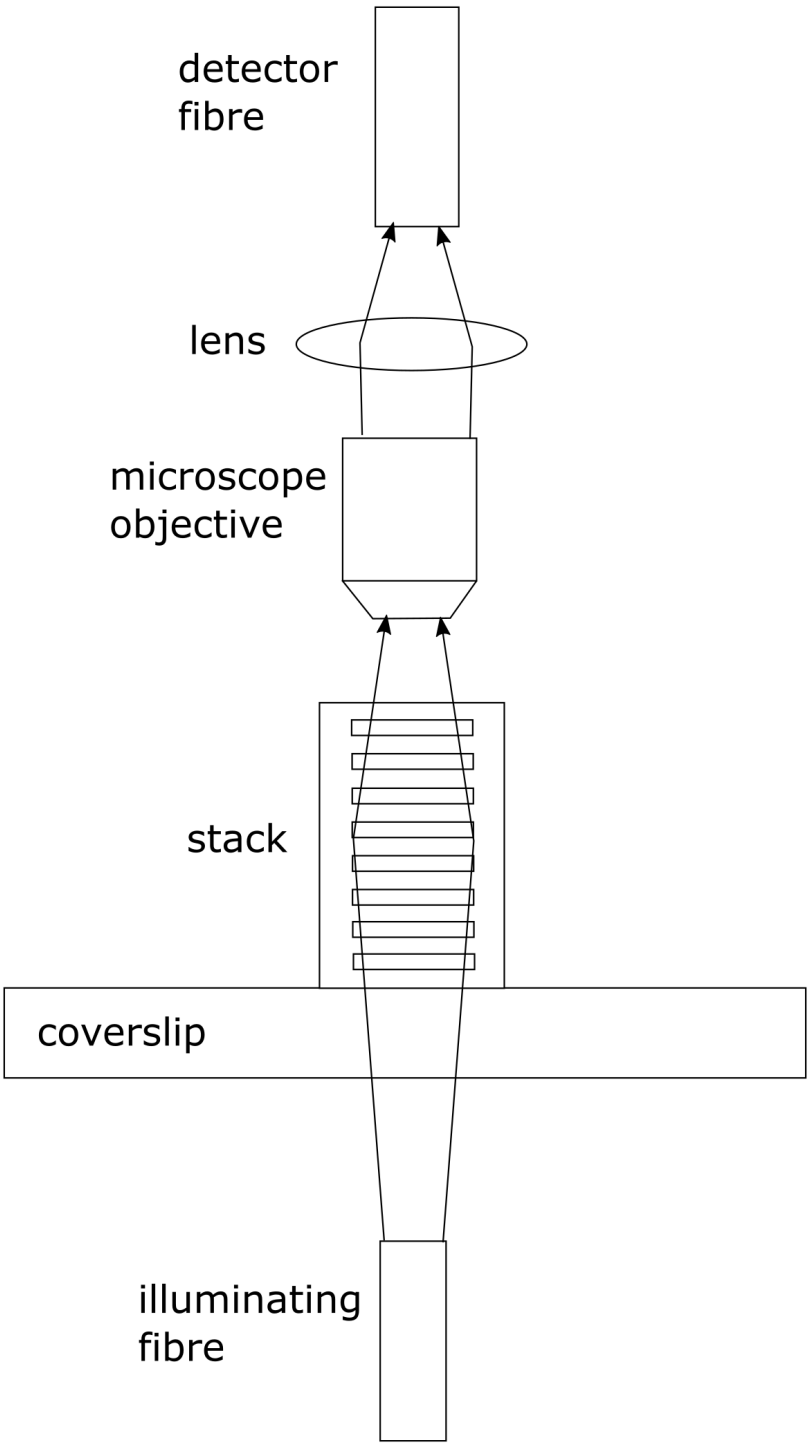

Figure 4.19: The optical system used to gather light from the sample. The arrows give an indication of the path of the light that passed through the system to the fibre leading to the spectrometer.

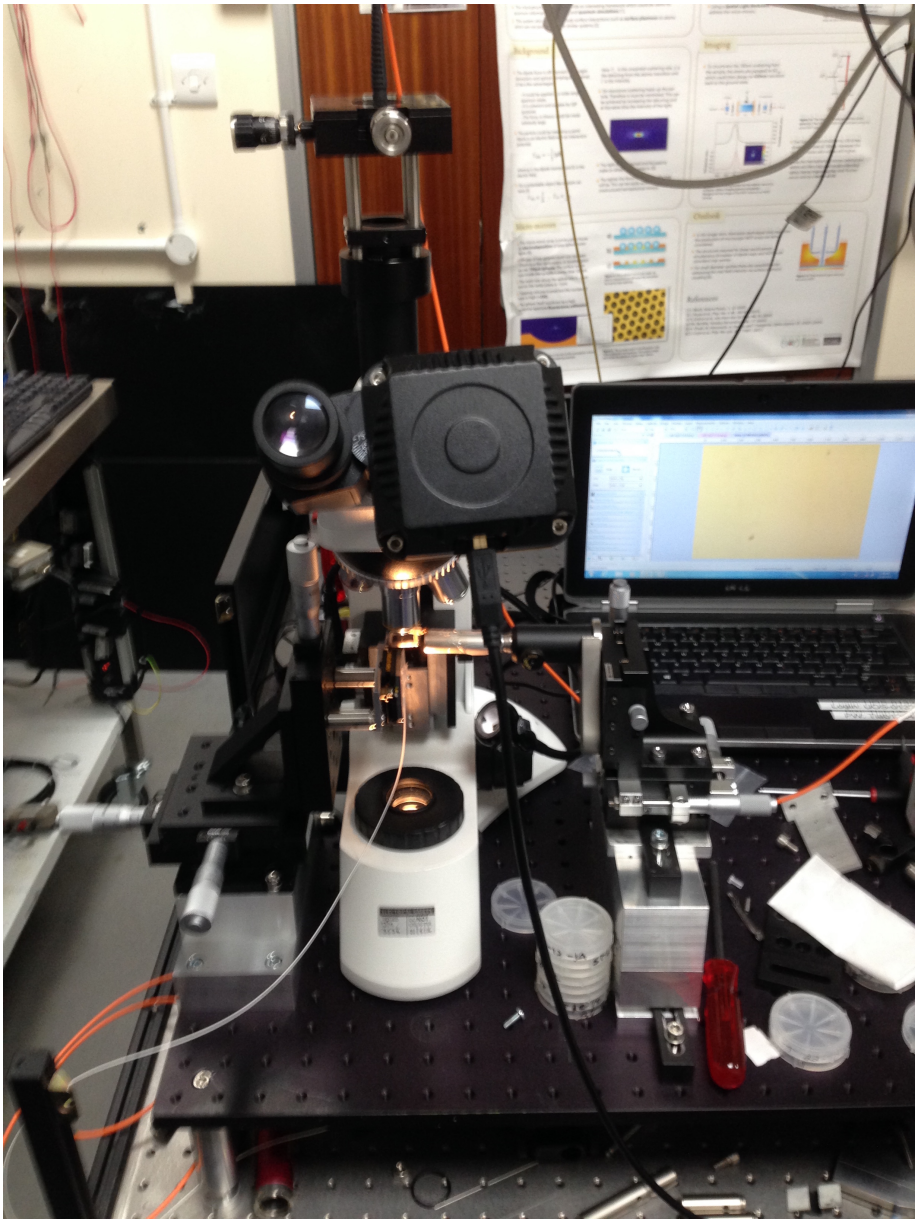

Figure 4.20: Experimental apparatus for measuring the transmission spectra of stacks.

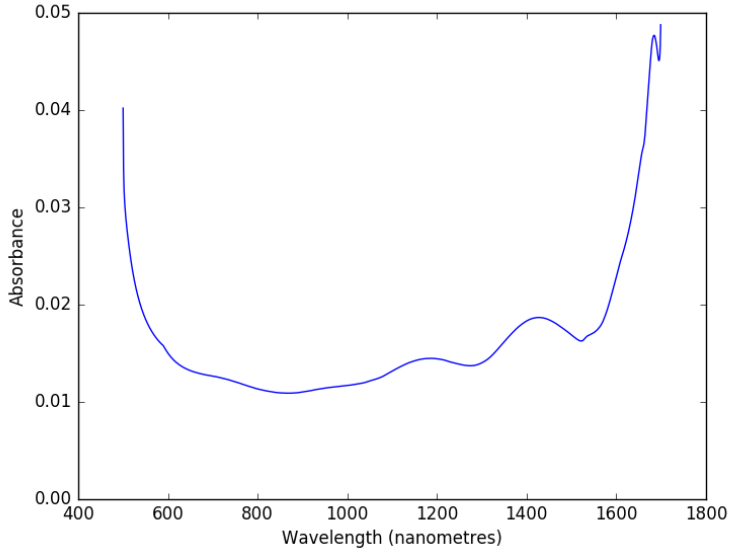

Figure 4.21: Absorbance of UV cured IP-L 780.

source is turned off) and the transmission is given by

$$T_\lambda = \frac{S_\lambda - D_\lambda}{R_\lambda - D_\lambda}. \tag{4.10}$$

In this case, since the sample is attached to a coverslip, the light must pass through the coverslip to get to the sample. So the reference intensity is the intensity of the light after it has passed through the coverslip.

The polymer itself may absorb some of the light passing through the stack. A transmission spectrum of a sample of the polymer was taken to provide the data to account for the effects of absorption in processing the measured spectra. A drop of liquid IP-L 780 was sandwiched between two slides, which were held separate by two coverslips on either side of the drop. The drop was then cured by a UV curing lamp. The absorbance of the samples was measured using a spectrophotometer. This spectrum was Gaussian smoothed over 181 points using Racket [111] and plotted using Scipy, see Figure 4.21. The number of points to be averaged was chosen by increasing the number of points averaged until enough high-frequency noise had been removed to make features such as maxima and minima discernible in the experimental data.

A stack has a thickness of IP-L 780 of the order of 10 microns. The sample of IP-L 780 is as thick as one coverslip: 170 microns. To use the absorption spectrum of polymerised IP-L 780, to adjust the transmission spectrum of the stack, assume that

$$T_\lambda = 10^{-\alpha_\lambda L_{samp}}, \tag{4.11}$$

where α_λ is the absorbance per unit length at λ and L_{samp} is the length of the sample. A spectrum can be adjusted to account for the absorption by multiplying it pointwise by T_λ for the thickness of material in the stack. In practice, this makes very little difference since the absorption is negligible for a sample of thickness 20 μm. The absorbance is less than 0.04 across most of the range for a sample of thickness 170 μm is 0.3–1.1 % at every wavelength in the measured range.

A reference spectrum was taken by measuring a transmission spectrum of light that passed through the coverslip but not the stack. A plot of the intensity of this light with a Gaussian moving average over 181 points is shown in figure 4.22.

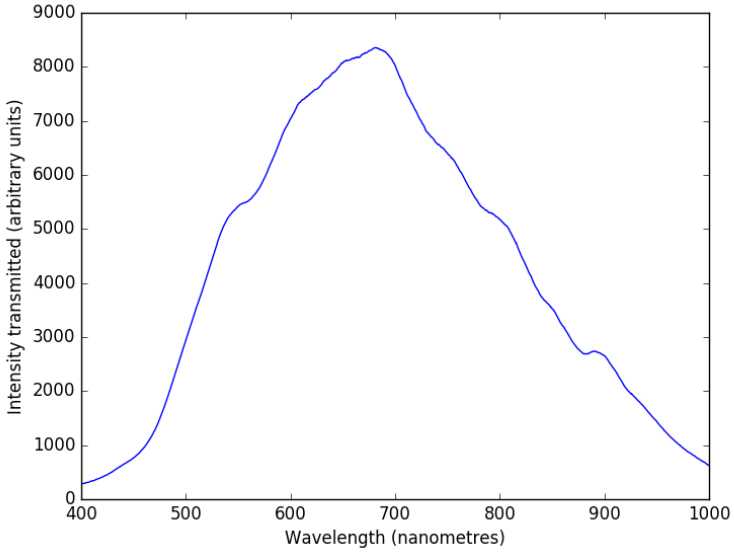

Figure 4.22: Smoothed measured spectrum of light that passed through a coverslip but not a stack.

Transmission spectra were taken of light that passed through the coverslip and the stack. A plot of the intensity of a particular sample with a Gaussian moving average over 181 points is shown in figure 4.23.

To predict the spectrum that would be detected a reference spectrum was multiplied pointwise by the predicted transmission spectra given in the previous section and the result was then put through the same Gaussian smoothing. The theoretical spectrum for a 10 period stack for air fractions 0.1 is shown below in figure 4.24 as an illustration.

The predicted and measured spectra were both normalised to reach a maximum value of 1 and then plotted on the same axes in cases where they looked like they might be a close match. One of the measured spectra looks similar to the predicted spectrum for a stack with two periods and an air fraction of 0.7, as illustrated in figure 4.25. The dip in transmission around 700-800nm resembles a feature in the predicted spectrum at the same wavelength.

None of the other spectra were as close a match for any of the predicted spectra. Some measured spectra had peaks of similar width and location but lacked features present in the predicted spectra. For example, one of the measured spectra 4.26 has a peak around 670nm that is similar in shape to the predicted peak in the spectrum of a stack with two periods and air fraction 0.6. This peak is very different from the spectrum of a coverslip without a stack, so the stack is having some effect on transmission. However, the measurements do not have a decrease in transmission that is present in the theoretical spectrum around 600nm.

Other measured spectra had minima in transmission but did not closely match any of the predictions, such as the spectrum in this example 4.27, which illustrates a measured spectrum and a predicted spectrum for a stack with 3 periods and an air fraction of 0.7.

The first spectrum 4.26 seems consistent with the idea that the stacks are functioning Bragg stacks. However, the theory does not account for the measurements taken from other stacks. Those spectra either lack some absorption features or have features that do not closely match any of the predictions. The model does not explain the predictions, but the measurement results also seem inconsistent with the stacks having no effect on transmission.

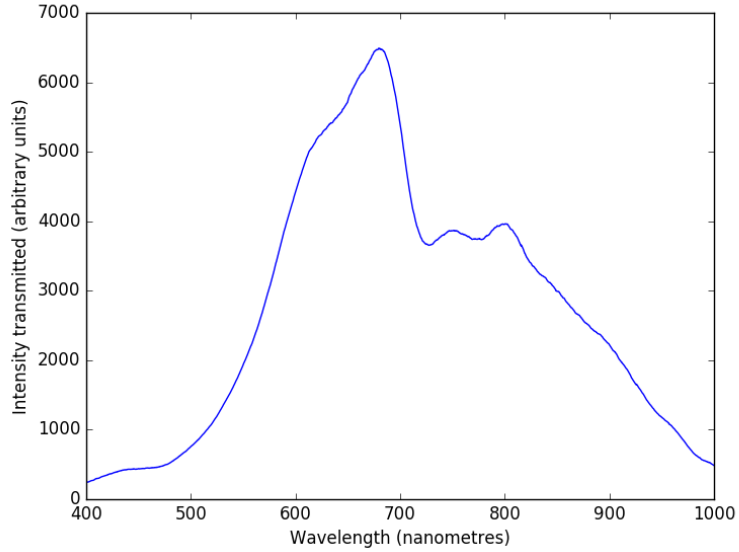

Figure 4.23: Smoothed measured transmission spectrum of light passing through a coverslip and a stack.

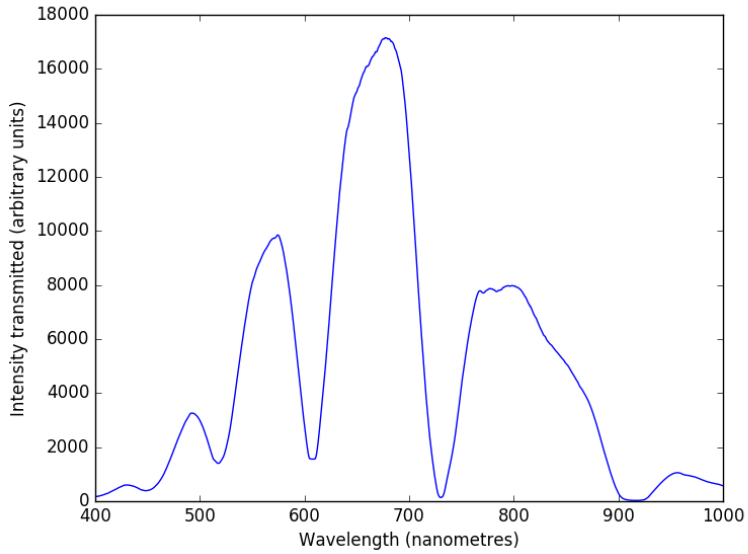

Figure 4.24: Predicted spectrum of a stack with 10 layers with air fraction 0.1.

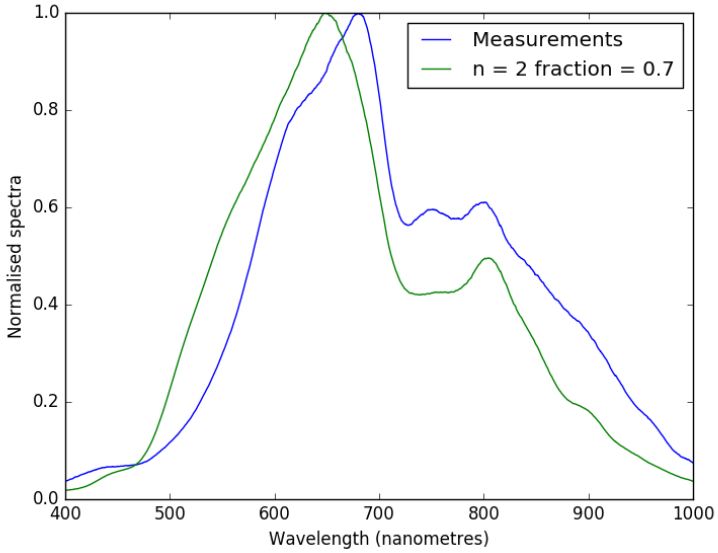

Figure 4.25: Predicted spectrum of a stack with 2 layers with air fraction 0.7 compared to a measured spectrum from one of the stacks. The green line is a theoretical prediction.

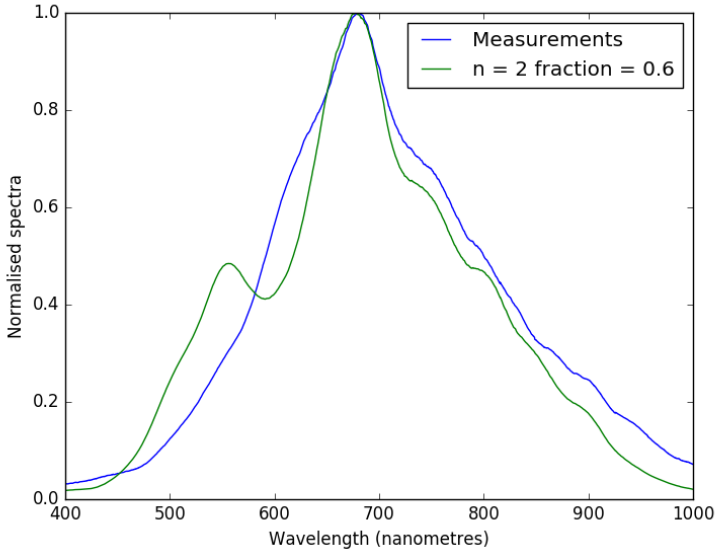

Figure 4.26: Predicted spectrum of a stack with two periods with air fraction 0.6 compared to a measured spectrum from one of the stacks. The green line is a theoretical prediction.

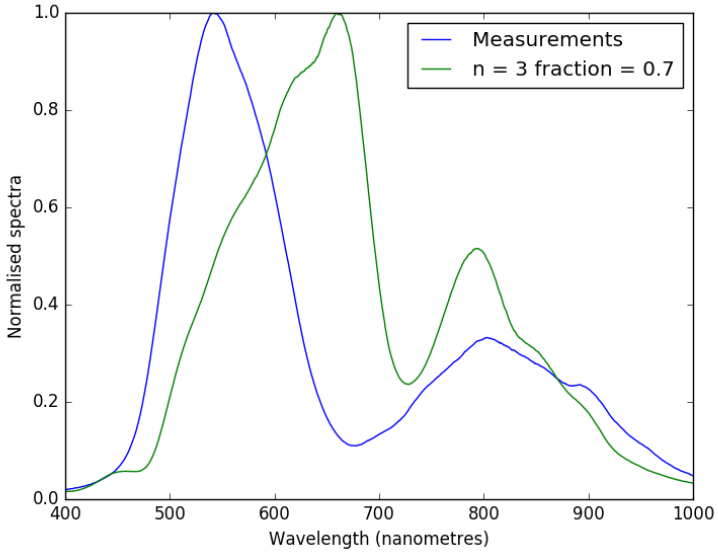

Figure 4.27: Predicted spectrum of a stack with 3 layers with air fraction 0.7 compared to a measured spectrum from one of the stacks. The green line is a theoretical prediction.

4.4 Conclusion

This chapter describes making Bragg stacks using the Nanoscribe and testing them.

The chapter describes some of the specifics of making a Bragg stack with a particular material IP-L 780 and a particular device the Nanoscribe. The plates in the stack should be written from top to bottom and the pillars should be 1 micron in width.

In addition, the experiments and models described here shed light on some more general considerations that should be taken into account when writing any structure using the Nanoscribe. Even if there is a difference of only 2% in refractive index between the written material and the raw material, the written material can change the distribution of light enough to stop a structure from being written according to plan. One way to avoid such problems is to write the structure so that the beam does not pass through the written material before it is focused. That prevents the beam from having to propagate through the material to write the rest of a structure. This may not always be possible as supports may have to be written so that a structure will stand up when it is written. Where it is not possible, simulations can help clarify how much material is necessary to disturb the distribution of light. In IP-L 780, the amount of material necessary to disrupt the writing was less than 2λ. When material of thickness of the order of 2λ is needed the distribution of light produced by such a structure should be simulated to check whether the writing process will be disrupted. Another problem is that some writing patterns will not evenly expose the region of the intended structure. One way to solve this problem that was used in this chapter is to exploit symmetries of a planned structure to start writing it in different positions so that the material is evenly exposed.

The transmission of stacks was tested and some of the results were compatible with the stacks reflecting light according to the standard theory of Bragg stacks. Many of the stacks suppressed transmission in a way that was not explained by the theory. However, the stacks did still reduce transmission, so more research on making Bragg stacks with the Nanoscribe may be worthwhile.

The minima in transmission in the experimental results shown in 4.27 are broader than any features predicted by the theory. If the stack sagged so that the gaps between

different layers varied over the size of the stack then the stack might block a broader range of wavelengths. Future research on Bragg stacks made using the Nanoscribe could look for ways to test this possibility.

Chapter 5

Conclusion and directions for future work

The objective of the project was to make optical actuators: photonic crystals that would undergo large quasi-static mechanical changes when illuminated. These crystals were to be made using the Nanoscribe [35]. The Nanoscribe used IP-L 780: a resist that can change state from liquid to solid as a result of chemical reactions when illuminated with light of a suitable wavelength. The change of state happens as a result of the formation of radicals, which occurs at a rate that depends on the square of the intensity of the illumination. As a result of this process, the Nanoscribe is capable of making structures with feature sizes of the order of 100nm. An optical actuator could be used for contactless actuation in a lab on a chip [5]. Some progress was made toward the stated objective. The feature sizes of structures produced by the Nanoscribe were characterised. Measurements were made of the Young's modulus of the polymer produced by the Nanoscribe. The optical properties of Bragg stacks made with the Nanoscribe were also tested.

5.1 Minimum feature sizes

Making an optical actuator with the Nanoscribe requires information on the size of features that can be made with the Nanoscribe. Data were gathered on the minimum feature size for structures written in IP-L 780. Lines were drawn between blocks using the Nanoscribe at different powers and at different movement speeds for the focus. The width of those lines was measured looking at the lines from the top and at an angle of 45 degrees. This information was used to calculate the depth of the line. So the experiments gave us information on both the width and the depth of the minimal feature size at various speeds and powers. The minimum and maximum measured widths of a line were 0.12 microns and 0.61 microns respectively. The minimum and maximum measured depths were 0.61 and 1 microns respectively. This information on its own could be useful for writing structures using IP-L 780.

In addition, the experimental data were fitted to models of voxel formation. These models assumed that voxels would form on the surface where the beam intensity dropped below some unknown threshold value. These models did not explain the data. The model fitted the data for the width for each individual power, but the parameters describing the fit were different for each data set. A fit for all of the width data together did not closely match the data. The model did not fit the data for the measured depth of the lines at all.

Another model was considered that incorporated the effects of a reaction that removed radicals without polymerisation at a rate proportional to their concentration. This model also did not account for the experimental results.

All of the data were successfully fitted to the function

$$y_T = \sqrt{f_s(P - f_i)\log\left(\frac{P^2}{v}g\right)}. \tag{5.1}$$

There is no theoretical motivation for this function. Future work could test this function in more cases and try to discover theoretical arguments for or against it.

5.2 Mechanical measurements

We conducted experiments to measure the Young's modulus of solid IP-L 780. Information about mechanical properties of IP-L 780 such as the Young's modulus would be necessary to predict the magnitude of the optical force required to produce actuation.

These experiments involved making beams running between cuboid blocks. The beams were then subjected those beams to forces of the order 10μN applied using the stylus of a KLA Tencor profiler. The stylus was moved along the beam and the height of the stylus above the substrate was measured as the force was applied. The height of the stylus was then fitted to a linear model of the response of the solid IP-L 780 to obtain estimates of the Young's modulus. These estimates varied between 4.7 GPa and 12 GPa and often varied by more than experimental error even in measurements of the same structure. These results are of the same order of magnitude as Nanoscribe's measured value of 4 GPa obtained using a nanoindenter. The results of the experiment were also compared to those of a Comsol model of a beam supported on two blocks: this model did not explain the results of the experiments. Some possible explanations that have not been ruled out include non-linear effects and variations in the shape and mechanical properties of the beams. Using smaller forces to eliminate the possibility of non-linear effects might produce more consistent results. Some other ways of measuring the Young's modulus are explained below, and might provide opportunities for future research.

Mechanical testing of microscopic materials is a well-known problem in MEMS applications, so it makes sense to consider whether these techniques could be adapted to measuring the Nanoscribe's output. Reviews of these techniques can be found in [112, 113].

One way to determine the Young's modulus of a material is to make a structure that should have resonant frequencies that depend on the Young's modulus and then measure the resonant frequency. Examples of such structures would include cantilever beams, simply supported beams and thin square or circular plates and calculations of their resonant frequencies can be found in papers such as [79]. Doing such measurements requires exerting forces on the structure at a controlled frequency and measuring the response of the structure. There are various ways of exerting the force, which include ultrasound and using an Atomic Force Microscope (AFM) cantilever. An AFM was available, but doing the measurement accurately requires having an accurate measurement of the spring constant of the cantilever. One means of doing the measurement is to measure the thermal noise spectrum of the cantilever [114, Section 2.3]. For an ideal spring with spring constant k_c, the noise spectrum would be related to the spring constant by

$$k_c = \frac{k_B T}{\langle Z_c^2 \rangle}. \tag{5.2}$$

However, the actual spring constant is not given by this formula because an actual cantilever is not an ideal spring. The actual spring constant is given by

$$k_c = \frac{k_B T}{\sum_i \alpha_i^4 \langle Z_{ci}^2 \rangle}, \tag{5.3}$$

where i is a label for the vibrational modes of the cantilever. The modes depend on the precise shape of the cantilever, so all of its plan dimensions have to be measured accurately and the resulting shape has to be simulated [115]. The medium in which the experiment is conducted also changes the resonant frequency. So accurate determination of the spring constant requires control over the surrounding medium, e.g. - by putting the experiment in an airtight box with a supply of gas with known properties.

Mechanical properties of a specimen can tested by fixing the specimen at one end and pulling the other end with some load. This method requires fixing one end of the sample, using some device that is capable of exerting a very small force and then measuring the resulting displacement. This requires a means of aligning the sample and applying the force. In MEMS, the problem of exerting the force and measuring the displacement is often solved by on-chip testing devices, such as comb drives [116]. This would require moving a Nanoscribe sample without damaging it or creating a comb drive on the coverslip without damaging the sample.

The mechanical properties of a membrane can be tested by attaching it to a support with a hole below it, exerting pressure on it and then measuring the displacement as a function of pressure [117]. The Nanoscribe can only make structures less than 300 microns in diameter. This would require making a substrate with a hole less than 300 microns in diameter. So it would be necessary to cut a 300 micron diameter hole in a coverslip without damaging the structure on top, or to transplant the membrane to such a hole with micron precision without damaging it.

Micro and nano indentation techniques involve pressing a hard tip with known properties into an unknown sample and measuring how deeply it penetrates as a function of force as the force is gradually ramped up and then reduced; for a review see [118]. For a suitable sample and a suitable indenter tip, this may be relatively easy to do experimentally. However, the analysis of the data can be difficult because the depth of penetration will depend on plastic as well as elastic properties, the shape of the tip and the roughness of the surface.

5.3 Writing structures

We conducted experiments to make Bragg stacks and measure their optical transmission. The experiments conducted to write the Bragg stacks provided information about writing patterns that could be applied to more general structures. The Bragg stacks consisted of pillars holding up plates of solid IP-L 780.

If the plates were written from the bottom of the stack (near the coverslip) to the top, then the plates further up the stack would not form properly. This was a result of the beam being fined to the lower parts of the stack by the layers written near the bottom. When a pillar was thicker than about one micron, and the beam passed through it, the highest intensity was confined to the pillar. So when trying to write structures, it is necessary to avoid having the beam passing through solid polymer. When designing a writing pattern, this problem should be borne in mind and simulations of the intensity distribution should be conducted in regions where the laser beam will overlap with solid resist.

The writing pattern for making a structure should also be carefully chosen to ensure even exposure of the region to be polymerised. For example, to write a shape with some

rotational symmetry the rotation should not always start at the same spoke since that spoke will be under-exposed.

When stacks had been written they were optically tested. We illuminated them with white light from an optical fibre and then measured the transmitted light. The measurement results varied from one stack to another. The results were compared to a theoretical model for Bragg stacks for various numbers of layers and distances between layers.

The Bragg stacks were written, placed in a solvent to remove the remaining liquid IP-L 780 and then dried out using critical point drying. Critical point drying involves replacing solvent with liquid carbon dioxide and then taking the carbon dioxide from liquid to gas without a sudden phase transition using the critical point: the pressure and temperature where the liquid and gas phases are indistinguishable [72–74]. We do not know of any specific reason to think this process could have been adjusted to produce more consistent Bragg stacks.

It is also possible that Bragg stacks are not robust regardless of how they are dried. The plates in the stack might be easily removed or disturbed regardless of how the sample is handled. Alternatively, the plates may sag under their weight in the middle in a way that produces inconsistent results. Simulations of how Bragg stacks sag under gravity using the values found for the Young's modulus might shed light on this problem.

Future investigations might consider making other kinds of structures that might be more robust while also having optical effects such as woodpiles. Woodpiles do not feature large plates that might sag or be easily removed by mechanical disturbance. Woodpiles have been made using two photon polymerisation [36–44].

Another area where progress might be made concerns simulations of the writing process. There are some artefacts in the simulations described in Chapter 4. The finite element method can also be computationally expensive for large systems since it requires decomposing the region into a fine mesh. Other methods might be less computationally expensive and could lead to fewer artefacts if implemented carefully. The plane wave time domain method [119–121] involves decomposing the field into plane waves instead of modelling the field at each point. The beam propagation method [122, 123] uses the slowly varying envelope approximation and calculates the envelope of the field rather than the carrier. If the envelope varies relatively slowly then this takes fewer computational resources while still being a good approximation.

The work described in this thesis may help with the design of such structures by providing information about what feature sizes can be produced, guidance about how they should be written and information about the mechanical properties of solid IP-L 780.

Appendices

Appendix A

Nanoscribe programming

To produce a structure the Nanoscribe must be given files that contain sets of coordinates, instructions on how to change the power of the laser beam, and whether the laser should be left on or turned off between any particular pair of coordinates. The coordinates and the relevant structures are described in a programming language called general writing language (GWL) developed by Nanoscribe.

In GWL a point is described by a line in the file containing three numbers that represent (x, y, z) coordinates given in microns. If one set of coordinates follows directly after another set of coordinates, then the laser is turned on between those coordinates and the Nanoscribe will draw a line. If a set of coordinates is separated by a line with the word "write", then the laser will be turned off between those sets of coordinates. If the laser is turned on between some set of points, then the speed it moves between those points will be $v = \text{PointDistance} \times \text{UpdateRate}$ in nm s^{-1}. If the laser is turned off between two points, then the time the Nanoscribe will take to move between the points is given in milliseconds by DwellTime. Lines with % at the start are comments. A brief commented example program is given below:

```
PointDistance 25 % Sets the point distance to 25 nm.

UpdateRate 1000 % Sets the update rate to 1000 s^-1

% These two lines together set the speed to 25 μms^-1

DwellTime 100 % Sets the Dwell Time to 100 ms.

LaserPower 60 % Sets the laser power to 12 mW.

0 0 0 % Starts drawing a line at (0, 0, 0).

10 0 0 % Continues the line to (10, 0, 0).

write % Turns off the laser and moves the focus to the next point in 100
    ms.

20 0 0 % Starts drawing a line at (20, 0, 0).

30 0 0 % Continues the line to (30, 0, 0).
```

Simple GWL files were often written by hand. More complicated files were generated by a program written in the Clojure programming language [124]. This program could also calculate the time required to write a file and check for problems with a file such as overlapping structures.

Appendix B

Tables of fitted results of mechanical tests

Sample, Batch	Force (μ N)	$a(\mu m^{-5})$	$\delta a(\mu m^{-5})$	$L(\mu m)$	$\delta L(\mu m)$	E (GPa)	δE (GPa)
1b,2	19.6	-1.64×10^{-10}	9×10^{-12}	13	1	7.2	0.2
1b,2	19.6	-1.36×10^{-10}	9×10^{-12}	13	1	7.2	0.2
1b,2	19.6	-1.32×10^{-10}	9×10^{-12}	13	1	7.2	0.2
1b,2	19.6	-1.07×10^{-10}	8×10^{-12}	11	2	7.4	0.2
1b,2	9.8	-8.9×10^{-11}	9×10^{-12}	8	2	7.1	0.2
1b,2	9.8	-8.1×10^{-11}	8×10^{-12}	7	2	7.0	0.2
1b,2	9.8	-8.0×10^{-11}	8×10^{-12}	7	2	7.2	0.2
1f,2	19.6	-1.47×10^{-9}	9×10^{-12}	46	108	5.6	0.1
1f,2	19.6	-1.46×10^{-9}	8×10^{-12}	46	13	5.6	0.1
1f,2	9.8	-1.8×10^{-10}	1×10^{-11}	7	1	6.8	0.1
1f,2	9.8	-1.1×10^{-10}	1×10^{-11}	3	2	6.9	0.2
1f,2	49	-1.08×10^{-10}	6×10^{-12}	14	1	8.4	0.3
1f,2	49	-1.04×10^{-10}	5×10^{-12}	14	1	8.4	0.3
1f,2	9.8	-8.71×10^{-11}	9×10^{-12}	2	2	7.2	0.2
2b,2	9.8	-3.48×10^{-9}	4×10^{-11}	65	26	4.7	0.1
2b,2	9.8	-2.73×10^{-9}	3×10^{-11}	65	42	5.1	0.1
2b,2	9.8	-7.7×10^{-11}	9×10^{-12}	14	3	6.8	0.3
2b,2	19.6	-1.1×10^{-11}	3×10^{-12}	31	13	11	1
2b,2	9.8	-5×10^{-12}	3×10^{-12}	33	25	10	1
2f,1	9.8	-4.4×10^{-9}	6×10^{-10}	9.178	1.362	6.8	0.2
2f,2	9.8	-5.9×10^{-11}	6×10^{-12}	19	3	6.5	0.3
2f,2	9.8	-4.4×10^{-11}	8×10^{-12}	14	5	7.1	0.3
2f,2	19.6	-1.7×10^{-11}	4×10^{-12}	34	9	9.6	0.7
2f,2	9.8	-2×10^{-12}	2×10^{-12}	76	52	12	9

Table B.1: Table of fitted values of and errors for a and the Young's modulus. The number after the comma in the Sample, Batch column is the batch number. A letter f after the Sample, Batch number denotes a forward scan (left to right), by denotes a backward scan (right to left).

Sample, Batch	Force (μN)	$a(\mu m^{-5})$	$\delta a(\mu m^{-5})$	$L(\mu m)$	$\delta L(\mu m)$	E (GPa)	δE (GPa)
3b,1	9.8	-6.1×10^{-9}	7×10^{-10}	25.1151	1.124	7.6	0.2
3b,1	9.8	-5.8×10^{-9}	7×10^{-10}	25.4768	1.203	7.6	0.2
3b,2	9.8	-2.2×10^{-10}	1×10^{-11}	22	1	6.4	0.2
3b,2	9.8	-9×10^{-12}	4×10^{-12}	27	17	10.4	0.9
3f,1	9.8	-5.8×10^{-9}	6×10^{-10}	10.9036	1.033	7.5	0.2
3f,2	9.8	-2.82×10^{-9}	2×10^{-11}	50	91	5.3	0.2
3f,2	9.8	-2.44×10^{-9}	2×10^{-11}	50	36	5.3	0.2
3f,2	9.8	-2.35×10^{-9}	2×10^{-11}	50	115	5.3	0.2
3f,2	19.6	-1.2×10^{-11}	3×10^{-12}	46	10	11.7	0.8
3f,2	19.6	-1.1×10^{-11}	3×10^{-12}	46	10	11.8	0.9
4b,1	9.8	-1.1×10^{-9}	2×10^{-10}	12.7203	2.463	8.2	0.4
5b,2	9.8	-1.1×10^{-10}	3×10^{-11}	19	4	8.0	0.2
5b,2	9.8	-5×10^{-12}	4×10^{-12}	21	32	9.0	0.8
5f,2	9.8	-2×10^{-10}	2×10^{-10}	27	59	7.6	0.1
6b,2	9.8	-1.47×10^{-9}	3×10^{-11}	62	42	6.8	0.2
6b,2	9.8	-2×10^{-11}	1×10^{-11}	1	16	7.7	0.4
6f,2	9.8	-1.26×10^{-9}	2×10^{-11}	50	8	6.7	0.1
6f,2	19.6	-2.5×10^{-10}	2×10^{-11}	0.1	1.0	7.3	0.2
6f,2	19.6	-8×10^{-11}	1×10^{-11}	6	3	8.1	0.3
6f,2	9.8	-5×10^{-11}	2×10^{-11}	2	9	7.5	0.3
6f,2	9.8	-4×10^{-11}	1×10^{-11}	2	9	7.6	0.3
10b,1	9.8	-3.5×10^{-9}	6×10^{-10}	25	2	7.7	0.2
10b,1	9.8	-2.2×10^{-9}	34×10^{-10}	21	2	7.9	0.2
10f,1	9.8	-2.7×10^{-9}	4×10^{-10}	9	2	7.8	0.2
10f,1	9.8	-2.4×10^{-9}	4×10^{-10}	9	2	7.7	0.2
11f,1	9.8	-6.5×10^{-9}	8×10^{-10}	11	1	7.5	0.1
11f,1	9.8	-6×10^{-9}	1×10^{-9}	10	2	7.4	0.2
12b,1	9.8	-6.0×10^{-9}	9×10^{-10}	27	2	7.5	0.2
12b,1	9.8	-4.4×10^{-9}	8×10^{-10}	23	2	7.7	0.2
12f,1	9.8	-8.01×10^{-8}	8×10^{-10}	32	214	6.2	0.1
12f,1	9.8	-4.7×10^{-9}	9×10^{-10}	23	2	7.8	0.2
13b,1	9.8	-4.4×10^{-9}	7×10^{-10}	21	2	7.8	0.2
13f,1	9.8	-9×10^{-11}	6×10^{-11}	21	30	6.4	0.1
17b,1	9.8	-1.3×10^{-9}	2×10^{-10}	7	2	8.2	0.3
19b,1	9.8	-1.76×10^{-8}	4×10^{-10}	48	60	7.0	0.1
19f,1	9.8	-4.2×10^{-9}	6×10^{-10}	12	1	7.1	0.1

Table B.2: Table of fitted values of and errors for a and the Young's modulus. The number after the comma in the Sample, Batch column is the batch number. A letter f after the Sample, Batch number denotes a forward scan (left to right), by denotes a backward scan (right to left).

Sample, Batch	Force (μN)	$a(\mu m^{-5})$	$\delta a(\mu m^{-5})$	$L(\mu m)$	$\delta L(\mu m)$	E (GPa)	δE (GPa)
20b,1	9.8	-4.6×10^{-9}	6×10^{-10}	27	1	8.0	0.1
20b,1	9.8	-4.5×10^{-9}	6×10^{-10}	27	1	8.0	0.1
20f,1	9.8	-3.9×10^{-9}	6×10^{-10}	9	2	7.8	0.2
21b,1	9.8	-4.9×10^{-9}	7×10^{-10}	24	1	8.0	0.1
21b,1	9.8	-3.9×10^{-9}	6×10^{-10}	24	1	8.0	0.1
21b,1	9.8	-1.7×10^{-9}	4×10^{-10}	18	3	8.0	0.3
22f,1	9.8	-2.8×10^{-9}	3×10^{-10}	0.07	1	8.1	0.2
23f,1	9.8	-4.33×10^{-8}	5×10^{-10}	31	112	4.9	0.1
25b,1	9.8	-3.0×10^{-9}	3×10^{-10}	21.8291	1.097	7.5	0.2
25f,1	9.8	-2.7×10^{-9}	3×10^{-10}	0.352	1.31	7.8	0.2
26b,1	9.8	-2.1×10^{-9}	2×10^{-10}	19.2195	1.316	7.9	0.2
26f,1	9.8	-2.6×10^{-9}	2×10^{-10}	1.913	1.015	7.6	0.2
26f,1	9.8	-2.3×10^{-9}	2×10^{-10}	1.731	1.374	7.8	0.3
26f,1	9.8	-1.7×10^{-9}	2×10^{-10}	3.278	1.726	7.9	0.3

Table B.3: Table of fitted values of and errors for a and the Young's modulus. The number after the comma in the Sample, Batch column is the batch number. A letter f after the Sample, Batch number denotes a forward scan (left to right), by denotes a backward scan (right to left).

Appendix C

Ellipsometry

Ellipsometry is a technique for measuring optical properties of a sample. In ellipsometry, light is reflected from a sample and the relative phase and amplitude of the reflected light is used to gain information about the optical properties of the sample.

The light incident on (reflected from) the sample has two components E_{ipar}, E_{iperp} (E_{rpar}, E_{rperp}), which are polarised parallel and perpendicular to the sample. The polarisation state of light can be characterised by the quantity [125, Sections 1.3 and 3.4.2]:

$$\rho = \tan\psi \exp(i\Delta), \tag{C.1}$$

where the polarisation state of the light is given in terms of the Jones vectors by

$$\begin{bmatrix} E_{par} \\ E_{perp} \end{bmatrix} = |E| \cos\psi \begin{bmatrix} \tan\psi \exp(i\Delta) \\ 1 \end{bmatrix}, \tag{C.2}$$

and $|E|$ is the magnitude of the electric field.

The action of optical elements on the polarisation state of light can be expressed in terms of Jones matrices [125, Section 3.3]. The the M2000DI ellipsometer, which was used to do the refractive index measurement mentioned in 4.4 is a rotating compensator ellipsometer, which uses two kinds of optical components: polarizers and compensators. A polariser only allows one polarisation to pass through. If the polariser is used to control the polarisation incident on a sample it is called a polariser. If it is used to select a component of the electric field for a detector, then it is called an analyser. The Jones matrix of a polariser (analyser) is:

$$P(A) = \begin{bmatrix} 1 & 0 \\ 0 & 0 \end{bmatrix}. \tag{C.3}$$

A compensator is a piece of birefringent crystal, so its refractive index along the slow axis n_0 than the refractive index along the fast axis n_e. In a crystal of length d, this produces a phase difference between the polarisations of

$$\delta = \frac{2\pi|n_e - n_o|d}{\lambda}. \tag{C.4}$$

So the Jones matrix of a compensator is given by

$$C_\delta = \begin{bmatrix} 1 & 0 \\ 0 & \exp(i\delta) \end{bmatrix}. \tag{C.5}$$

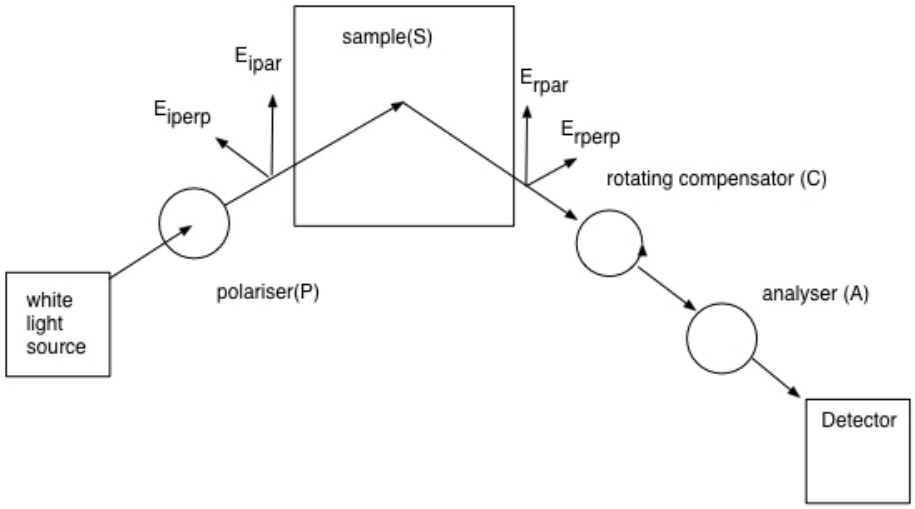

Figure C.1: Optical layout of a rotating compensator ellipsometer.

Compensators are often chosen so that they produce a $\pi/2$ phase change:

$$C_{\pi/2} = \begin{bmatrix} 1 & 0 \\ 0 & \exp(i\pi/2) \end{bmatrix}. \tag{C.6}$$

The final relevant Jones matrix is the Jones matrix that describes the effect of rotation of an optical component:

$$R_\alpha = \begin{bmatrix} \cos\alpha & -\sin\alpha \\ \sin\alpha & \cos\alpha \end{bmatrix}. \tag{C.7}$$

Next we have an example of a Jones matrix for a possible sample. The Jones matrix for light incident on a single dielectric interface at angle θ would be given by

$$R_\alpha = \begin{bmatrix} r_{par} & -0 \\ 0 & r_{perp} \end{bmatrix}, \tag{C.8}$$

where

$$\begin{aligned} r_{par} &= \frac{n\cos\theta - \cos\phi}{n\cos\theta + \cos\phi} \\ r_{perp} &= \frac{\cos\theta - n\cos\phi}{\cos\theta + n\cos\phi} \\ n\sin\phi &= \sin\theta. \end{aligned} \tag{C.9}$$

The refractive index will be written $n = n_r + ik$, where n_r is the real part of the refractive index and k is the imaginary part representing the absorption. In general the matrix for a real sample will be more complicated and will be composed out of many matrices representing different layers in the sample.

We are now in a position to explain the operation of a rotating compensator ellipsometer (RCE) along the lines given in [125, Section 4.2.4]. Figure C.1 shows the layout of the optical components of the RCE and the incident and reflected fields $\mathbf{E}_i = [E_{ipar}, E_{iperp}], \mathbf{E}_r = [E_{rpar}, E_{rperp}]$.

The field at the detector is represented by

$$\mathbf{E}_{out} = AR_A R_{-C} C R_C S R(-P) P \mathbf{E}_{in}. \tag{C.10}$$

The input field and the matrices of all of the components are known except for S. This equation can be used to obtain the S matrix by rotating the compensator at a controlled rate so that $C = \omega t$, and finding the Fourier components of the resulting signal.

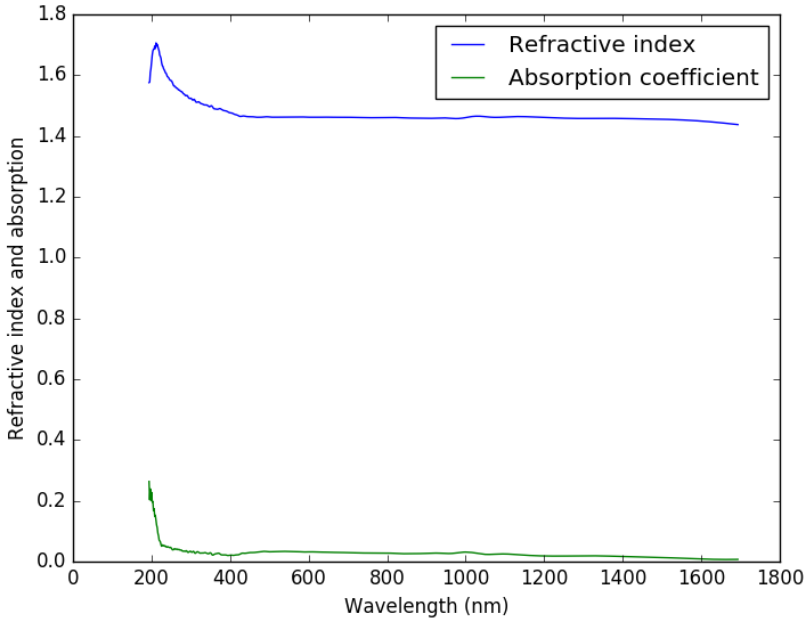

Figure C.2: Graph of the refractive and absorption coefficient of a sample of solid IP-L 780.

The data on the refractive index and absorption Elena Mavrona obtained from the RCE is shown in Figure C.2.

This shows the refractive index levels off after about 500nm at about 1.46. And above 500nm the absorption becomes negligible. The absorption results are similar to those obtained in chapter 4.4.

Bibliography

[1] K. C. Neuman and S. M. Block, Review of Scientific Instruments **75**, 2787 (2004).

[2] A. Xuereb and M. Paternostro, Physical Review A **87**, 023830 (2012), 1212.0641.

[3] A. Xuereb, C. Genes, and A. Dantan, Physical Review Letters **109**, 223601 (2012).

[4] A. Xuereb, C. Genes, and A. Dantan, Physical Review A **88**, 053803 (2013), 1304.4574.

[5] P. Neuzil, S. Giselbrecht, K. Lange, T. J. Huang, and A. Manz, Nature Reviews Drug Discovery **11**, 620 (2012).

[6] D. Baigl, Lab on a chip **12**, 3637 (2012).

[7] A. Terray, J. Oakey, and D. W. M. Marr, Applied Physics Letters **81**, 1555 (2002).

[8] S. Maruo and H. Inoue, Applied Physics Letters **89**, 144101 (2006).

[9] H.-t. Chen, A. J. Taylor, and N. Yu, Reports on Progress in Physics **79**, 076401 (2016), arXiv:1605.07672v1.

[10] J. D. Joannopoulos, S. G. Johnson, J. N. Winn, and R. D. Meade, *Photonic crystals: molding the flow of light*, Second ed. (Princeton University Press, Princeton, 2008).

[11] J. M. Bendickson, J. P. Dowling, and M. Scalora, Physical Review E **53**, 4107 (1996).

[12] A. Figotin and A. Klein, Journal of the Optical Society of America A **15**, 1423 (1998).

[13] M. C. Parker, R. J. Mears, and S. D. Walker, Journal of Optics A: Pure and Applied Optics **3**, S171 (2001).

[14] H.-B. Sun *et al.*, Applied Physics Letters **79**, 1 (2001).

[15] Z.-Y. Li and L.-L. Lin, Physical Review E **67**, 046607 (2003).

[16] Z.-Y. Li and K.-M. Ho, Physical Review B **68**, 155101 (2003).

[17] Y. Akahane, T. Asano, B.-S. Song, and S. Noda, Nature **425**, 944 (2003).

[18] L. Botten, N. Nicorovici, R. McPhedran, C. Sterke, and a. Asatryan, Physical Review E **64**, 046603 (2001).

[19] L. Botten *et al.*, Optics express **12**, 1592 (2004).

[20] L. Botten *et al.*, Physical Review E **70**, 056606 (2004).

[21] D. Englund and J. Vucković, Optics express **14**, 3472 (2006).

[22] K. Mnaymneh and R. C. Gauthier, Optics express **15**, 5089 (2007).

[23] S. V. Zhukovsky and S. V. Gaponenko, Physical Review E **77**, 046602 (2008).

[24] A. F. Oskooi *et al.*, Computer Physics Communications **181**, 687 (2010).

[25] S. Chakraborty, M. C. Parker, and R. J. Mears, Photonics and Nanostructures - Fundamentals and Applications **3**, 139 (2005).

[26] D. Englund, I. Fushman, and J. Vučković, Optics express **13**, 5961 (2005).

[27] Y. Akahane, T. Asano, B.-S. Song, and S. Noda, Optics express **13**, 1202 (2005).

[28] I. L. Garanovich, S. Longhi, A. a. Sukhorukov, and Y. S. Kivshar, Physics Reports **518**, 1 (2012).

[29] M. Antonoyiannakis and J. Pendry, Physical Review B **60**, 2363 (1999).

[30] P. T. Rakich, P. Davids, and Z. Wang, Optics express **18**, 14439 (2010).

[31] M. Sonnleitner, M. Ritsch-Marte, and H. Ritsch, EPL (Europhysics Letters) **94**, 34005 (2011).

[32] M. Sonnleitner, M. Ritsch-Marte, and H. Ritsch, New Journal of Physics **14**, 103011 (2012).

[33] J. Chan *et al.*, Nature **478**, 18 (2011), 1106.3614.

[34] T. A. Palomaki, J. W. Harlow, J. D. Teufel, R. W. Simmonds, and K. W. Lehnert, Nature **495**, 210 (2013), arXiv:1206.5562v1.

[35] Nanoscribe GmbH, Data Sheet Photonic Professional, 2013.

[36] J. Serbin and M. Gu, Journal of Applied Physics **98**, 123101 (2005).

[37] S. Juodkazis, V. Mizeikis, K. K. Seet, H. Misawa, and U. G. K. Wegst, Applied Physics Letters **91** (2007).

[38] M. Thiel, M. S. Rill, G. Von Freymann, and M. Wegener, Advanced Materials **21**, 4680 (2009).

[39] M. Thiel, J. Fischer, G. Von Freymann, and M. Wegener, Applied Physics Letters **97**, 1 (2010).

[40] M. Thiel *et al.*, Cleo: 2013 , ATu2N.4 (2013).

[41] E. Waller, M. Renner, M. Thiel, a. Radke, and G. V. Freymann, **1038**, 76344 (2013).

[42] S. Wong *et al.*, Advanced Materials **20**, 4097 (2008).

[43] C. De Marco *et al.*, Langmuir : the ACS journal of surfaces and colloids **29**, 426 (2013).

[44] L. C. Montemayor, L. R. Meza, and J. R. Greer, Advanced Engineering Materials **16**, 184 (2014).

[45] Y. Dong *et al.*, Polymers for Advanced Technologies **18**, 519 (2007).

[46] M. Kempe, P. Westphal, W. Grau, and G. von Freymann, Laser beam machining, 2013.

[47] M. Malinauskas *et al.*, Proceedings of SPIE **7715**, 77151F (2010).

[48] J. Serbin *et al.*, Optics letters **28**, 301 (2003).

[49] M. Farsari, G. Filippidis, and C. Fotakis, Optics Letters **30**, 3180 (2005).

[50] D. Tan *et al.*, Applied Physics Letters **90**, 9 (2007).

[51] M. Thiel and M. Hermatschweiler, Method and device for a spatially resolved introduction of an intensity pattern comprising electro-magnetic radiation into a photosensitive substance as well as applications thereof, 2012.

[52] M. Thiel and H. Fischer, Method and device for a spatially resolved introduction of an intensity pattern comprising electro-magnetic radiation into a photosensitive substance as well as applications thereof, 2012.

[53] L. J. Jiang *et al.*, SPIE Photonics West 2014-LASE: Lasers and Sources **8969**, 896909 (2014).

[54] J. B. Mueller, J. Fischer, F. Mayer, M. Kadic, and M. Wegener, Advanced materials (Deerfield Beach, Fla.) **26**, 6566 (2014).

[55] F. Niesler and M. Hermatschweiler, Laser Technik Journal **11**, 54 (2016).

[56] G. Odian, *Principles of polymerization*, Fourth edi ed. (Wiley, Hoboken, 2004).

[57] W. Peticolas, Annual Review of Physical Chemistry **18**, 233 (1967).

[58] B. Harke, P. Bianchini, F. Brandi, and A. Diaspro, Chemphyschem : a European journal of chemical physics and physical chemistry **13**, 1429 (2012).

[59] A. Pikulin and N. Bityurin, Physical Review B **75**, 195430 (2007).

[60] X. Zhou, Y. Hou, and J. Lin, AIP Advances **5** (2015).

[61] H.-B. Sun, K. Takada, M.-S. Kim, K.-S. Lee, and S. Kawata, Applied Physics Letters **83**, 1104 (2003).

[62] K. Takada, H.-B. Sun, and S. Kawata, Applied Physics Letters **86**, 071122 (2005).

[63] T. Tanaka, H. B. Sun, and S. Kawata, Applied Physics Letters **80**, 312 (2002).

[64] F. Burmeister *et al.*, Journal of laser applications **24**, 042014 (2012).

[65] S. Kawata and H.-B. Sun, Applied Surface Science **208-209**, 153 (2003).

[66] C. Yuan *et al.*, Journal of Nonlinear Optical Physics & Materials **23**, 1450015 (2014).

[67] W. H. Teh *et al.*, Applied Physics Letters **84**, 4095 (2004).

[68] S. S. M. Kuebler *et al.*, Journal of Photopolymer Science and Technology **14**, 657 (2001).

[69] W. Haske *et al.*, Optics express **15**, 3426 (2007).

[70] J. F. Xing *et al.*, Applied Physics Letters **90**, 31 (2007).

[71] J. W. Perry *et al.*, Conference on Lasers and Electro-Optics, 2007, CLEO 2007 , 12 (2007).

[72] C.-J. Kim, J. Y. Kim, and B. Sridharan, Sensors and Actuators A: Physical **64**, 17 (1998).

[73] G. L. Weibel and C. K. Ober, Microelectronic Engineering **65**, 145 (2002).

[74] S. Maruo, T. Hasegawa, and N. Yoshimura, Optics express **17**, 20945 (2009).

[75] T. E. Oliphant, Computing in Science and Engineering **9**, 10 (2007).

[76] A. Ovsianikov *et al.*, ACSNano **2**, 2257 (2008).

[77] A. Pikulin and N. Bityurin, Physical Review B **82**, 085406 (2010).

[78] L. Landau and E. M. Lifschitz, *Theory of elasticity* (Pergamon, Oxford, 1970).

[79] M. Poot and H. S. van der Zant, Physics Reports **511**, 273 (2012).

[80] M. Qin and V. M. C. Poon, Journal of Materials Science Letters **19**, 2243 (2000).

[81] V. Mulloni, S. Colpo, a. Faes, and B. Margesin, Journal of Micromechanics and Microengineering **23**, 025025 (2013).

[82] M. S. Williams and J. D. Todd, *Structures: theory and analysis* (MacMillian, London, 2000).

[83] J. M. Gere, *Mechanics of materials*, 5th ed. (Brooks/Cole, Pacfic Grove, CA., 2001).

[84] T. B. Jones and N. G. Nenadic, *Electromechanics and MEMS* (Cambridge University Press, Cambridge, 2013).

[85] S. Timoshenko and J. N. Goodier, *Theory of elasticity*, Second ed. (McGraw-Hill, London, 1951).

[86] S. S. Singh, P. Pal, and A. K. Pandey, Journal of Applied Physics **118**, 204303 (2015).

[87] S. Abrate, Journal of Sound and Vibration **185**, 703 (1995).

[88] K. V. Singh, G. Li, and S.-S. Pang, Composite Structures **74**, 37 (2006).

[89] E. M. Arruda and M. C. Boyce, International Journal of Plasticity **9**, 697 (1993).

[90] C. A. Harper, *Modern Plastics Handbook* (McGraw-Hill, New York, 2000).

[91] J. Haberko, N. Muller, and F. Scheffold, Physical Review A **88**, 043822 (2013).

[92] J. Haberko and F. Scheffold, Optics express **21**, 1057 (2013).

[93] I. Staude *et al.*, Optics letters **35**, 1094 (2010).

[94] I. Staude, G. von Freymann, S. Essig, K. Busch, and M. Wegener, Optics letters **36**, 67 (2011).

[95] I. Staude *et al.*, Advanced Materials **25**, 1260 (2013).

[96] N. Tétreault *et al.*, Advanced Materials **18**, 457 (2006).

[97] M. Rill *et al.*, Conference on Quantum Electronics and Laser Science (QELS) - Technical Digest Series , 543 (2008).

[98] J. Li *et al.*, Laser and Photonics Reviews **8**, 602 (2014).

[99] T. Asavei, T. a. Nieminen, N. R. Heckenberg, and H. Rubinsztein-Dunlop, Journal of Optics A: Pure and Applied Optics **11**, 034001 (2009).

[100] H. O. Moser and C. Rockstuhl, Laser and Photonics Reviews **6**, 219 (2012).

[101] J. Mu *et al.*, Applied Physics B , 121 (2014).

[102] A. Žukauskas, M. Malinauskas, C. Reinhardt, B. N. Chichkov, and R. Gadonas, Applied Optics **51**, 4995 (2012).

[103] D. B. Phillips, M. J. Padgett, J. G. Rarity, M. J. Miles, and S. H. Simpson, **9374**, 937402 (2015).

[104] S. Tottori *et al.*, Advanced Materials **24**, 811 (2012).

[105] M. Skeren, J. Svoboda, M. Kveton, and P. Fiala, Journal of Physics: Conference Series **415**, 012075 (2013).

[106] V. V. Parsi Sreenivas, M. Bülters, M. Schröder, and R. B. Bergmann, **9130**, 91300M (2014).

[107] A. Bondeson, T. Rylander, and P. Ingelstrom, *Computational Electromagnetics* (Springer, Berlin, 2005).

[108] B. M. A. Rahman and A. Agrawal, *Finite Element Modeling Methods for Photonics* (Artech House, Norwood, MA., 2013).

[109] A. Yariv and P. Yeh, *Optical waves in crystals* (Wiley, New York, 1984).

[110] A. Ghatak and K. Thyagarajan, *Introduction to fiber optics* (Cambridge University Press, Cambridge, 1998).

[111] M. Flatt, Communications of the ACM **55**, 48 (2012).

[112] M. F. Pantano, H. D. Espinosa, and L. Pagnotta, Journal of Mechanical Science and Technology **26**, 545 (2012).

[113] V. T. Srikar and S. M. Spearing, Experimental Mechanics **43**, 238 (2003).

[114] H. J. Butt, B. Cappella, and M. Kappl, Surface Science Reports **59**, 1 (2005).

[115] J. E. Sader *et al.*, Review of Scientific Instruments **83** (2012).

[116] S. J. Eppell, B. N. Smith, H. Kahn, and R. Ballarini, Journal of the Royal Society Interface **3**, 117 (2006).

[117] J. Vlassak and W. Nix, Journal of Materials Research **7**, 3242 (1992).

[118] A. C. Fischer-Cripps, *Nanoindentation*, 3rd ed. (Springer, 2011).

[119] A. Ergin, B. Michielssen, and E. Shanker, IEEE Antennas and Propagation Magazine **41**, 39 (1999).

[120] D. Jiao, A. A. Ergin, B. Shanker, E. Michielssen, and J.-M. Jin, IEEE transactions on antennas and propagation **50**, 1192 (2002).

[121] H. Bagci, A. Ylmaz, J.-M. Jin, and E. Michielssen, Time Domain Adaptive Integral Method for Surface Integral Equations, in *Lecture Notes in Computational Science and Engineering*, chap. 3, pp. 65–104, Springer, Berlin, 2008.

[122] R. Learn and E. Feigenbaum, Applied Optics **55**, 4402 (2016).

[123] D. Liu, *Advances in Beam Propagation Method for Facet Reflectivity Analysis*, PhD thesis, University of Nottingham, 2013.

[124] M. Fogus and C. Houser, *The Joy of Clojure*, Second edi ed. (Manning Publications, New York, 2014).

[125] H. Fujiwara, *Spectroscopic Ellipsometry: Principles and Applications* (John Wiley & Sons, Chichester, 2007).